Aspects of Integrated Amplification for Silicon Photonics

Aspects of Integrated Amplification for Silicon Photonics

By Yuxuan Gao, M.A.Sc.

A Thesis Submitted to the School of Graduate Studies in the Partial Fulfillment of the Requirements for the Degree Ph.D.

McMaster University © Copyright by Yuxuan Gao May 6, 2024

McMaster University

Ph.D. (2024)

Hamilton, Ontario (Department of Engineering Physics)

TITLE: Aspects of Integrated Amplification for Silicon Photonics

AUTHOR: Yuxuan Gao (McMaster University)

SUPERVISORS: Dr. Andrew P. Knights, Dr. Peter Mascher

NUMBER OF PAGES: xvii, 147

Abstract

The exponential rise in global data traffic and the growing reliance on digital applications is pushing the bandwidth demands within data centers. The traditional hierarchical network architecture of data centers, primarily relying on electrical interconnects, faces scalability challenges including power dissipation, bandwidth limitations, and cooling requirements. Optical interconnects, using fibers and pluggable transceivers, emerge as a promising solution to these challenges, offering advantages such as electromagnetic interference resistance, high bandwidth, and efficient energy usage.

This thesis explores the design, fabrication, and characterization of opto-electronic devices to be used as components for optical transceivers on a silicon photonics platform, which leverages the mature complementary metal-oxide semiconductor fabrication technology. Chapter 2 introduces the basics of waveguide theory alongside the principles behind defect-based avalanche photodiodes, phototransistors, and two-level system optical amplifiers. Chapter 3 details the design, simulation, and characterization of a high-responsivity silicon/germanium phototransistor, achieving over 1000 A/W in performance. Chapter 4 discusses the design and measurement of an all-silicon avalanche photodetector for near-infrared wavelengths mediated by deep-level defects. In Chapter 5, the focus shifts to enhancing the previously mentioned photodetector's responsivity through slow light gain with subwavelength grating waveguide structures, with details on its design, simulation, fabrication, and characterization. Chapter 6 explores the development and analysis of an erbium-doped waveguide amplifier on a hybrid silicon nitride - tellurite platform, incorporating erbium ions via ion implantation.

This thesis makes contributions toward realizing efficient silicon photonics-based data communication infrastructure, supporting the escalating demand for bandwidth while mitigating power consumption and improving system scalability.

Acknowledgements

I express my deepest gratitude to all who have contributed to the completion of this thesis. Foremost, I extend my sincere appreciation to my supervisors, Dr. Andy Knights and Dr. Peter Mascher, for their boundless guidance, patience, and support throughout my PhD journey. Their expertise and insightful feedback have been instrumental in shaping this work. My committee members, Dr. Jonathan Bradley and Dr. Adrian Kitai, deserve special thanks for their encouragement, constructive critiques, and valuable time. Their insights have been crucial in refining my research.

I am thankful to my lab mates from Dr. Knights' lab—Yanran Xie, Ranjan Das, Feng Guo, Arthur Mendez-Rosales, Dylan Genuth-Okon, Keru Chen, Gregory Thomas, and Mohammad Islam—and those from Dr. Mascher's lab—Fahmida Azmi, Tiancheng Wu, and Paramita Bhattacharyya—for their camaraderie, stimulating discussions, and shared insights that have significantly contributed to my motivation and intellectual growth.

I also extend my sincere thanks to our neighboring group members, Batoul Hashemi, Bruno L.S. Frare, Cameron Naraine, Pooya T. Ahmadi, and Niloofar M. Taleghani, for their approachability and fruitful collaborations. My gratitude goes to Doris Stevanovic from the Center for Emerging Device Technology (CEDT) for her support and assistance.

Special appreciation is directed to my parents, whose unconditional love, understanding, and encouragement have been my cornerstone throughout this journey.

Lastly, I must acknowledge my partner, Ying Hu, who became my wife during my PhD journey. The completion of this thesis would not have been possible without her unwavering love and support.

Contents

Abstract iii

Acknowledgements iv

Contents v

List of Figures ix

List of Tables xiii

Declaration of Authorship xvii

1 Introduction **1**

1.1 Optical interconnects for data centers 1

1.2 Silicon photonics 3

1.2.1 Overview of silicon photonics 3

1.2.2 Challenges in silicon photonics 5

1.3 Thesis objectives 8

1.4 Statement of thesis work 9

1.5 Publications 10

1.6 References 12

2 Background **20**

2.1 Silicon photonics platform 20

2.2 Waveguide theory . . . 21
2.2.1 Electromagnetic wave propagation . . . 21
2.2.2 Electromagnetic waves in a 2-D slab waveguide . . . 24
2.2.3 Light propagating in SOI waveguide . . . 28
2.2.4 Group index and slow light . . . 30
2.2.5 Subwavelength grating waveguide . . . 34
2.2.6 Waveguide material systems . . . 37
2.2.7 Effective index method for mode solving . . . 38
2.3 Photodetection . . . 39
2.3.1 Optical absorption in SOI waveguides . . . 40
2.3.2 Photodiodes . . . 46
2.3.3 Avalanche photodetector . . . 51
2.3.4 Phototransistor . . . 52
2.4 Erbium doped waveguide amplifiers . . . 54
2.4.1 Erbium luminescence . . . 54
2.4.2 Amplification in erbium-based systems . . . 57
2.4.3 Erbium implantation in tellurium oxide . . . 58
2.5 References . . . 60

3 Si/Ge Phototransistor with Responsivity over 1000A/W on a Silicon Photonics Platform 68

3.1 Abstract . . . 69
3.2 Introduction . . . 69
3.3 Method . . . 71
3.3.1 Operational principle . . . 71
3.3.2 Device fabrication . . . 74
3.3.3 Device characterization . . . 74
3.4 Experimental results . . . 75

3.4.1 Steady-state response . . . 75
3.4.2 Assessing the impact of the floating p-doped regions . . . 78
3.4.3 Electrical bandwidth and phase noise . . . 80
3.5 Discussion and Conclusion . . . 82

4 Monolithic silicon avalanche photodetector utilizing surface state defects operating at 1550 nm 90

4.1 Abstract . . . 91
4.2 Introduction . . . 91
4.3 Fabrication and Characterization . . . 93
4.3.1 Device Fabrication . . . 93
4.3.2 Device Characterization . . . 95
4.4 Results and discussions . . . 96
4.5 Summary . . . 99

5 Slow Light Enhanced Monolithic Silicon Photodetector Using Subwavelength Grating Waveguides 104

5.1 Abstract . . . 105
5.2 Introduction . . . 105
5.3 Method . . . 107
5.3.1 Device design . . . 107
5.3.2 Device fabrication . . . 109
5.3.3 Device characterization . . . 110
5.4 Experimental Results and Discussion . . . 110
5.4.1 Intrinsic photodetector characterization . . . 110
5.4.2 Enhanced responsivity with mid-bandgap defects . . . 114
5.5 Conclusion . . . 116

6 Erbium implanted waveguide amplifier on SiN platform 123

6.1 Abstract 124

6.2 Introduction 124

6.3 Methods 127

6.4 Measurement results 128

6.5 Conclusion 133

7 Conclusions and future perspectives **140**

7.1 Summary of work 140

7.2 Suggested future work 143

7.3 References 146

List of Figures

1.1 Typical building blocks of a complete PIC platform: generation, routing, processing, detection, and modulation [37]. 5

2.1 Cross-section view of the silicon-on-insulator (SOI) wafer. 21

2.2 Total internal reflection for a guided mode in a slab waveguide. 25

2.3 TE modes in an asymmetric step-index planar waveguide [23]. 27

2.4 Two types of frequently used waveguides on SOI platform. 28

2.5 Simulated (a) mode profile, and (b) and effective index and group index of a waveguide with 220 nm height and 500 nm width at 1550 nm. 29

2.6 Simulated bending loss as a function of bending radius (μm) for the strip waveguide shown in Fig. 2.4. 30

2.7 Wave packet composed of two frequency components. 31

2.8 a), Silicon-on-insulator slab waveguide with etched SWG, for light propagation along the z axis. Schematic dispersion diagram (b) and simulated electric field profiles (c) of radiation regime (top), slow light regime (middle), and deep SWG regime (bottom). 36

2.9 Optical absorption versus wavelength for various semiconductor materials [31] © 1985 John Wiley & Sons. 40

2.10 Band diagram of the two-photon absorption mechanism in Si. 42

2.11 Cross-sectional view of BDA detectors (left) , and energy level diagram of BDA detectors (right) [32]. 43

2.12 Cross-sectional view of SSA detectors 46
2.13 A conceptual diagram of the avalanche multiplication process. 51
2.14 a) Schematic structure of a conventional SOI phototransistor integrated with a ridge waveguide. b) Energy band diagram under bias. 52
2.15 Energy level diagram of Er^{3+} ions[55]. 55
2.16 Optical processes: optical absorption, spontaneous emission, and stimulated emission. 56
2.17 a) Schematic cross-sectional view of the cross section view of the Si_3N_4 waveguide cladded with TeO_2 glass with a thickness of 100 nm, b) optical mode profile of the propagating light at 1550 nm, and c) simulated ion implantation ion as a function of implantation depth based on an energy of 200 KeV. 59

3.1 Cross-sectional diagram of the n-p-n structure of the Si/Ge photodetector with electric field and current density (J) simulation of the photodetector at a forward bias of 2 V_{ce}. Voltage is applied on the emitter and the right side collector only in the simulation. Bottom shows the band diagrams of the devices with a cutline at the Si/Ge interface demonstrated in the current density plots. Left, without p^+-doping; right, with p^+-doping. . . 72
3.2 a, b) Device dark current, illuminated current, and responsivity under different incident power levels with incident light at 1550 nm; c) responsivity versus optical power at different applied voltage; d) I_{ON}/I_{OFF} ratio of the device under different incident power levels. 76
3.3 a) Dark current, b) illuminated current (-10 dBm optial power), for devices with different geometries (without p^+-doped regions, with 1 µm and 0.75 µm width p^+-doped region); device dark current and responsivity comparisons with c) varying p^+-doped regions distances, and d) varying p^+-doped region widths. 78

3.4 a) 3-dB bandwidth for devices with 1 µm and 0.75 µm p^+-region widths under 1 V_{CE}; b) Phase noise with 1 GHz RF carrier for device with 0.75 µm p^+-region under different biases of V_{CE}(1 V, 4 V, and -4 V). 81

4.1 Schematic show of surface state defects (left) and bulk defects (right). . . 93
4.2 Cross-sectional diagram of the p-i-n diode. 94
4.3 Measured illuminated currents and dark currents of reference device, SSD device, and BDA device. 96
4.4 Photocurrent of devices before and after surface state defects activation, after native-grown oxide and controlled surface oxidation. 97
4.5 SEM image of device a) as received and b) HF etched. 98
4.6 Bandwidth measurement of SSD devices under various biases (10 V, 15 V, and 32 V). 99

5.1 a) Device structure, b) SWG waveguide diagram of the device, c) simulated effective index, d) band diagram, and e) group index of the devices with a duty cycle of 0.5 and varied periods from 250 nm to 400 nm. . . . 107
5.2 Simulated Floquet-Bloch mode propagating in the SWG waveguide at slow light regime (1550 nm) with cross-section view(i), top view at the ridge region (ii) and slab region (iii), and SWG regime (1600 nm) with cross-section view(iv), top view at the ridge region (v) and slab region (vi).109
5.3 a) Fiber-to-fiber transmission of the reference straight waveguide (STWG) and the slow light (SWG) device test structure for $\Lambda = 300nm$ and duty cycle of 0.5 and 0.47; b) Illuminated current from the corresponding photodetectors of these waveguide structures. Dark current (not shown) is below 0.3 nA at a bias of 33V (avalanche) for all the devices. 111
5.4 114
5.5 116

6.1 a) Diagram of the TeO_2:Er^{3+}-coated Si_3N_4 waveguide structure. b) Calculated (black dot) and fitted (red line) erbium concentration using TRIM simulations, and the simulated optical transverse electric (TE) mode intensity (inset). . . . 126

6.2 Experimental setup for measuring gain in TeO_2: Er^{3+} cladded Si_3N_4 spiral waveguides. . . . 129

6.3 a) The Lorentzian fittings indicating the Q-factors of the microrings before implantation, right after implantation, and after annealing. . . . 129

6.4 Measured and fitted photoluminescence intensity decay a) before and b) after annealing. . . . 130

6.5 a) Measured Er implantation loss spectrum (excluding fiber-chip edge coupling loss) of waveguide after implantation (blue) and annealing (green); b) Measured signal enhancement factor (dB) at 1550 nm as a function of on-chip optical pump power (mW) at 1470 nm. . . . 131

List of Tables

3.1 A performance summary of selected phototransistors on silicon photonics platform. 84

4.1 Device summary with post process details 95

List of Acronyms

AMF Advanced Micro Foundry

APDs avalanche photodetectors

BDA bulk defect absorption

BJT bipolar junction transistor

CAD computer-aided design

CMOS complementary metal-oxide-semiconductor

CPO co-packaged optics

ECR-PECVD electron cyclotron resonance plasma enhanced chemical vapour deposition

EDFA erbium-doped fiber amplifier

EDWA erbium-doped waveguide amplifier

EDWAs erbium-doped waveguide amplifiers

EIM effective index method

ESA electrical spectrum analyzer

FIB focused ion beam

Ge germanium

IC integrated circuit

IoT internet of things

LA limiting amplifier

LDs laser diodes

LIDAR light detection and ranging

MFD mode field diameter

MPW multi-project wafer

MZI Mach–Zehnder interferometer

NIR near-infrared

PDK process design kits

PICs photonic integrated circuits

PN phase noise

QE quantum efficiency

RF radio-frequency

RI refractive index

SOI silicon-on-insulator

SSA surface state absorption

SSB single side band

SSD surface state defects

SWG subwavelength grating

TCAD technology computer aided design

TDFA thulium doped fiber amplifier

TE transverse electrical

TIA transimpedence amplifier

TPA two-photon absorption

TRIM transport of ions in matter

UTC uni-traveling-carrier

WDM wavelength-division multiplexing

Declaration of Authorship

I, Yuxuan GAO, declare that this thesis titled, “Aspects of Integrated Amplification for Silicon Photonics” was written by and presents research work lead by myself. Contributions made by others to this work are as listed:

Chapter 3

- Feng Guo aided with measuring IV curves of the phototransistors
- Ranjan Das aided with the bandwidth and phase noise measurements

Chapter 4

- David Hagan performed the tape-outs of the device
- Doris Stevanovic performed the ion implantation

Chapter 5

- Yanran Xie contributed to the design of the experiment
- Jack Hendriks assisted with ion implantation

Chapter 6

- Batoul Hashemi contributed to the scientific discussion, device measurement and data analysis
- Bruno Segat Frare performed TeO_2 deposition and assisted with sample preparation
- Ion Beam Center at University of Surrey performed the ion implantation

Chapter 1

Introduction

1.1 Optical interconnects for data centers

The COVID-19 pandemic has fundamentally transformed the landscape of global data traffic, marked by a significant shift in how data is used. A surge in internet traffic was fueled by a greater dependence on emerging applications such as cloud storage and computing, high-definition video streaming and conferencing, the internet of things (IoT), and various multimedia applications. These bandwidth hungry services are often hosted in data centers, requiring extensive server-to-server interactions [1]. The global bandwidth demand is expected to double every 18 months and the internal network bandwidth within hyperscale data centers is over 70% of the total worldwide bandwidth, estimated by Cisco [2]. A hierarchical architecture is the most typical design of data center networks, where information is passed between layers and layers on the request of users [3]. The application servers will need to communicate with other servers, to process the request and then send the response to the Internet through gateway routers. Most of the global data traffic has been in the data centers and is expected to stay in the data centers [4].

Data centers, which have been extensively utilizing intra/interchip electrical interconnects for server communication and user-cloud interactions, are facing significant challenges as they scale up. This scaling brings about numerous issues with the increased use of electrical interconnects, such as power dissipation, interconnect delays, transmission loss, limited bandwidth, clock synchronization problems, and electrical noise [5, 6]. Additionally, excess heating caused by power dissipation from these electrical interconnects necessitates cooling systems that consume almost 40% of the total power in a data center [7]. Furthermore, the bandwidth for radio-frequency (RF) signals diminishes over long transmission distances in electrical wires [8], leading to reduced economic efficiency as more servers are added. Confronting these challenges, data centers must innovate to develop more effective networking solutions.

In high-speed data centers optical fibers and transceivers are predominantly used for interconnects [9]. An optical transceiver, comprising an optical transmitter and receiver, is equipped with both electrical and optical interfaces. These interfaces are designed to adhere to industry standards, ensuring interoperability with components from various vendors.

Optical transmission is resistant to electromagnetic interference, and more importantly, optical transmission is not affected by modulation rate, enabling high-bandwidth and low-loss data exchange in the short range. Furthermore, the invention of wavelength-division multiplexing (WDM) systems in the 1990's enables multiple wavelengths to be modulated and transmitted separately and simultaneously through the same single fiber, significantly increasing the transmission bandwidth through parallelism. Additionally, no excess heating is created during the optical signal propagation in dielectric waveguides, which could save a large portion of the total power consumption for cooling in the conventional electrical driven data centers.

However, the complexity of traditional photonic integrated circuits (PICs) manufacturing arises from the need to use different material systems for various functional photonic components. For instance, laser diodes (LDs) predominantly utilize InP [10] or GaAs [11], while the most effective modulators are made with $LiNbO_3$ [12, 13]. Waveguides are typically constructed using SiO_2/Si or SiO_2/Si_3N_4, and photodetectors often prefer SiGe [14], among others. A key challenge in PIC development is integrating these diverse materials and functional components onto a single substrate and ensuring their collaborative operation. Silicon photonics has shown great potential as a large-scale optoelectronic integration platform.

1.2 Silicon photonics

1.2.1 Overview of silicon photonics

Since Texas Instruments' invention of the first integrated circuit (IC) [15], silicon has become the most important material in the information technology industry, primarily due to the mature complementary metal-oxide-semiconductor (CMOS) electronics fabrication technology. Silicon photonics aims to extend the application of CMOS technology to photonics and opto-electronics, offering a significant economic advantage over other photonic materials like III-V compounds and polymers [16–18]. After billions of dollars and decades of research, silicon photonics has sucessfully bridged the gap between research and commercialization, and is now widely accepted as a key technology in the next generation optical communication systems [19–23].

In addition to manufacturing cost, silicon photonics also provides several technical advantages over other platforms for the development of high performance optical transceivers. Due to the large refractive index (RI) contrast between silicon (around 3.5) and silicon dioxide (around 1.45), the optical mode at 1550 nm can be confined in small waveguides (typically 450 nm x 220 nm cross-section) with bend radius as low

as 10 µm, enabling ultra compact PICs on a single semiconductor unit using silicon-on-insulator (SOI) technology. With an optical band-gap of around 1100 nm, silicon is suitable for the conventional telecommunication wavelength region (1300 - 1600 nm) [24, 25]. High-quality crystalline silicon yields low-loss silicon waveguides (lower than 2 dB/cm), which can be obtained inexpensively. High-resolution lithography provided by the silicon photonics foundries enables the realization of sophisticated passive photonic devices including subwavelength grating waveguides [26], high-quality resonance cavities [27, 28], and complicated devices by inverse design [29, 30].

The field of silicon photonics was initiated in 1985 with a pioneering proposal to integrate photonic components using silicon, due to silicon's transparency in the near-infrared spectrum [31]. The breakthrough came in 1991 with the successful demonstration of a Silicon on Insulator (SOI) waveguide, notable for its low loss characteristics [32]. This development sparked a surge in research interest, leading to the development of various key components such as integrated directional couplers [33], multiplexers/de-multiplexers [34], and active components like micro-ring resonators [35]. A landmark achievement was the demonstration of a 1 GHz silicon modulator by Intel in 2004 [36], a development that underscored the potential of silicon photonics in application in next-generation optical communication technologies. Nowadays, despite still being in its nascent commercialization stage, silicon photonics has a relatively well-developed ecosystem including not only traditional silicon industries [37], but also start-up companies focusing on datacom and artificial intelligence, supporting software including computer-aided design (CAD) and optical/electrical simulation, and foundry services which provides multi-project wafer (MPW) tape-outs and the associating process design kits (PDK) [38].

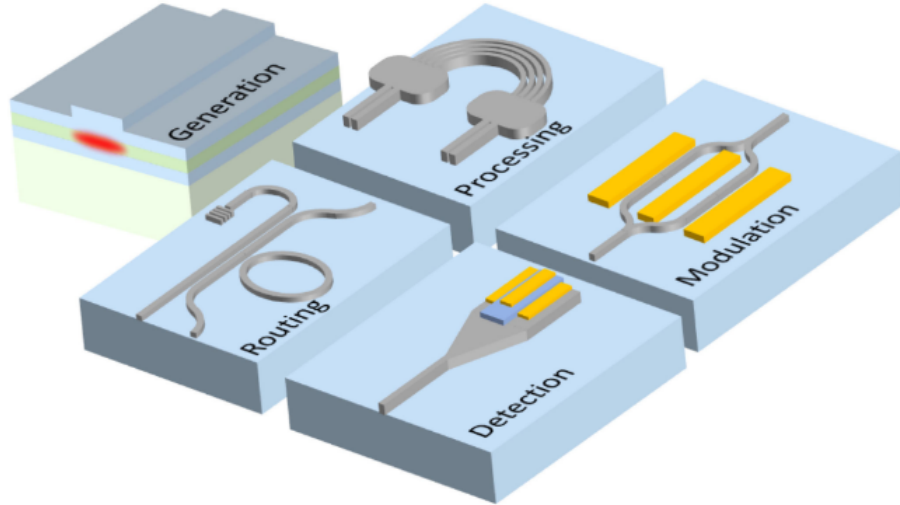

Figure 1.1: Typical building blocks of a complete PIC platform: generation, routing, processing, detection, and modulation [37].

1.2.2 Challenges in silicon photonics

Silicon photonic circuits are designed mainly to manipulate light in silicon, which contains light generation, modulation, routing, processing, and detection [37], as shown in Figure 1.1.

Despite the advantages of silicon, it has some poor properties for photonic development. The generation of light from silicon has always been challenging due to the indirect bandgap of silicon, which limits the efficiency of radiative recombination at room temperature [39]. To transition an electron from band to band of silicon, external momentum is needed in the form of phonons (lattice vibration), resulting in an emission quantum efficiency of bulk silicon lower than 1% [40]. The size of the indirect bandgap of silicon also causes poor optical absorption in the conventional telecommunication wavelength region, which is an obstacle for monolithic silicon photodetector development.

Optical detection and amplification will be discussed in detail in the following subsections.

Photodetection

A photodetector transforms optical signals into electrical signals, voltage or current, by generating electron-hole pairs when photons are absorbed. This process happens when the photon energy exceeds the semiconductor material's bandgap, leading to the creation of these carriers. Applying external reverse bias creates an expanded depletion region, forming a high electric field that aids in the collection of the photogenerated carriers, allowing them to travel at saturation velocity. However, silicon's transparency in the infrared wavelength makes it a less effective optical absorber at communication wavelengths.

For that reason, hetero-epitaxial germanium (Ge) is often chosen as the ideal material for the intrinsic region due to its strong absorption in the near-infrared spectrum and its compatibility with CMOS technology. This compatibility allows for efficient, high-throughput, and cost-effective integration. The integration of germanium photodiodes in CMOS has been particularly successful, demonstrating large responsivities [41]. These photodetectors maintain their effectiveness up to about 1600 nm, covering most of the erbium-doped fiber amplifier (EDFA) wavelength band [42].

However, Ge-based photodetectors also face challenges. The hetero-epitaxial integration of Ge on Si presents material difficulties due to a significant lattice mismatch of 4.2% between Si and Ge [22, 43]. This mismatch leads to high dark current in germanium photodiodes, making them less suitable for sensitive applications. The increased noise due to the high dark current necessitates more optical power in the optical link to distinguish between signal and noise, resulting in higher overall power consumption. As photonic circuits evolve, reducing power consumption becomes increasingly important.

With the rapid increase in data transmission via optical networks, there is a growing need for advanced photonic technologies to avoid a potential 'capacity crunch' [44]. A promising approach is the exploration of new spectral regions at longer wavelengths. Due

to the limited absorption range (up to 1600 nm), current Ge-based photodetectors will not be capable of detection for example, in the thulium doped fiber amplifier (TDFA) band centered at 1900 nm.

Achieving a monolithic silicon integration for components made entirely from silicon would simplify fabrication and reduce fabrication costs. Silicon-on-Insulator technology can achieve photo-detection through a monolithic approach known as defect-mediated photo-detection. This process involves intentionally introducing defects in silicon to create intermediate energy levels [45–47], enabling the excitation of electrons in the valence band through photo-absorption. Silicon-based detectors, characterized by low dark current [48, 49], can become more responsive under high reverse bias due to avalanche photo-detection from impact-ionization of photo-generated carriers. The monolithic photodetectors utilizing various mechanism will be discussed in the forthcoming chapters.

Optical amplification

Optical amplification is needed to compensate for the attenuation of the light signal in the communication networks due to limited link budget of optical power and photodetector sensitivity. Erbium ions have demonstrated stimulated emission of photons covering the telecommunication C-band (1525 - 1564 nm) with low noise. In the late 1980s, the invention of the EDFA extended the optical network by regenerating the optical signal every few tens of kilometers [50] with high data integrity and enhanced network scalability.

Intensive research efforts have been applied to miniaturize the EDFA into on-chip amplifiers for optical interconnects, which are known as erbium-doped waveguide amplifiers (EDWAs). EDWAs offer advantages including robust performance, low-cost, and high integration due to their compact sizes. However, it still remains a challenge to

efficiently incorporate Er ions, especially when EDWAs have much shorter amplification lengths compared to conventional EDFAs.

In EDFAs, Er ions are directly doped to the fiber core. However, being crystalline material, a silicon waveguide will be damaged if external ions are directly introduced to the silicon matrix, unless annealed with very high temperature [51]. Another approach is to dope the Er into waveguide cladding materials, which provides flexibility for the selection of waveguide material. When pumped with light at 980 nm or 1480 nm, the evanescent field of the light propagating in the waveguide cladding region will interact with the local dopants.

Research efforts have explored various material systems and fabrication methods to enhance Er solubility, reduce propagation loss, ensure uniform growth on large substrates, ensure CMOS compatibility, and maintain high deposition rates [52]. Host materials under investigation include crystalline ones like lithium niobate [53–55] and amorphous ones such as aluminum oxides (Al_2O_3) [56–60], tantalum pentoxide (Ta_2O_5) [61, 62], and tellurium oxide (TeO_2) [63–65], all aiming to achieve optical gain through erbium doping.

In addition to material optimization, integrating optical amplifiers into the silicon photonics platform involves challenges like efficient light coupling, loss minimization, and thermal management. Fabrication and characterization of an EDWA on a hybrid Si_3N_4-TeO_2 platform will be discussed in Chapter 6.

1.3 Thesis objectives

The objectives of this thesis work are to investigate the design, fabrication, and characterization methodologies of integrated photodetectors and EDWAs on a the silicon photonics platform. Various gain mechanisms including transistor amplification, avalanche

multiplication, and slow light gain are used to investigate enhanced photodetector responsivity. Whereas, development of EDWAs utilizes design of fabrication process using sputtering deposition and ion implantation. This work aims to make a significant step toward the realization of silicon photonics technology compatible transceivers for use in future data communication infrastructure to accommodate system level link budget due to the scaling up of data centers.

1.4 Statement of thesis work

This thesis consists of seven chapters and discusses integrated amplification for silicon photonics for light detection and amplification.

Chapter 2 provides a brief review of waveguide theory and the working principle of defect-based avalanche photodiodes, phototransistors, and the two-level system optical amplifier. Chapter 3 presents a published manuscript on the design, simulation, and characterization of a Si/Ge based phototransistor with high responsivity over 1000 A/W. Chapter 4 presents a published manuscript on the design, fabrication and characterization of an all-silicon avalanche photodetector operating in the near infrared wavelength utilizing deep-level defects. Chapter 5 presents a manuscript in preparation for submission on the design, simulation, fabrication, and characterization of the device designed in Chapter 4 with increased responsivity achieved through slow light gain for optical communication application. Chapter 6 presents a manuscript in preparation for submission on the design and characterization of an EDWA on hybrid Si_3N_4-TeO_2 platform with erbium ions introduced using ion implantation. Chapter 7 summarizes the thesis and discusses potential future research directions related to this work.

1.5 Publications

The following is a list of journal articles by the author that have contributed to the results presented in this thesis:

- **Y. Gao**, R. Das, Y. Xie, P. Mascher, and A. P. Knights, "Slow Light Enhanced Monolithic Silicon Photodetector Using Subwavelength Grating Waveguides," Manuscript in preparation.
- **Y. Gao**, B. Hashemi, B. L. S. Frare, H. C. Frankis, J. D.B. Bradley, P. Mascher, and A. P. Knights, "Signal enhancement from hybrid erbium-implanted tellurite waveguide integrated on silicon nitride platform," Manuscript in preparation.
- **Y. Gao**, F. Guo, Y. Xie, P. Mascher, and A. P. Knights, "Defects-Mediated Monolithic Integrated Silicon Avalanche Photodetector Operating at 1550 nm," Manuscript in preparation.
- **Y. Gao**, R. Das, Y. Xie, F. Guo, P. Mascher, and A. P. Knights, "Si/Ge Phototransistor with Responsivity >1000 A/W on a Silicon Photonics Platform," Optics Express, vol. 32, no. 2, pp. 2271-2280, 2024.

The author has also contributed to the following conference posters, presentations, and proceedings:

- **Y. Gao**, F. Guo, R. Das, P. Mascher, and A. P. Knights, "High responsivity Si/Ge phototransistor on silicon photonics platform for small signal application," in Proc. 2023 Photonics North (PN), 2023, pp. 1-1.
- **Y. Gao**, F. Guo, P. Mascher, and A. P. Knights, "Monolithic silicon avalanche photodetector utilizing surface state defects operating at 1550 nm," in Silicon Photonics XVIII, vol. 12426, pp. 61-65, 2023, SPIE.

- A. P. Knights, **Y. Gao**, F. Guo, and P. Mascher, "Silicon photodetector operating at 1550nm utilizing surface state defects - applications in avalanche detection and energy harvesting," presented in Photonics North (PN), Montreal, Canada, 2023

- **Y. Gao**, B. Hashemi, B. L. S. Frare, F. Guo, J. D. B. Bradley, P. Mascher, and A. P. Knights, "Erbium-Doped Waveguide Amplifier (EDWA) for Silicon Photonic Integrated Circuits," presented at Nano Ontario 2022, Waterloo, Canada, 2022 (Poster)

- **Y. Gao**, F. Guo, P. Mascher, and A. P. Knights, "Performance Enhancement of a Monolithic Silicon APD Operating at 1550 nm using Post Fabrication Processing," presented in Photonics North (PN), Niagara Falls, Canada, 2022

Additionally, the author has contributed to the following journal publications, which are not directly presented or discussed over the course of this thesis:

- S. Sakib, R. MacLachlan, **Y. Gao**, P. Mascher, A. Knights, L. Soleymani, and I. Zhitomirsky, "Catecholate Dye-Assisted Decoration of Ag on TiO_2 Nanoparticles for Detection of Cancer-Related MicroRNA Biomarkers on a Multiplexed Photoelectrochemical Platform," ACS Applied Nano Materials, vol. 6, no. 21, pp. 20375-20388, 2023, ACS Publications.

- F. Azmi, **Y. Gao**, Z. Khatami, and P. Mascher, "Tunable emission from Eu: SiO_xN_y thin films prepared by integrated magnetron sputtering and plasma enhanced chemical vapor deposition," Journal of Vacuum Science & Technology A, vol. 40, no. 4, 2022, AIP Publishing.

- **Y. Gao**, Z. Khatami, and P. Mascher, "Influence of Nitrogen on the Luminescence Properties of Ce-Doped SiO_xN_y," ECS Journal of Solid State Science and Technology, vol. 10, no. 7, p. 076005, 2021, IOP Publishing.

1.6 References

[1] S. Sakr, A. Liu, D. M. Batista, and M. Alomari, A survey of large scale data management approaches in cloud environments, *IEEE communications surveys & tutorials*, vol. 13(3), 311–336, 2011.

[2] Cisco, *Global cloud index*, `https://www.cisco.com/c/en/us/solutions/collateral/service-provider/global-cloud-index-gci/white-paper-c11-738085.html`, 2018.

[3] M. Imran and S. Haleem, Optical interconnects for cloud computing data centers: Recent advances and future challenges, *Proceedings of Science*, vol. 327, 2018, ISSN: 18248039.

[4] T. Benson, A. Anand, A. Akella, and M. Zhang, Understanding data center traffic characteristics, *ACM SIGCOMM Computer Communication Review*, vol. 40(1), 92–99, 2010.

[5] H. Cho, P. Kapur, and K. C. Saraswat, Power comparison between high-speed electrical and optical interconnects for inter-chip communication, *Proceedings of the IEEE 2004 International Interconnect Technology Conference*, vol. 22(9), 116–118, 2004.

[6] G. Schulz, *The green and virtual data center*. CRC Press, 2016.

[7] C. Nadjahi, H. Louahlia, and S. Lemasson, A review of thermal management and innovative cooling strategies for data center, *Sustainable Computing: Informatics and Systems*, vol. 19, 14–28, 2018.

[8] R. Havemann and J. Hutchby, High-performance interconnects: An integration overview, eng, *Proceedings of the IEEE*, vol. 89(5), 586–601, May 2001, ISSN: 00189219.

[9] S. Aleksic, The future of optical interconnects for data centers: A review of technology trends, in *2017 14th International Conference on Telecommunications (ConTEL)*, IEEE, 2017, 41–46.

[10] Z. Lu, J. Liu, C. Song, J. Weber, Y. Mao, S. Chang, H. Ding, P. Poole, P. Barrios, D. Poitras, *et al.*, High performance inas/inp quantum dot 34.462-ghz c-band coherent comb laser module, *Optics Express*, vol. 26(2), 2160–2167, 2018.

[11] Z.-R. Lv, Z.-K. Zhang, X.-G. Yang, and T. Yang, Improved performance of 1.3-μm inas/gaas quantum dot lasers by direct si doping, *Applied Physics Letters*, vol. 113(1), 2018.

[12] L. Chen, Q. Xu, M. G. Wood, and R. M. Reano, Hybrid silicon and lithium niobate electro-optical ring modulator, *Optica*, vol. 1(2), 112–118, 2014.

[13] C. Wang, M. Zhang, X. Chen, M. Bertrand, A. Shams-Ansari, S. Chandrasekhar, P. Winzer, and M. Lončar, Integrated lithium niobate electro-optic modulators operating at cmos-compatible voltages, *Nature*, vol. 562(7725), 101–104, 2018.

[14] S. Liao, N.-N. Feng, D. Feng, P. Dong, R. Shafiiha, C.-C. Kung, H. Liang, W. Qian, Y. Liu, J. Fong, *et al.*, 36 ghz submicron silicon waveguide germanium photodetector, *Optics Express*, vol. 19(11), 10 967–10 972, 2011.

[15] J. S. Kilby, *Miniaturized electronic circuits*, US Patent 3,138,743, Jun. 1964.

[16] B. Jalali and S. Fathpour, Silicon photonics, *Journal of lightwave technology*, vol. 24(12), 4600–4615, 2006.

[17] A. Rickman, The commercialization of silicon photonics, *Nature Photonics*, vol. 8(8), 579–582, 2014.

[18] D. A. Miller, Optical interconnects to silicon, *IEEE Journal of Selected Topics in Quantum Electronics*, vol. 6(6), 1312–1317, 2000.

[19] G. T. Reed and A. P. Knights, *Silicon photonics: an introduction.* John Wiley & Sons, 2004.

[20] A. S. Mayer and B. C. Kirkpatrick, Silicon photonics, *Frontiers in Modern Optics*, vol. 24(12), 189–205, 2016, ISSN: 18798195.

[21] M. J. S. Shawon and F. Li, A review of the building blocks of silicon photonics: From fabrication perspective, *Semiconductor Science and Information Devices*, vol. 1(1), 29–35, 2019.

[22] D. Thomson, A. Zilkie, J. E. Bowers, T. Komljenovic, G. T. Reed, L. Vivien, D. Marris-Morini, E. Cassan, L. Virot, J.-M. Fédéli, *et al.*, Roadmap on silicon photonics, *Journal of Optics*, vol. 18(7), 073 003, 2016.

[23] S. Shekhar, W. Bogaerts, L. Chrostowski, J. E. Bowers, M. Hochberg, R. Soref, and B. J. Shastri, *Silicon photonics – roadmapping the next generation*, 2023.

[24] R. Soref, The past, present, and future of silicon photonics, *IEEE Journal of selected topics in quantum electronics*, vol. 12(6), 1678–1687, 2006.

[25] W. Bogaerts, R. Baets, P. Dumon, V. Wiaux, S. Beckx, D. Taillaert, B. Luyssaert, J. Van Campenhout, P. Bienstman, and D. Van Thourhout, Nanophotonic waveguides in silicon-on-insulator fabricated with cmos technology, *Journal of Lightwave Technology*, vol. 23(1), 401, 2005.

[26] P. Cheben, R. Halir, J. H. Schmid, H. A. Atwater, and D. R. Smith, Subwavelength integrated photonics, *Nature*, vol. 560(7720), 565–572, 2018, ISSN: 14764687.

[27] J. Niehusmann, A. Vörckel, P. H. Bolivar, T. Wahlbrink, W. Henschel, and H. Kurz, Ultrahigh-quality-factor silicon-on-insulator microring resonator, *Optics letters*, vol. 29(24), 2861–2863, 2004.

[28] A. Morand, Y. Zhang, B. Martin, K. P. Huy, D. Amans, P. Benech, J. Verbert, E. Hadji, and J.-M. Fédéli, Ultra-compact microdisk resonator filters on soi substrate, *Optics Express*, vol. 14(26), 12 814–12 821, 2006.

[29] A. Y. Piggott, J. Lu, K. G. Lagoudakis, J. Petykiewicz, T. M. Babinec, and J. Vučković, Inverse design and demonstration of a compact and broadband on-chip wavelength demultiplexer, *Nature Photonics*, vol. 9(6), 374–377, 2015.

[30] M. H. Tahersima, K. Kojima, T. Koike-Akino, D. Jha, B. Wang, C. Lin, and K. Parsons, Deep neural network inverse design of integrated photonic power splitters, *Scientific reports*, vol. 9(1), 1368, 2019.

[31] R. A. Soref and J. P. Lorenzo, Single-crystal silicon: A new material for 1-3 and 1-6 fim integrated-optical components, *Electronics Letters*, vol. 21(21), 953–954, 1985, ISSN: 00135194.

[32] J. Schmidtchen, A. Splett, B. Schuppert, K. Petermann, and G. Burbach, Low loss singlemode optical waveguides with large cross-section in silicon-on-insulator, *Electronics letters*, vol. 16(27), 1486–1488, 1991.

[33] P. Trinh, S. Yegnanarayanan, and B. Jalali, Integrated optical directional couplers in silicon-on-insulator, *Electronics Letters*, vol. 31(24), 2097–2098, 1995.

[34] P. Trinh, S. Yegnanarayanan, F. Coppinger, and B. Jalali, Silicon-on-insulator (soi) phased-array wavelength multi/demultiplexer with extremely low-polarization sensitivity, *IEEE Photonics Technology Letters*, vol. 9(7), 940–942, 1997.

[35] Q. Xu, B. Schmidt, S. Pradhan, and M. Lipson, Micrometre-scale silicon electro-optic modulator, *nature*, vol. 435(7040), 325–327, 2005.

[36] A. Liu, R. Jones, L. Liao, D. Samara-Rubio, D. Rubin, O. Cohen, R. Nicolaescu, and M. Paniccia, A high-speed silicon optical modulator based on a metal–oxide–semiconductor capacitor, *Nature*, vol. 427(6975), 615–618, 2004.

[37] S. Y. Siew, B. Li, F. Gao, H. Y. Zheng, W. Zhang, P. Guo, S. W. Xie, A. Song, B. Dong, L. W. Luo, *et al.*, Review of silicon photonics technology and platform development, *Journal of Lightwave Technology*, vol. 39(13), 4374–4389, 2021.

[38] A. E.-J. Lim, J. Song, Q. Fang, C. Li, X. Tu, N. Duan, K. K. Chen, R. P.-C. Tern, and T.-Y. Liow, Review of silicon photonics foundry efforts, *IEEE Journal of Selected Topics in Quantum Electronics*, vol. 20(4), 405–416, 2013.

[39] C. Xiang, J. Guo, W. Jin, L. Wu, J. Peters, W. Xie, L. Chang, B. Shen, H. Wang, Q.-F. Yang, *et al.*, High-performance lasers for fully integrated silicon nitride photonics, *Nature communications*, vol. 12(1), 6650, 2021.

[40] M. A. Green, J. Zhao, A. Wang, P. J. Reece, and M. Gal, Efficient silicon light-emitting diodes, *Nature*, vol. 412(August), 805–808, 2001.

[41] J. Michel, J. Liu, and L. C. Kimerling, High-performance ge-on-si photodetectors, *Nature photonics*, vol. 4(8), 527–534, 2010.

[42] M. Piels and J. E. Bowers, Photodetectors for silicon photonic integrated circuits, *Photodetectors*, 419–436, 2023.

[43] H. Chen, P. Verheyen, P. De Heyn, G. Lepage, J. De Coster, S. Balakrishnan, P. Absil, G. Roelkens, and J. Van Campenhout, Dark current analysis in high-speed germanium p-i-n waveguide photodetectors, *Journal of Applied Physics*, vol. 119(21), 2016, ISSN: 10897550.

[44] J. J. Ackert, D. J. Thomson, L. Shen, A. C. Peacock, P. E. Jessop, G. T. Reed, G. Z. Mashanovich, and A. P. Knights, High-speed detection at two micrometres with monolithic silicon photodiodes, *Nature Photonics*, vol. 9(6), 393–396, 2015, ISSN: 17494893.

[45] D. F. Logan, P. Velha, M. Sorel, R. M. De La Rue, A. P. Knights, and P. E. Jessop, Defect-enhanced silicon-on-insulator waveguide resonant photodetector with high sensitivity at 1.55 μm, *IEEE Photonics Technology Letters*, vol. 22(20), 1530–1532, 2010.

[46] J. D. B. Bradley, P. E. Jessop, and A. P. Knights, Silicon waveguide-integrated optical power monitor with enhanced sensitivity at 1550nm, *Applied Physics Letters*, vol. 86(24), 241 103, 2005, ISSN: 0003-6951.

[47] D. H. Hagan, Y. Xie, R. Das, A. S. Kashi, J. C. Cartledge, and A. P. Knights, Modification of the electrical properties of a silicon waveguide avalanche photodetector operating at 1550 nm via defect engineering, *Journal of Lightwave Technology*, vol. 42(2), 704–712, 2024.

[48] D. F. Logan, P. E. Jessop, and A. P. Knights, Modeling defect enhanced detection at 1550 nm in integrated silicon waveguide photodetectors, *Journal of Lightwave Technology*, vol. 27(7), 930–937, 2009.

[49] Y. Gao, F. Guo, P. Mascher, and A. P. Knights, Monolithic silicon avalanche photodetector utilizing surface state defects operating at 1550 nm, in *Silicon Photonics XVIII*, SPIE, vol. 12426, 2023, 61–65.

[50] R. J. Mears, L. Reekie, I. Jauncey, and D. N. Payne, Low-noise erbium-doped fibre amplifier operating at 1.54 μm, *Electronics Letters*, vol. 19(23), 1026–1028, 1987.

[51] Y. Liu, Z. Qiu, X. Ji, A. Lukashchuk, J. He, J. Riemensberger, M. Hafermann, R. N. Wang, J. Liu, C. Ronning, *et al.*, A photonic integrated circuit–based erbium-doped amplifier, *Science*, vol. 376(6599), 1309–1313, 2022.

[52] D. Nikolova, S. Rumley, D. Calhoun, Q. Li, R. Hendry, P. Samadi, and K. Bergman, Scaling silicon photonic switch fabrics for data center interconnection networks, *Optics Express*, vol. 23(2), 1159–1175, 2015.

[53] R. Brinkmann, I. Baumann, M. Dinand, W. Sohler, and H. Suche, Erbium-doped single and double pass Ti:$LiNbO_3$ waveguide amplifiers, *IEEE journal of quantum electronics*, vol. 30(10), 2356–2360, 1994.

[54] H. Suche, I. Baumann, D. Hiller, and W. Sohler, Modelocked Er: Ti:$LiNbO_3$ waveguide laser, *Electronics Letters*, vol. 29(12), 1111–1112, 1993.

[55] J. Zhou, Y. Liang, Z. Liu, W. Chu, H. Zhang, D. Yin, Z. Fang, R. Wu, J. Zhang, W. Chen, *et al.*, On-chip integrated waveguide amplifiers on erbium-doped thin-film lithium niobate on insulator, *Laser & Photonics Reviews*, vol. 15(8), 2 100 030, 2021.

[56] S. A. Vazquez-Cordova, M. Dijkstra, E. H. Bernhardi, F. Ay, K. Worhoff, J. L. Herek, S. M. Garcia-Blanco, and M. Pollnau, Erbium-doped spiral amplifiers with 20 dB of net gain on silicon, *Optics Express*, vol. 22(21), 25 993–26 004, 2014.

[57] J. Ronn, W. Zhang, A. Autere, X. Leroux, L. Pakarinen, C. Alonso-Ramos, A. Saynatjoki, H. Lipsanen, L. Vivien, E. Cassan, *et al.*, Ultra-high on-chip optical gain in erbium-based hybrid slot waveguides, *Nature communications*, vol. 10(1), 432, 2019.

[58] J. Mu, M. Dijkstra, J. Korterik, H. Offerhaus, and S. M. Garcia-Blanco, High-gain waveguide amplifiers in Si_3N_4 technology via double-layer monolithic integration, *Photonics Research*, vol. 8(10), 1634–1641, 2020.

[59] K. Worhoff, J. D. B. Bradley, F. Ay, D. Geskus, T. P. Blauwendraat, and M. Pollnau, Reliable Low-Cost Fabrication of Low-Loss Al_2O_3:Er^{3+} Waveguides With 5.4-dB Optical Gain, *IEEE Journal of Quantum Electronics*, vol. 45(5), 454–461, 2009.

[60] J. Bradley, L. Agazzi, D. Geskus, F. Ay, K. Worhoff, and M. Pollnau, Gain bandwidth of 80 nm and 2 dB/cm peak gain in Al_2O_3: Er^{3+} optical amplifiers on silicon, *JOSA B*, vol. 27(2), 187–196, 2010.

[61] A. Z. Subramanian, G. S. Murugan, M. N. Zervas, and J. S. Wilkinson, High index contrast Er: Ta_2O_5 waveguide amplifier on oxidised silicon, *Optics Communications*, vol. 285(2), 124–127, 2012.

[62] Z. Zhang, R. Liu, W. Wang, K. Yan, Z. Yang, M. Song, D. Wu, P. Xu, X. Wang, and R. Wang, On-chip Er-doped Ta_2O_5 waveguide amplifiers with a high internal net gain, *Optics Letters*, vol. 48(21), 5799–5802, 2023.

[63] K. Vu and S. Madden, Tellurium dioxide erbium doped planar rib waveguide amplifiers with net gain and 2.8 db/cm internal gain, *Optics Express*, vol. 18(18), 19 192–19 200, 2010.

[64] K. Vu, S. Farahani, and S. Madden, 980nm pumped erbium doped tellurium oxide planar rib waveguide laser and amplifier with gain in S, C and L band, *Optics Express*, vol. 23(2), 747–755, 2015.

[65] H. C. Frankis, H. M. Mbonde, D. B. Bonneville, C. Zhang, R. Mateman, A. Leinse, and J. D. B. Bradley, Erbium-doped TeO_2-coated Si_3N_4 waveguide amplifiers with 5 dB net gain, *Photonics Research*, vol. 8(2), 127–134, 2020.

Chapter 2

Background

This chapter provides an overview of the Silicon Photonics (SiP) platform and the devices examined in this thesis. Initially, in Section 2.1, we introduce the silicon-on-insulator (SOI) platform, highlighting the essential characteristics of silicon waveguides utilized within this framework. Following that, Section 2.2 delves into the theoretical background of light propagation in integrated waveguides, exploring various waveguide structures and material systems. Section 2.3 offers a concise summary of the mechanisms for detecting light on the silicon photonics platform. Lastly, Section 2.4 discusses erbium-doped waveguide amplifiers, covering the mechanism of erbium luminescence and the integration of erbium into the waveguide matrix.

2.1 Silicon photonics platform

Integrated photonics provide a solution for optical systems with increased bandwidths, lower power consumption, and compact volumes [1]. Silicon photonics, as one of the most promising platforms for integrated photonics, is attracting increasing research interest due to its compatibility with CMOS foundry processes. Other than optical communication, silicon photonics can be applied to various fields including sensing [2, 3], optical phase array [4], optical computing [5], and quantum optics [6]. The silicon photonics

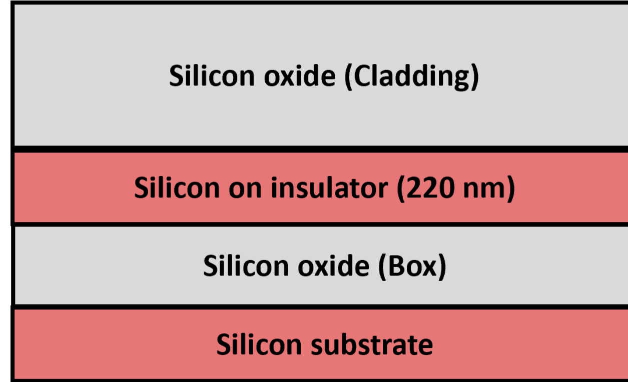

FIGURE 2.1: Cross-section view of the silicon-on-insulator (SOI) wafer.

platform can provide performance that cannot be achieved with free-space discrete components [7]. The component libraries of the silicon photonics platform have been actively expanded to active components such as high-speed modulators [8, 9], switches [10, 11], detectors [12–15], and even lasers [16, 17] to passive components such as 3dB couplers [18], directional couplers [19], and waveguide crossings [20].

The typical silicon photonics wafer composition is depicted in Fig. 2.1. In a silicon photonics multi-project wafer (MPW) process based on deep-ultraviolet lithography, the silicon-on-insulator (SOI) <100> wafers with a silicon thickness of 220 nm are etched to form waveguides structures over buried oxide. A silicon substrate wafer on the bottom is used to provide mechanical robustness to the overall system. Silicon on insulator with different thickness have been reported for various applications [21], but a height of 220 nm is considered as standard since the early 2000s [22]. Lastly, a top oxide cladding is applied to the overall structure to protect the silicon structures.

2.2 Waveguide theory

2.2.1 Electromagnetic wave propagation

Electromagnetic waves propagating in a dielectric medium containing no free charges and no current are governed by the Maxwell's Equations. In a linear, homogeneous and

isotropic medium without any free electric charges, Maxwell's equations can be written in the following form [23]:

$$\nabla E = 0 \tag{2.1}$$

$$\nabla H = 0 \tag{2.2}$$

$$\nabla \times E = -\mu \frac{\partial H}{\partial t} \tag{2.3}$$

$$\nabla \times H = \sigma E + \epsilon \frac{\partial E}{\partial t} \tag{2.4}$$

where $\mathbf{H}$ is the magnetic vector field, $\mathbf{E}$ is the electric vector field, ϵ is the dielectric permittivity, μ is the magnetic permeability and σ is the conductivity of the medium.

By combining equations 2.1 to 2.4, and assuming a perfect dielectric medium where conductivity $\sigma = 0$, the wave equations for the material medium can be obtained:

$$\nabla^2 \mathbf{E} = \mu\epsilon \frac{\partial^2 \mathbf{E}}{\partial t^2} \tag{2.5}$$

$$\nabla^2 \mathbf{H} = \mu\epsilon \frac{\partial^2 \mathbf{H}}{\partial t^2} \tag{2.6}$$

Each of these two wave equations can be separated on three scalar wave equations, expressed as:

$$\nabla^2 E = \mu\epsilon \frac{\partial^2 E}{\partial t^2} \tag{2.7}$$

where the $E(\mathbf{r}, t)$ can represent each of the Cartesian components of either the electric fields. The solution of this equation represents a wave that propagates with a speed v (phase velocity) given by:

$$v = \frac{1}{\sqrt{\epsilon\mu}} \tag{2.8}$$

For electromagnetic waves propagating in free space, and using $\epsilon_0 = 8.85 \times 10^{-12} m^{-3} kg^{-1} s^4 A^2$ and $\mu_0 = 4\pi \times 10^{-7} mkgs^{-2} A^{-2}$, we can obtain the speed of light in free space:

$$c = \frac{1}{\sqrt{\epsilon_0 \mu_0}} \approx 3 \times 10^8 \text{ m/s} \tag{2.9}$$

The refractive index of a dielectric medium is related to the optical constant of the material medium and the dielectric permittivity and the magnetic permeability of free space, and it is by defined as:

$$n = \sqrt{\frac{\epsilon \mu}{\epsilon_0 \mu_0}} \tag{2.10}$$

where the magnetic permeability is very close to that of free space in most of the non-magnetic materials. Therefore, the refractive index expression can be simplified:

$$n \approx \sqrt{\frac{\epsilon}{\epsilon_0}} = \sqrt{\epsilon_r} \tag{2.11}$$

In a certain dielectric medium, the propagation speed of the electromagnetic waves v is expressed as a function of the speed of light in free space c through the following relation:

$$v = \frac{c}{n} \tag{2.12}$$

A general solution to Eq. (2.5) can be obtained as sinusoidal wave functions :

$$\mathbf{E}(\mathbf{r}, t) = \mathbf{E}_0 e^{i(k \cdot \mathbf{r} - \omega t)} \tag{2.13}$$

where $\mathbf{E}(\mathbf{r})$ is the electric field of the wave; $\mathbf{r}$ is a vector in Cartesian (x, y, z) coordinates, and t is time. The parameter ω is the angular frequency (radians per second).

The wavevector $\mathbf{k}$ describes the spatial periodic variation of electric field in the wave propagation. In isotropic materials, $\mathbf{k}$ is perpendicular to both $\mathbf{E}$ and $\mathbf{H}$, making the light wave transverse [23].

For a plane wave travelling in the z direction, made by setting $\mathbf{E}_0$ as a constant vector in the xy plane and setting $\mathbf{k}$ to be parallel to z with a magnitude of k, the solution would be:

$$\mathbf{E}(z,t) = \mathbf{E}_0 e^{i(kz-\omega t)} \tag{2.14}$$

The magnitude of the wavevector can be determined:

$$k = \frac{\omega n}{c_0} = k_0 n \tag{2.15}$$

where k_0 is defined as the wavevector in free-space. Then wavelength λ can be defined as:

$$\lambda = \frac{2\pi}{k} = \frac{\lambda_0}{n} \tag{2.16}$$

The Poynting Vector is defined as:

$$\vec{S} = \vec{E} \times \vec{H} \tag{2.17}$$

And the intensity I of an electromagnetic wave is defined as:

$$I = \langle |\vec{S}| \rangle \tag{2.18}$$

Note that the unit for the intensity is power per unit area (W/cm^2). To calculate the total optical power, one just needs to integrate the intensity over the total area.

2.2.2 Electromagnetic waves in a 2-D slab waveguide

Waveguides, which are used to confine and guide optical waves, are considered the core element in a photonic integrated circuit. A waveguide often consists of propagating mediums with different refractive indices, where the core has a higher index than the cladding, as shown in Fig. 2.2 ($n_2 > n_1$ and $n_2 > n_3$). In this case, electromagnetic waves can be confined in the higher index region by total internal reflection. The ray

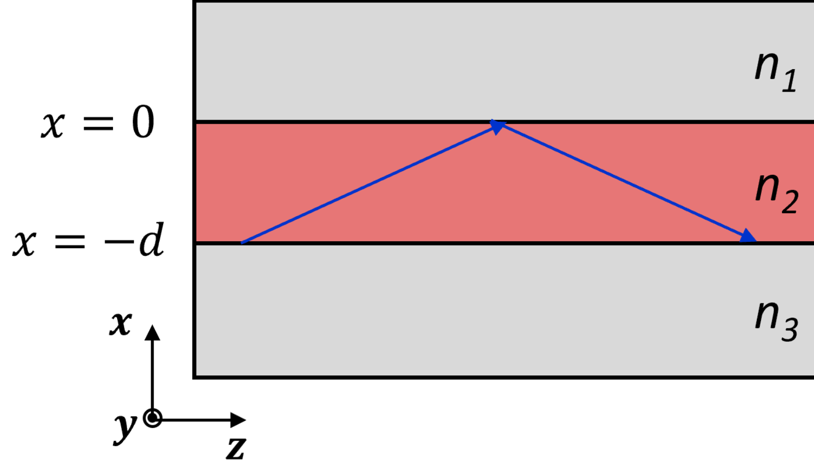

FIGURE 2.2: Total internal reflection for a guided mode in a slab waveguide.

optics of this phenomenon can be described by Snell's Law of refraction and the law of reflection [24]:

$$n_a \sin\theta_a = n_b \sin\theta_b \tag{2.19}$$

$$\theta_a = \theta_r \tag{2.20}$$

where θ_a, θ_r, and θ_b are the angles of incidence, reflection, and refraction, respectively. In Fig. 2.2, the structure consists of three homogeneous dielectric layers with z axis extending to infinity. The scalar wave equation can be given by:

$$\left(\frac{\partial^2}{\partial x^2} + \frac{\partial^2}{\partial y^2}\right) E(x,y) + \left(k_0^2 n - \beta^2\right) E(x,y) = 0 \tag{2.21}$$

where k_0 is the wavenumber in vacuum and β is the propagation constant in the z-direction. The effective index n_{eff}, which is used to describe the propagation of light in a non-homogeneous medium, can be defined:

$$n_{\mathrm{eff}} = \frac{\beta}{k_0} \tag{2.22}$$

An optical mode refers to the pattern of electromagnetic field distribution in the transverse plane due to the boundary conditions of the waveguide structure. Waveguides often support a discrete number of optical modes with distinctive propagation constant β :

$$\beta = k_0 n_{eff} \tag{2.23}$$

The transverse electrical (TE) mode is the mode profile along the x axis when the polarization of the electric field is parallel to the y axis. The electric field amplitude for TE modes can be expressed [23]:

$$E_y^m(x) = \begin{cases} C\exp(-qx), & x \geq 0 \\ C\left(\cos(hx) - \frac{q}{h}\sin(hx)\right), & -d \leq x \leq 0 \\ C\left(\cos(hd) + \frac{q}{h}\sin(hd)\right)\exp\left(p(x+d)\right), & x \leq -d \end{cases} \tag{2.24}$$

where m stands for the m-th mode, d is the thickness of the core layer, c is a normalization constant and h, q, p are defined as [23]:

$$\begin{aligned} h &= \left[(n_2 k_0)^2 - (n_{\text{eff}} k_0)^2\right]^{1/2}, \\ q &= \left[(n_{\text{eff}} k_0)^2 - (n_1 k_0)^2\right]^{1/2}, \\ p &= \left[(n_{\text{eff}} k_0)^2 - (n_3 k_0)^2\right]^{1/2}. \end{aligned}$$

The H-field amplitude is then derived as:

$$H_z^m(x) = i\omega\mu \begin{cases} -qC\exp(-qx), & x \geq 0 \\ C(-h\sin(hx) - q\cos(hx)), & -d \leq x \leq 0 \\ pC\left(\cos(hd) + \frac{q}{h}\sin(hd)\right)\exp(p(x+d)), & x \leq -d \end{cases} \tag{2.25}$$

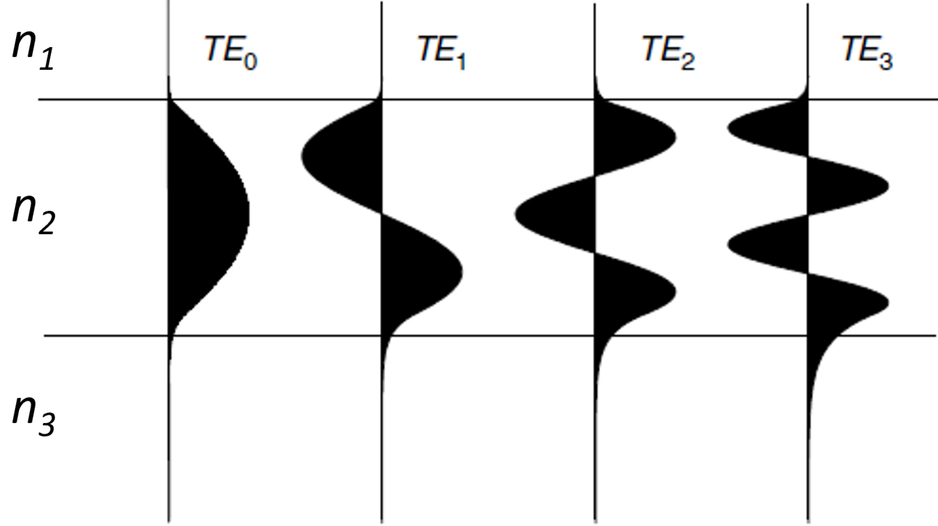

FIGURE 2.3: TE modes in an asymmetric step-index planar waveguide [23].

Using the boundary condition that both E-field and H-field must be continuous at the interfaces $x = 0$ and $x = -d$, the mode-condition eigenfunction can be obtained:

$$\tan(hd) = \frac{p + q}{h(1 - pq/h^2)} \tag{2.26}$$

which admits a finite number of solutions for a finite number of integer m, meaning the waveguide will support a finite number of guided modes. If the waveguide supports only one mode for $m = 0$, the waveguide is called a single mode waveguide, otherwise it's referred to as a multi-mode waveguide. Figure 2.3 demonstrates 4 solutions for TE-mode in a structure shown in Fig. 2.2. Each mode shows a standing wave in the transverse plane. Normally the effective index will increase as the mode order increases due to the expanded mode size. The electric field in the top and bottom regions are referred to as evanescent waves where the propagating light attenuates exponentially in the evanescent field.

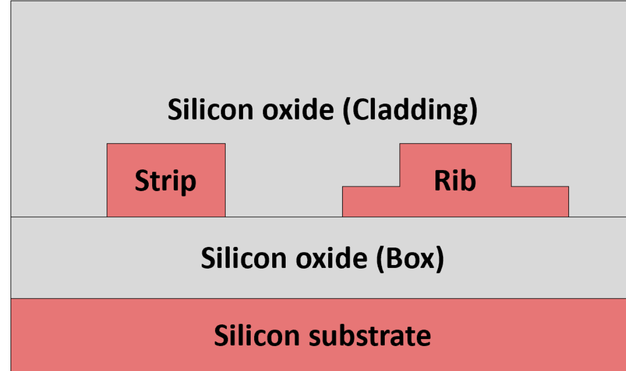

FIGURE 2.4: Two types of frequently used waveguides on SOI platform.

2.2.3 Light propagating in SOI waveguide

There are several types of waveguides commonly used in silicon photonics integrated circuits. Fig. 2.4 shows the two types of most commonly used waveguides. The strip waveguide typically has a cross section dimension of 220 nm in height and 500 nm in width to support single mode operation. It is also used for routing due to its tight bend radii from the high effective index. The rib waveguide (also known as ridge waveguide), is used to build P-N junctions to form modulators and photodetectors. The strip waveguide is simulated using Ansys Lumerical MODE Solutions [25] to solve for the fundamental TE mode, with the structure shown in Fig. 2.4 left. The mode profile at 1550 nm is shown in Fig. 2.5, where most of the electric field is concentrated in the center of the waveguide with a symmetrical distribution. The effective index and group index at 1550 nm are calculated to be 2.45 and 4.18, respectively. Despite the mode concentrating in the center, optical field still leaks out via the waveguide boundary, forming the evanescent fields. These fields can be interacting with the surrounding environment such as rare earth dopants in the top cladding and surface state defects at the Si/SiO_2 interface, as described in more detail in the forthcoming chapters. Besides, the evanescent fields can be coupled into adjacent waveguide mediums, which can be utilized for coupling light between adjacent waveguides and transiting light between two different waveguide types (e.g. strip to ridge waveguide).

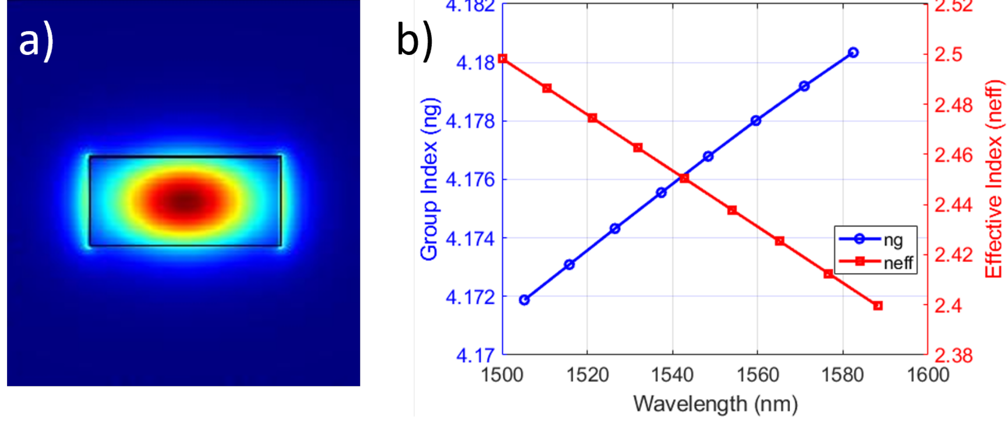

FIGURE 2.5: Simulated (a) mode profile, and (b) and effective index and group index of a waveguide with 220 nm height and 500 nm width at 1550 nm.

To introduce light to a waveguide, it is required to couple light from an optical fiber to a edge coupler on an integrated chip since optical fibers typically have a larger mode field diameter (MFD) compared to the much smaller waveguides on a chip. An edge coupler is needed to match these modes as closely as possible to maximize coupling efficiency. This often involves tapering the waveguide to gradually transform the mode profile to more closely match that of the fiber. The waveguide on the chip tapers down from a larger cross-sectional area (e.g. 220 nm by 500 nm) near the edge of the chip to a smaller cross-section (220 nm by 140 nm). This tapering is designed to gradually adapt the mode size of the incoming light from the fiber to the mode size of the on-chip waveguide. With a linearly tapered edge coupler, the coupling loss is around 1.5 dB per facet. Subwavelength grating edge couplers are able to increase the coupling efficiency by decreasing the effective index of the waveguide, thus expanding the mode size to better match the mode of the optical fiber. However, the light often needs to be transitioned to conventional waveguides to process the optical signal, causing extra loss in the mode conversion. Therefore, a conventional linearly tapered edge coupler is used for all the devices in this thesis.

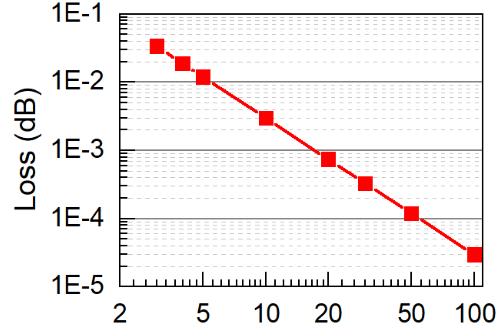

FIGURE 2.6: Simulated bending loss as a function of bending radius (μm) for the strip waveguide shown in Fig. 2.4.

Waveguide bends are usually required for routing. The minimum bending radius is carefully determined to balance compactness and the bending loss. In a bend, the light has inertia to keep propagating straight, thus causing mode leakage towards the outer side, increasing the propagation loss. To solve for an optimal bending radius for a conventional single mode strip waveguide (Fig. 2.4), waveguide bends with different radii were simulated in Ansys MODE Solutions [25], where the corresponding bending loss is extracted from the mode mismatch between the mode in a bend and the mode in a straight waveguide. Fig. 2.6 shows the simulated bending loss as a function of bending radius for the strip waveguide. A bending radius of over 10 µm is normally required to minimize the bending loss while maintaining compact circuits.

2.2.4 Group index and slow light

The phase term of the sinusoidal electromagnetic wave is expressed as $e^{-i(kz-\omega t)}$ traveling in the $\hat{z}$ direction. The speed of the wave front point stays constant as:

$$z(t) = \frac{\omega t}{k} + \text{constant} \tag{2.27}$$

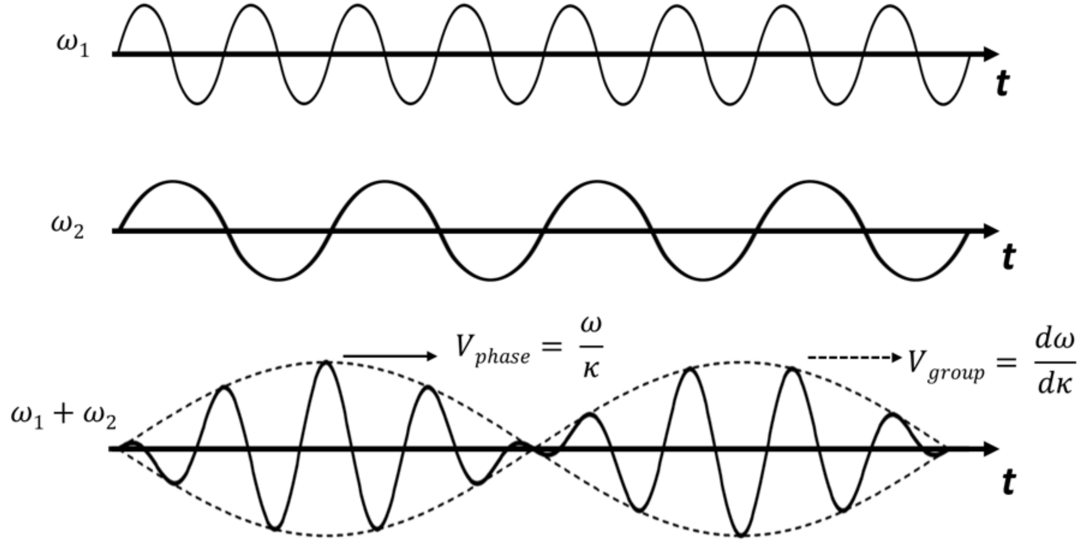

FIGURE 2.7: Wave packet composed of two frequency components.

The phase velocity v_p can be defined by taking the derivative of Eq. 2.27 with respect to time t:

$$v_p = \frac{dz}{dt} = \frac{\omega}{k} \tag{2.28}$$

In optical communication applications, light always travels as a wave packet. A wave packet is a localized collection of waves superimposed in a coherent manner, such that individual wave components with different frequencies and wavelengths combine to form a pulse with a finite spatial extent. Mathematically, a wave packet can be represented as an integral over a range of frequencies of plane waves, each with its own amplitude, phase, and frequency, following the Fourier synthesis.

A wave packet with two waves with different angular frequencies ($\omega_1 = \omega + \Delta\omega$, $\omega_2 = \omega - \Delta\omega$) is shown in Fig. 2.7. The electric field superposition can be written as follow:

$$E_1 + E_2 = 2E_0 \cos(\omega t - kz) \cos(\Delta\omega t - \Delta kz) \tag{2.29}$$

where E_1 and E_2 are the electric field of the two waves, E_0 is the addition of the amplitude of the two waves, and Δk is the wavevector difference. The group velocity v_g describes the speed of the wave packet (envelope), described by $\cos(\Delta\omega t - \Delta kz)$. If we study a point on the envelope, the speed of this point is constrained, such that its phase should be constant. Therefore we can obtain the group velocity v_g by taking first-order derivative of $z(t) = \Delta\omega t/\Delta k + \text{constant}$:

$$v_g = \frac{dz}{dt} = \frac{\Delta\omega}{\Delta k} = \frac{d\omega}{dk} \tag{2.30}$$

Group delay τ_g is defined as the reciprocal of the group velocity:

$$\tau_g = \frac{1}{v_g} = \frac{dk}{d\omega} \tag{2.31}$$

Substituting $k = \frac{n_{\text{eff}}\omega}{c}$ into Eq. 2.31, the group delay can be expressed as:

$$\tau_g = \frac{d\left(\frac{n_{\text{eff}}\omega}{c}\right)}{d\omega} = \frac{n_{\text{eff}} + \omega\frac{dn_{\text{eff}}}{d\omega}}{c} \tag{2.32}$$

By inverting Eq. 2.32, v_g is expressed as:

$$v_g = \frac{c}{n_{\text{eff}} + \omega\frac{dn_{\text{eff}}}{d\omega}} \tag{2.33}$$

We can obtain the group index n_g as:

$$n_g = n_{\text{eff}} + \omega\frac{dn_{\text{eff}}}{d\omega} = n_{\text{eff}} - \lambda\frac{dn_{\text{eff}}}{d\lambda} \tag{2.34}$$

Physically, the group velocity is often associated with the transport of energy and information, since it defines the speed at which changes to the wave packet's shape (modulations) travel. This is of particular importance in communication systems where signal integrity must be maintained over long distances.

In a dispersive medium, which is common in PICs, different frequency components of a wave packet travel at different phase velocities due to the material's refractive index's dependence on frequency. This dispersion leads to the spreading of the wave packet as it propagates, with the group velocity deviating from the phase velocity.

Slow light in photonic integrated circuits represents a regime where the group velocity of light is substantially reduced from its speed in a vacuum. Achieving slow light involves engineering materials or waveguide structures that exhibit strong dispersion, a property where the refractive index changes quickly with the light's wavelength. Photonic crystal waveguides, which incorporate periodic structures, are one such approach to induce slow light. These structures create photonic bandgaps that alter how light travels within the medium, particularly at the bandgap edges where the group velocity can drop significantly.

The advantage of slow light is the enhanced interaction between light and the medium it traverses. This longer interaction time can be exploited to boost the efficiency of various optical processes within PICs. For example, the effectiveness of modulators and switches is improved, benefiting from the stronger light-matter interactions to achieve the same modulation depth with lower power or achieve a more significant effect with the same power. Slow light also amplifies the material's nonlinear response, facilitating applications like harmonic generation, four-wave mixing, and parametric amplification, which are foundational to many advanced optical processing techniques.

In the realm of sensing, the slow light effect provides a distinct advantage. It enables the design of highly sensitive on-chip sensors capable of detecting minute changes in environmental conditions, such as slight variations in refractive index or the presence of trace amounts of biological or chemical substances. Moreover, slow light can be utilized to construct compact optical delay lines, offering a means to synchronize light signals in dense PICs or to implement optical buffering strategies, critical for managing data flows

in optical communication systems.

However, slow light technology also faces several challenges that must be addressed. For instance, as light slows down, it tends to experience increased absorption and scattering losses, which can diminish the intensity of the signal. Additionally, the slow light effect often occurs over a narrow bandwidth, which limits the range of frequencies that can be effectively slowed. Moreover, the temporal spreading of optical pulses, known as group velocity dispersion, can lead to signal distortion, posing a problem for maintaining signal integrity over long propagation distances. Finding a balance between the desirable effects of slow light and its inherent limitations can harness its potential for creating more capable and multifunctional photonic integrated circuits.

2.2.5 Subwavelength grating waveguide

On photonic integrated circuits, subwavelength grating (SWG) waveguide structures are a pivotal technology that manipulate light in ways that conventional waveguides cannot. They exploit the phenomenon of diffraction to achieve various functionalities. In a PIC, an SWG can be used to create highly efficient couplers, filters, or even to engineer the dispersion properties of waveguides. By altering the duty cycle, period, and height of the grating elements, designers can control the effective refractive index experienced by the light. This enables the creation of waveguides with engineered dispersion for specific phase-matching conditions, essential in nonlinear optical applications such as wavelength conversion and supercontinuum generation. One of the compelling applications of SWGs in PICs is in the realization of broadband optical couplers. These components are designed to efficiently couple light between the sub-micron scale waveguides of silicon photonics and the larger optical fibers used in telecommunications.

SWGs can provide a gradual transition in the effective refractive index, which facilitates mode-matching and reduces coupling losses significantly. These structures consist

of periodic patterns with features much smaller than the wavelength of the light propagating through them, which form an array of Rayleigh scatterers [26]. The periodicity of the grating creates a new effective medium for the light, with properties that can be precisely engineered by adjusting the grating's parameters.

In the SWG regime, the waveguide structure is optically equivalent to a uniaxial crystal with optic axis parallel to the propagation direction [27]. The refractive index of the homogeneous waveguide can be estimated using the homogenization or effective-medium theory [28]:

$$n^2 \approx \frac{a}{\Lambda} n_1^2 + \left[1 - \frac{a}{\Lambda}\right] n_2^2 \tag{2.35}$$

where a is the width of a slab of material with index n_1, n_2 is the index of the material in the gaps, Λ is the grating period and λ is the free-space wavelength as shown in Fig. 2.8 (a).

As demonstrated in Fig. 2.8 (b), the dispersion relation governs the light propagation in a grating structure where three regimes can be divided based on the angular frequency of the propagating light for a certain period, the subwavelength, optical bandgap (Bragg), and the radiation regimes [26]. In the optical bandgap, Bragg resonance occurs and no mode is allowed to propagate within the structure and the intensity of the light will decay exponentially due to optical reflection. In the radiation regime, the waveguide structure works like a diffraction grating, radiating the optical power into the surrounding cladding around the waveguide (shown in Fig. 2.8 (c) top). In the SWG regime, where the period is much smaller than the propagating wavelength, Floquet-Bloch modes are allowed to propagate without loss according to Bloch's theorem. Fig. 2.8 (c) bottom shows the electric field profile of light travelling in deep the SWG regime, where the photonic crystal can be considered as a homogeneous waveguide.

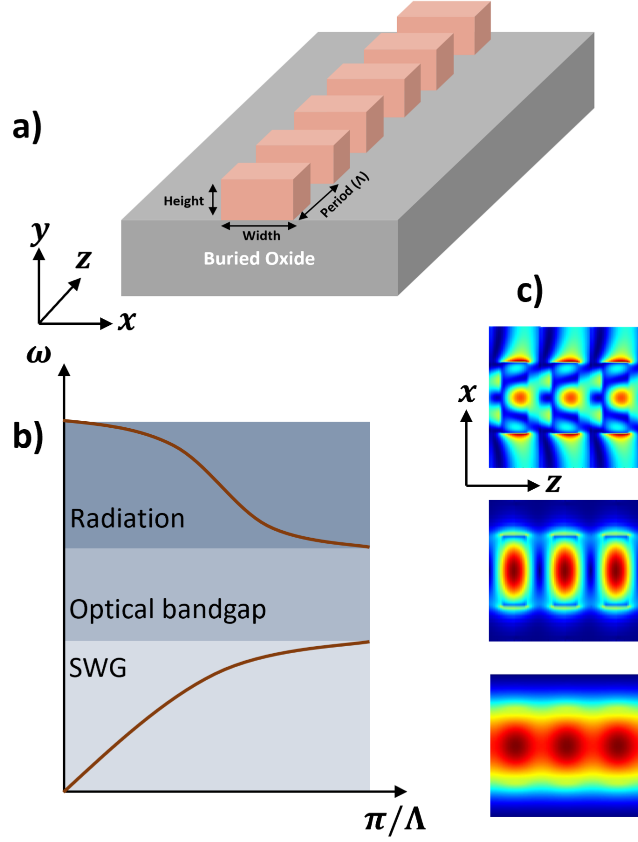

FIGURE 2.8: a), Silicon-on-insulator slab waveguide with etched SWG, for light propagation along the z axis. Schematic dispersion diagram (b) and simulated electric field profiles (c) of radiation regime (top), slow light regime (middle), and deep SWG regime (bottom).

From [29], the group index can be calculated as:

$$n_g = c\frac{\partial K}{\partial \omega} \tag{2.36}$$

with K being the dispersion relation. Close to the optical bandgap, the dispersion relation becomes flat, indicating an increased group index (slow light). In theory the group index can approach infinity, however, due to the increased propagation loss, this group index can not be observed in experiments. In this thesis, we consider the slow light regime when the group index is greater than 10.

2.2.6 Waveguide material systems

Crystalline silicon and silicon nitride are two prominent materials used in the fabrication of waveguides on a silicon photonics platform, and they each have unique properties that make them suitable for different applications within the field of integrated optics.

Silicon

Silicon waveguides stand out in photonic integrated circuits due to their compatibility with established CMOS fabrication processes which significantly reduces manufacturing costs and paves the way for seamless integration with electronic components. As the demand increases for high-bandwidth communication applications, co-packaged optics (CPO) is considered as the technology addressing next generation bandwidth and power challenges, where heterogeneous integration of optics and silicon on a single packaged substrate is realized. Silicon allows for the integration of both passive (e.g., waveguides, couplers, multiplexers) and active (e.g., modulators, detectors) devices on the same substrate. This integration is key for creating a complete optical link within a co-packaged module.

Silicon has high refractive index, enabling tight light confinement and compact designs. Optimal for near-infrared (NIR) applications, particularly around the 1.55 µm telecom band, silicon's transparency in this range allows for efficient light transmission with minimal losses. Its strong nonlinear optical properties, while beneficial for certain all-optical signal processing tasks, can introduce challenges such as two-photon absorption at high power levels. Additionally, silicon's significant thermo-optic effect requires careful thermal management but also enables tunable photonic devices including thermal phase shifters and thermo-optic modulators.

Silicon nitride

Silicon nitride offers a broad transparency window extending from the visible to the infrared, associated with lower refractive index and propagation losses, making it a versatile choice for a variety of photonic applications, including those in biophotonics and spectroscopy. More importantly, it exhibits much lower optical propagation losses compared to Si waveguides. This low loss enables the transmission of light over longer distances within a chip without significant signal attenuation, which is crucial for applications requiring long optical path lengths, such as delay lines, on-chip spectroscopy, and sensing. Its low nonlinearity minimizes performance penalties under high-power light propagation, positioning it as a favorable material for linear optical components. Despite a lower thermo-optic coefficient than silicon, which confers more stable performance across temperature fluctuations, silicon nitride can still be processed in advanced CMOS facilities. Si_3N_4 waveguides can be integrated on top of other substrates, such as silicon, due to their lower temperature processing requirements, making it possible to combine the benefits of ultra-low loss SiN with the electronic integration capabilities of silicon. This positions Si_3N_4 as a material that combines performance stability with the manufacturing precision required for PICs that operate across a wide wavelength range and are less dependent on electronic-photonic integration.

2.2.7 Effective index method for mode solving

It is often needed to simulate how light propagates in the waveguide structures, especially when there are variations in the structure causing interference, scattering, integration, and mode expansion. The effective index method (EIM) is often used to obtain an analytical approximation of the mode.

The benefit of this method is that it can model large scale devices (hundreds of microns) with high efficiency [30]. In this method, a 3D geometry is simplified as a 2D

layout by collapsing the structure from the top view, with the assumption that the coupling between different slab modes is negligible. Initially, EIM solves for the waveguide's effective index in the vertical dimension, treating it as a slab waveguide in the horizontal plane. This effective index is then used to transform the original three-dimensional structure into an equivalent two-dimensional slab waveguide problem, which is subsequently solved to find the modes. By combining the solutions from the independent dimensional analyses, EIM provides an approximation of the original waveguide's modes. For enhanced accuracy, this process can be performed iteratively, using the fields obtained from the two-dimensional solution to refine the effective index and improve the solution's precision. This method is especially valuable for high-index-contrast waveguides with tightly confined fields, offering a balance between computational efficiency and solution accuracy. In this thesis, the EIM method is implemented in Lumerical MODE Solutions [25].

2.3 Photodetection

Photodetectors are key components in silicon photonics, designed to convert optical signals into electrical signals. They play a crucial role in optical communication systems, where they are used at the receiving end to detect and decode the light signals transmitted through optical fibers. In silicon photonics, photodetectors are integrated onto the same chip as other optical components, such as waveguides, modulators, and multiplexers, leading to compact, efficient, and high-speed optical circuits. In this section, we will discuss the optical absorption in SOI waveguides and different types of photodetectors used on the silicon photonics platform.

2.3.1 Optical absorption in SOI waveguides

Intrinsic absorption in silicon

With an indirect bandgap, the lowest energy point in the conduction band and the highest point of the valence band are offset, meaning a momentum transfer is needed through a phonon (lattice vibration) to make a photon cross the bandgap. Therefore, Si has a lower optical absorption coefficient compared to other semiconductor materials as shown in Fig. 2.9.

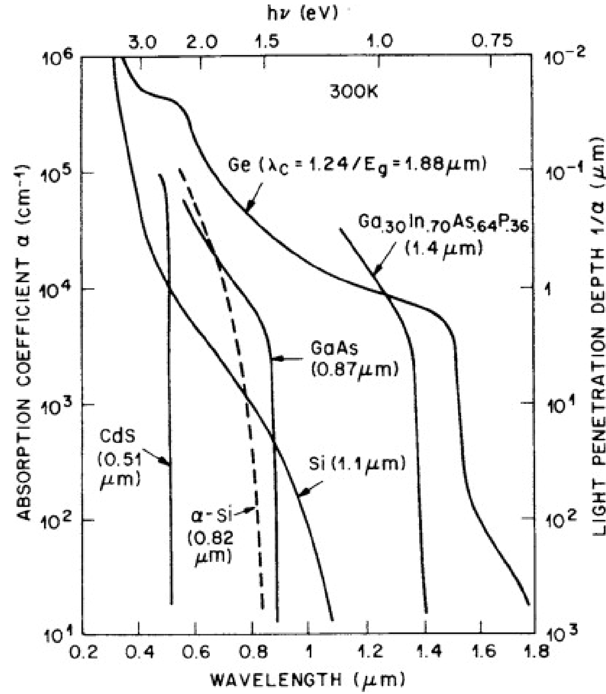

FIGURE 2.9: Optical absorption versus wavelength for various semiconductor materials [31] © 1985 John Wiley & Sons.

Silicon has a bandgap of $E_g = 1.12eV$, making it transparent to photons below this energy. The cut-off wavelength for silicon is calculated to be around 1.1 µm using:

$$\lambda_{cutoff} = \frac{hc}{E_g} \tag{2.37}$$

Approaches based on different sub-bandgap absorption mechanisms have been demonstrated to improve the response of all-silicon photodetectors at telecommunication wavelengths, including two-photon absorption (TPA), bulk defect absorption (BDA), and surface state absorption (SSA).

Two-photon absorption

TPA is a quantum mechanical process wherein two photons of lower energy (typically half the energy required to bridge the bandgap) are simultaneously absorbed by a material to excite an electron from a lower energy state (usually the valence band) to a higher energy state (such as the conduction band). Unlike traditional single-photon absorption, where the energy of a single photon matches the energy gap of the material, TPA requires the simultaneous absorption of two photons. When silicon is exposed to intense optical fields, such as those in tightly confined waveguides, the probability of simultaneous two-photon events increases, leading to measurable absorption even at wavelengths where silicon is otherwise transparent.

In the process of TPA, no intermediate but a "virtual state" is required, which does not correspond to any electronic energy state [32].During the absorption of the first photon, or while the electron's virtual state, created post-absorption of the first photon, exists, a phonon interaction would occur to satisfy the conservation of momentum in this indirect transition [33].

The TPA coefficienct β can be defined as [32]:

$$\beta(\omega) = \frac{3\pi}{c\varepsilon_0 n_0^2} \Im \left\{ \chi^{(3)} \right\} \tag{2.38}$$

where n_0 is the linear refractive index, ε_0 is the vacuum permittivity, λ is the wavelength of the incident optical beam, and $\chi^{(3)}$ is the third-order susceptibility.

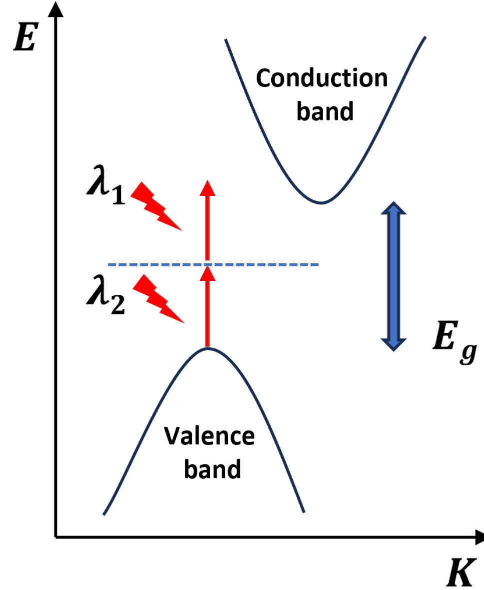

FIGURE 2.10: Band diagram of the two-photon absorption mechanism in Si.

One of the challenges with TPA-based photodetection is that it typically requires high optical powers, as the probability of two photons being absorbed simultaneously is lower than single-photon absorption. The silicon waveguides often carry light with optical power less than 1 mW (0 dBm), where the TPA effect can be negligible to the overall optical absorption, making it not ideal for small signal detection. Recent advancements focus on designing waveguides and resonant structures that enhance the optical intensity within the silicon, thereby increasing the TPA efficiency at lower power levels. Additionally, integrating other materials with stronger nonlinear properties or optimizing the photodetector design can further enhance TPA efficiency.

Bulk defect-mediated absorption

Mid-bandgap absorption can be achieved via BDA, where the defects can be introduced by ion implantation of foreign ions into the silicon crystal structure, producing divacancies as deep electronic levels in the silicon bandgap [34–38]. The tuneable concentration

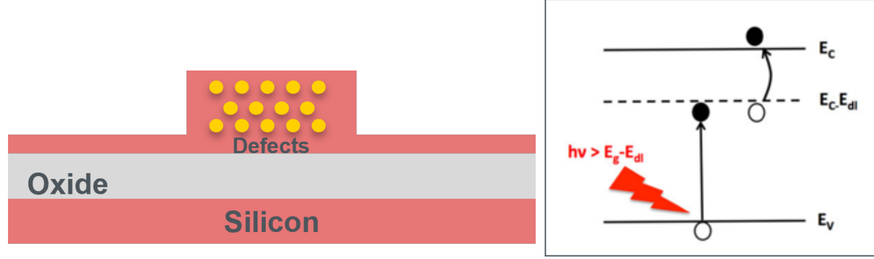

FIGURE 2.11: Cross-sectional view of BDA detectors (left) , and energy level diagram of BDA detectors (right) [32].

and the distribution of the implanted ions by controlling implantation dose and energy are considered the main advantages of this method.

As shown in Figure 2.11, after ion implantation, a deep level with a charge-state energy located below the conduction band can provide electron-hole pair generation through the two-step process. Firstly, the absorption of a photon excites an electron from the valence band into the deep level. Second, the electron is thermally excited from the deep level into the conduction band.

The rate ($cm^{-3}s^{-1}$) of electrons being excited from the valence band to an unoccupied deep level is given by [32]:

$$G_p^{opt} = I(x,y)\frac{1}{hv} - \alpha_d e^{-\alpha_d z} \tag{2.39}$$

with $I(x,y)$ being the optical intensity profile propagating in z direction, and $\alpha_d = \alpha_d(x,y,\lambda)$ referring to the optical absorption (at a given wavelength λ) due to the deep level, which has the form:

$$\alpha_d(x,y,\lambda) = \sigma_{opt}(\lambda)(1-f)N_t(x,y) \tag{2.40}$$

where σ_{opt} is the absorption cross-section (in cm^2), and $(1-f)$ is the fraction of deep levels in an unoccupied charge state [39].

For a photodetector utilizing the BDA effect, the responsivity due to the deep levels can be expressed as [32]:

$$R = e\eta\gamma = e\eta\left[\frac{\int G_p^{opt}(x, y, z)dV}{P_0}\right] \tag{2.41}$$

where η represents the efficiency of extracting generated carriers, including the influence of charge carrier lifetime, P_0 denotes the optical power within the active region of the photodetector, G_p^{opt} is the rate of electrons being excited from the valence band to an unoccupied deep level, and γ is characterized as the rate of electron-hole pair generation per second per watt. The rate γ is expressed as an integral that encompasses the spatial distribution of defects and the optical mode shape, accounting for the exponential decline in optical power at different positions due to absorption.

The generation of electron-hole pairs is influenced by several factors: 1) the concentration of deep-level defects, denoted as N_t, affecting G_p^{opt}; 2) the ambient temperature, which affects the rate of electron excitation from the deep levels to the conduction band; 3) the intensity of the optical field, I, where saturation of absorption occurs; and 4) the position of the Fermi level via the parameter f.

After undergoing thermal annealing at temperatures exceeding 200 °C, there is a gradual decrease in the excess optical loss, which is entirely eliminated at 350 °C [40], a temperature at which the divacancy is acknowledged to vanish [41]. Furthermore, the variation of the absorption coefficient with the Fermi level has been substantiated by optical loss evaluations conducted on samples with different levels of background phosphorus doping [41].

In 2006, Knights *et. al.* proposed a waveguide photodetector using ion implantation with a p-i-n diode configuration, reaching a responsivity of 9 mA/W [34]. The responsivity of this silicon photodetector was enhanced with ring resonators fabricated

with electron-beam lithography, reaching a responsivity of 39 mA/W at 20 volts reverse bias[36]. Similar devices with fast operation (35 GHz) were fabricated and characterized to have responsivity of 1-2 A/W at 20 volts by Geis *et al.*[42].

Surface state defect-mediated absorption

In addition to bulk defects in the silicon lattice introduced from ion implantation, surface state defects can be formed by un-passivating the silicon detector surface, which has been demonstrated to increase the optical absorption [43].

In crystal structures, such as silicon, the termination of the crystal lattice (at a surface or interface) results in atoms with unsatisfied bonds. These dangling bonds at the silicon interfaces lead to the formation of surface states, creating mid-bandgap energy levels, as demonstrated in Fig. 2.12. Unlike the continuous bands found in bulk material, electron wavefunctions at the surface are disrupted, resulting in electronic levels within the bandgap. These surface states, or interface states in the presence of another material system like silicon dioxide, play a crucial role in optical absorption processes.

Surface-state absorption becomes particularly significant when dealing with sub-bandgap wavelengths. Chiarotti *et al.* observed that the excess optical loss from a silicon surface peaks at a photon energy of 0.5 eV and diminishes following surface oxidation [43]. This observation underscores the impact of surface states on the optical properties of silicon. Moreover, when the silicon dioxide cladding on silicon waveguides is locally removed, there are photocarriers generated from guided C-band wavelengths [44, 45].

Historically, much effort in silicon processing has been directed towards reducing the concentration of electronically active surface states, as they typically act as recombination centers, lowering the operating efficiency of most devices. However, in nanophotonic

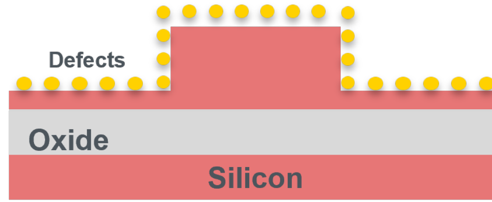

FIGURE 2.12: Cross-sectional view of SSA detectors

devices, where the bulk material volume is reduced, surface chemistry, and consequently surface-state absorption, becomes increasingly important.

By manipulating these surface states through various treatments and structural modifications, it's possible to enhance the photodetection capabilities of silicon photonics devices. This effect was deployed into photodetectors in 2008, where Baehr-Jones *et al.* proposed a photodetector with sensitivity at C-band wavelength by removing the top silicon dioxide cladding and exposing the silicon waveguide to air[44]. Chen *et al.* proposed an all-silicon p-i-n photodetector with a reponsivity of 0.25 mA/W, where they attribute the linear absorption to surface state absorption [46]. An avalanche photodetector from Zhu *et al.* reached a responsivity of 2.33 A / W by enhancing surface state absorption with a reduced waveguide width [47]. A 2 mm long silicon photodetector utilizing surface-state absorption with 0.045 A/W reponsivity was achieved by Ackert *et al.* [45]. It was also demonstrated that surface state concentration can be enhanced by gamma radiation [48] and silver-hyperdoping [49], and the absorption of surface states can be enhanced by raising ambient temperature [50].

2.3.2 Photodiodes

P–N junction

The operation of a p-n junction is a fundamental concept in semiconductor electronics. A p-n junction is formed when p-type and n-type semiconductor materials are joined together. For silicon as a group IV element, the p-type silicon has an abundance of

holes (positive charge carriers), typically created by doping with group III elements like boron. The n-type silicon, on the other hand, has an excess of electrons (negative charge carriers) due to doping with group V elements like phosphorus.

Upon contact, diffusion occurs where electrons from the n-type material move into the p-type material and recombine with holes. This movement creates a depletion region at the junction, characterized by the absence of free charge carriers. The diffusion of charge carriers leads to an imbalance of charge along the junction, creating an electric field and a potential barrier, known as the built-in potential (V_{bi}), described by the equation:

$$V_{bi} = \frac{kT}{q} \ln \left(\frac{N_A N_D}{n_i^2} \right)$$

where k is Boltzmann's constant, T is the temperature, q is the charge of an electron, N_A and N_D are the acceptor and donor doping concentrations, respectively, and n_i is the intrinsic carrier concentration of the semiconductor.

The depletion region is void of free carriers and electrically neutral. Its width (W) can be estimated by:

$$W = \sqrt{\frac{2\varepsilon_s (V_{bi} - V)}{q} \left(\frac{N_A + N_D}{N_A N_D} \right)}$$

where ε_s is the permittivity of the semiconductor material and V is the applied voltage across the junction.

When an external voltage is applied to a p-n junction, it can be in forward bias or reverse bias. At forward bias, applying a positive voltage to the p-side reduces the barrier potential, allowing charge carriers to cross the junction. The current-voltage (I-V) relationship in forward bias is given by the diode equation:

$$I = I_0 \left(e^{\frac{qV}{kT}} - 1 \right)$$

where I_0 is the reverse saturation current and V is the applied bias voltage.

At reverse bias, applying a negative voltage to the p-side increases the barrier potential, widening the depletion region and reducing the flow of charge carriers. The leakage current in reverse bias is small and nearly constant, which approaches I_0 as the reverse bias increases.

A photodiode can be created using a *p-n* junction. When a photon strikes and generates an electron-hole pair, the junction's electric field can separate these charges, thus inhibiting recombination and producing a detectable current. Generation of photo-induced carriers can happen both inside and outside the depletion region. Should this generation take place near but outside the junction, diffusion may allow a carrier to reach the depletion zone and augment the photocurrent. Typically, the generation of an electron-hole pair will enhance the photocurrent if it occurs within a diffusion length from the junction. Conversely, carrier generation within the depletion area tends to be more efficient as recombination is less likely to occur as the drift field separates these charges.

P-I-N photodetector

A p-i-n silicon photodiode consists of a p-type, an intrinsic (undoped), and an n-type Si, with the intrinsic layer situated between the p-type and n-type layers. This configuration extends the depletion region beyond the standard p-n junction diode discussed in the previous section. The intrinsic layer in the p-i-n photodiode is crucial as it serves as a wide depletion region, enabling the absorption and generation of electron-hole pairs by incident photons. The operation of a p-i-n photodiode encompasses two primary processes: photon absorption and charge carrier separation.

When photons with energy exceeding Si's bandgap strike the diode, they generate electron-hole pairs within the intrinsic region. The intrinsic layer's built-in electric field

facilitates the separation of these electron-hole pairs, driving electrons towards the n-type layer and holes towards the p-type layer, thus creating a photocurrent. The generated photocurrent (I_{ph}) in the photodiode under illumination is given by:

$$I_{ph} = q \cdot \Phi \cdot \eta$$

where q is the electron's charge, Φ represents the photon flux, and η denotes the quantum efficiency of the diode.

The total current (I) through the photodiode is described by the modified diode equation:

$$I = I_0 \left(e^{\frac{qV}{kT}} - 1 \right) - I_{ph}$$

Here, I_0 is the reverse saturation current (dark current), V is the applied voltage, k is Boltzmann's constant, and T is the temperature.

The quantum efficiency (QE) denoted by η of a p-i-n photodiode is defined to be [51]:

$$\eta = \frac{\text{number of generated e-h pairs}}{\text{number of incident photons}} = \frac{I_p/q}{P_0/hv} \tag{2.42}$$

The responsivity R describing the photocurrent obtained per unit optical power coupled (in A/W) [51] is defined as:

$$R = \frac{I_p}{P_0} = \frac{\eta q}{hv} = \eta \frac{\lambda_0}{1.24} \tag{2.43}$$

where λ_0 is the photon wavelength (µm). With a quantum efficiency of 100%, the detector could have a maximum responsivity of 1.25 A/W at the wavelength of 1550 nm. The quantum efficiency can be enhanced using avalanche amplification which will be discussed in details in the following section.

Responsivity is a key performance factor of a photodetector. Another important aspect of a photodetector is the bandwidth, which describes how fast the device responds

to a modulated optical signal. Two main factors determining the bandwidth are the transit time and the RC time constant.

Transit time refers to the duration required for carriers (electrons and holes) to travel through the photodetector's active region. In a p-i-n photodetector, the transit time is determined by the width of the intrinsic region, the electric field, and the mobility of the carriers. When biased with high enough electric field, carriers will reach saturation velocity v_{sat}, and the saturation carrier mobility (considering different mobilities for electrons and holes) can be defined as [30]:

$$\mu_{\text{sat}} = \frac{\mu}{\sqrt{1 + \left(\frac{\mu E}{v_{\text{sat}}}\right)^2}}. \tag{2.44}$$

The RC time constant is another significant factor affecting bandwidth. It is the product of the resistance (R) and capacitance (C) of the photodetector circuit. The bandwidth limited by the RC is given by:

$$f_{RC} = \frac{1}{2\pi RC} \tag{2.45}$$

An increase in either resistance or capacitance results in a larger RC time constant, slowing the response of the photodetector. Minimizing the RC time constant is essential for high-speed operation.

The overall bandwidth of the photodetector is therefore given by:

$$\frac{1}{f^2} = \frac{1}{f_{RC}^2} + \frac{1}{f_{transit}^2} \tag{2.46}$$

To maximize bandwidth, both the transit time and the RC time constant must be minimized. For integrated avalanche detectors, the electric field can often exceed the

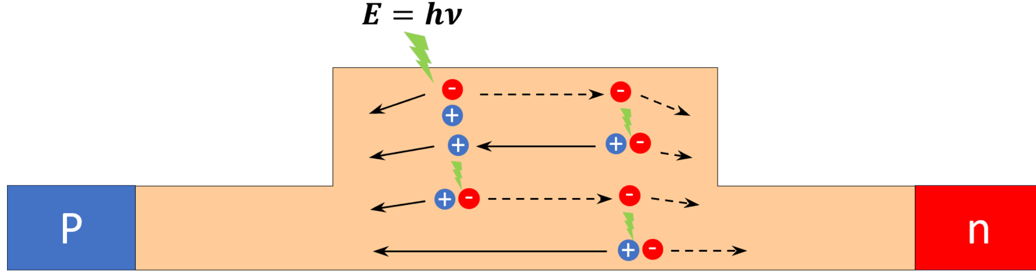

FIGURE 2.13: A conceptual diagram of the avalanche multiplication process.

threshold for saturation carrier velocity. To decrease the RC time constant, one effective method is to reduce the device capacitance by optimizing the device width and length.

2.3.3 Avalanche photodetector

Avalanche breakdown occurs at high reverse bias, where the high electric field provides sufficient kinetic energy and enables impact ionization. As shown in Fig.2.13, multiplication is defined by an optically generated carrier that can generate two additional carriers. When accelerated by the high electric field in the avalanche region, the carriers can gain sufficient kinetic energy to ionize silicon atoms through impact ionization, creating additional electron-hole pairs. These new carriers are also accelerated, leading to a chain reaction, resulting in a significant multiplication of the initial carriers.

Impact ionization is defined by coefficients for both electrons and holes, denoted as α_n and α_p respectively. These coefficients, which are specific to the material, indicate the mean number of ionization events occurring for each unit of distance traversed by a carrier. Specifically, in scenarios where electrons are injected at low frequencies, the multiplication factor M is represented by [52]:

$$M = \frac{\left(1 - \frac{\alpha_p}{\alpha_n}\right) \exp\left[\alpha_n W_D \left(1 - \alpha_p/\alpha_n\right)\right]}{1 - \left(\frac{\alpha_p}{\alpha_n}\right) \exp\left[\alpha_n W_D \left(1 - \alpha_p/\alpha_n\right)\right]}, \tag{2.47}$$

in which W_D symbolizes the depletion width. This formula is crucial in determining the device's breakdown voltage, a point where M tends towards infinity. As a result of the high ionization-coefficient ratio, carrier multiplication can be easily achieved in silicon. In this thesis, we use silicon ridge waveguide integrated avalanche photodetectors to explore the responsivity enhancement from deep-level defects and the slow light effect, which will be discussed in the next few chapters.

2.3.4 Phototransistor

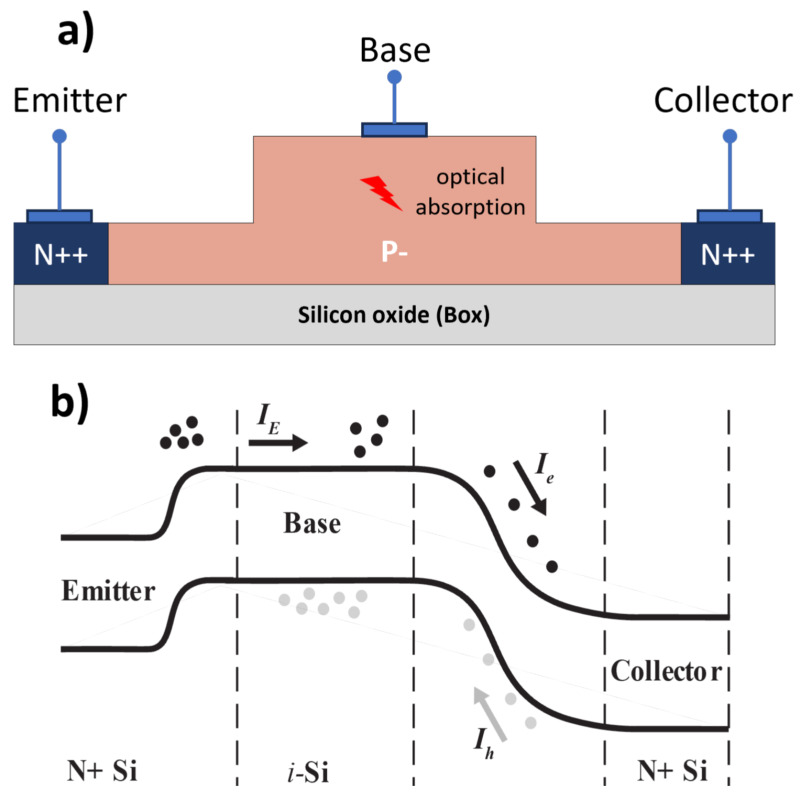

FIGURE 2.14: a) Schematic structure of a conventional SOI phototransistor integrated with a ridge waveguide. b) Energy band diagram under bias.

Another approach to achieve high responsivity photodetection is to use phototransistors. A phototransistor is essentially a light-sensitive transistor, with high gain through

the internal bipolar-transistor action. Compared to avalanche photodiodes, phototransistors eliminate the high voltage required and high noise associated with avalanche multiplication [31]. In a bipolar junction transistor (BJT)-based phototransistor (N-P-N type for example), the device has a collector (N), base (P), and emitter (N) as shown in Fig. 2.14 (a). Photons striking the base region generate electron-hole pairs in the reverse-biased B-C junction. The carriers are then swept out of the space charge region, producing an photocurrent I_L. Holes are drifted into the p-type base, making the base positive withe respect to the emitter. Electrons are injected from the emitter into the base due to the forward-biased B-E junction.

The energy band diagram is depicted in Fig. 2.14 (b). Holes generated by optical absorption in the base-collector depletion zone, and those within the diffusion length, migrate towards the valance band peak and get captured in the base. This congregation of holes or positive charges causes a reduction in the base energy (effectively increasing the potential), facilitating a substantial electron flow from the emitter to the collector. The phenomenon of a significantly amplified electron current triggered by a minimal hole current is attributed to the efficiency of emitter injection. This principle is a key amplification mechanism for phototransistors, especially when the electron transit time across the base is considerably shorter than the minority-carrier lifetime [31].

Despite the high gain, phototransistors are not commonly found in major optical optical communication systems. The bandwidth of the phototransistor is limited by the large B-C junction capacitance, which is then multiplied by the Miller effect [53]. Therefore, phototransistors with high gain can be used for non-high-speed applications such as power monitoring and light detection and ranging (LIDAR) systems.

2.4 Erbium doped waveguide amplifiers

Optical amplifiers are pivotal for the realization of complicated functionalities as photonics integrated circuits scale up. These devices amplify optical signals directly to compensate the various losses, bringing more flexibility to power budget management. Besides, an effective gain medium is the key for the development of on-chip lasers, which has been an urgent issue for monolithically integrated silicon PICs. This sections focuses on erbium-doped waveguide amplifiers (EDWAs) for silicon photonic integrated circuits, covering their operation, material system, and integration.

2.4.1 Erbium luminescence

Erbium, as a rare-earth element, situated in the sixth row of the periodic table, has an electronic configuration of $[Xe]4f^{12}6s^2$. Similar to other elements in the rare-earth series, erbium demonstrates several strong and notably narrow luminescence bands across the visible and near-infrared spectrum. As an ion, erbium predominantly exists in two states of oxidation: Er^{2+} and Er^{3+}, with the former being relatively uncommon in semiconductor materials. The Er^{3+} ion is created through the loss of an electron from the 4f shell and both electrons from the 6s shell. This triply charged state of the ion is of significant interest in the field of photonics due to its radiative transitions near 1.53 μm in the near-infrared region, which coincide with the conventional telecommunication band. In this state, the 5s and 5p shells provide shielding to the incomplete 4f shell, leading to the ion's luminescence being largely independent of its host. The radiative transitions of erbium in solid hosts are similar to those observed in the free ion, albeit with slight variations due to Stark splitting [54], and the interaction between electrons and phonons is minimal.

The energy level diagram of Er is shown in Figure 2.15, where the electron transitions

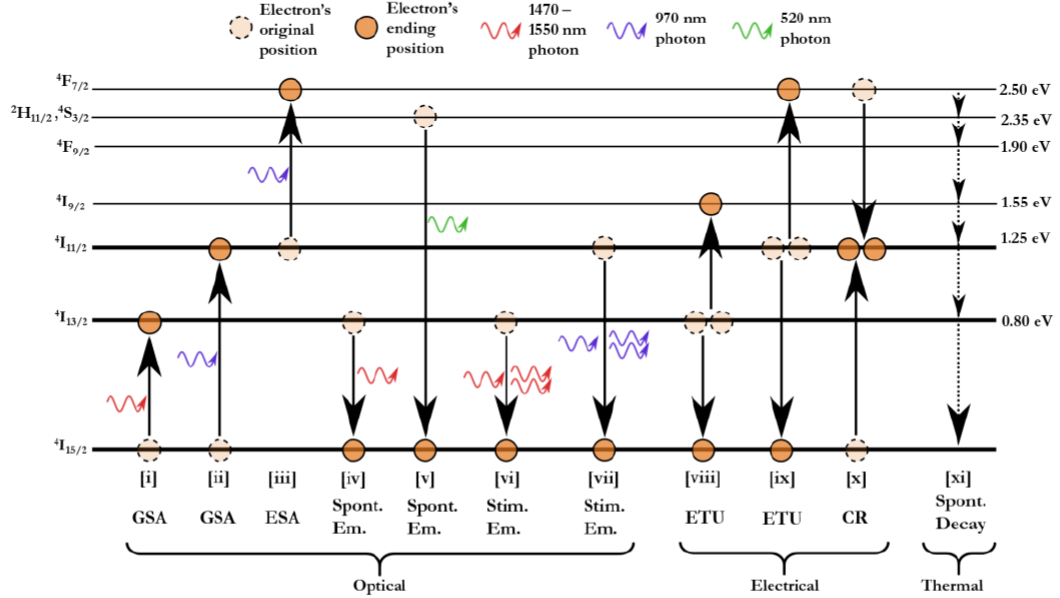

FIGURE 2.15: Energy level diagram of Er^{3+} ions[55].

between different energy levels can be divided into optical, electrical, and thermally-based processes[55]. The ground state with a configuration of ^{4}I is split into 9/2, 11/2, 13/2, and 15/2 due to the integration between the electron's spin and orbital angular momentum [56]. The stimulated emission corresponding to a transition between the first excited state ($^4I_{13/2}$) and the ground state is at around 1530 nm, corresponding to an energy difference of around 0.8 eV. The lifetime of the first excited state is relatively longer compared to other states, but can be reduced in the presence of non-radiative processes.

Figure 2.16 demonstrates the three optical processes that can occur in a system with an excited and ground energy state, of optical absorption, spontaneous emission, and stimulated emission.

Optical absorption occurs when an erbium ion in a lower energy state absorbs a photon and transitions to a higher energy state. In erbium-doped fiber amplifiers (EDFAs), Er^{3+} ions absorb photons typically around 1.48 µm or 0.98 µm, exciting them from their

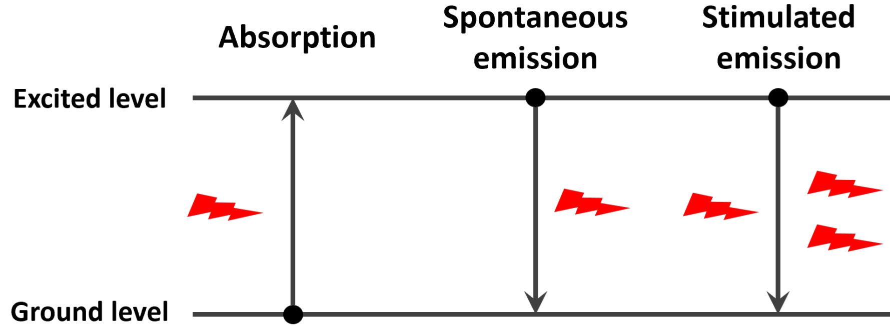

FIGURE 2.16: Optical processes: optical absorption, spontaneous emission, and stimulated emission.

ground state ($^4I_{15/2}$) to higher energy states. This excitation is crucial for preparing the ions for subsequent photon emission, key for signal amplification in optical communications. Stimulated emission occurs when an excited Er^{3+} ion encounters a photon with energy matching the energy difference between its current and a lower energy state. This interaction triggers the ion to release a second photon, identical to the incident photon. This primarily occurs when Er^{3+} ions transition from the $^4I_{13/2}$ state back to the ground state, emitting a photon at approximately 1.53 µm. Spontaneous emission occurs when an excited erbium ion independently returns to a lower energy state, emitting a photon randomly. This process is the primary noise source in Er-doped optical amplifiers.

The emission efficiency and lifetime of Er ions are significantly impacted by interactions among ions, particularly through the quenching effect that arises at high concentrations of erbium. Coulombic interactions between neighboring ions can effectively transfer excitation from an ion in an excited state to another in the ground state, a process known as energy migration. Interactions can occur between two excited ions, resulting in one ion transitioning to the ground state and the other to a higher-energy state, known as co-operative up-conversion. Furthermore, an ion in a higher excited state can transfer energy to another ion, elevating it from the ground state to the first excited state, a process termed as cross-relaxation.

2.4.2 Amplification in erbium-based systems

The gain of erbium-based systems depends on various device parameters, including erbium ion concentration, amplifier length, waveguide structure, and pump power [57–59].

A two-level model can be used to describe the three optical processes mentioned in the previous section. The population densities of the ground state N_1 and the excited state N_2 are given by the following rate equations [60]:

$$\frac{\partial N_2}{\partial t} = (\sigma_p^a N_1 - \sigma_p^e N_2)\phi_p + (\sigma_s^a N_1 - \sigma_s^e N_2)\phi_s - \frac{N_2}{T_1} \tag{2.48}$$

$$\frac{\partial N_1}{\partial t} = (\sigma_p^e N_2 - \sigma_p^a N_1)\phi_p + (\sigma_s^e N_2 - \sigma_s^a N_1)\phi_s + \frac{N_2}{T_1} \tag{2.49}$$

where σ^a and σ^e are the absorption and emission cross sections at the frequency ω_j with $j = p, s$ for pump and signal light. T_1 is the spontaneous lifetime of the excited state. The quantities ϕ_p and ϕ_s represent the photon flux for the pump and signal waves, governed by:

$$\phi_p = P_p/(a_p h\nu_p) \tag{2.50}$$

$$\phi_s = P_s/(a_s h\nu_s) \tag{2.51}$$

where P_j is the optical power and a_j is the cross section area for $j = p, s$ respectively.

Because of the contribution from absorption, stimulated emission, and spontaneous emission, the pump power and signal power intensity would vary along the propagation direction. For simplicity, we can neglect the spontaneous emission and fiber losses for

an amplifier [58, 60]. The pump and signal power are then given by:

$$\frac{\partial P_s}{\partial z} = \Gamma_s(\sigma_s^e N_2 - \sigma_s^a N_1)P_s \tag{2.52}$$

$$\frac{\partial P_p}{\partial z} = \Gamma_p(\sigma_p^e N_2 - \sigma_p^a N_1)P_p \tag{2.53}$$

where Γ_s and Γ_p are the confinement factors describing the power confined within the active gain area. Equation 2.48 can be solved by setting the time derivative to 0 [60]:

$$N_2(z) = -\frac{T_1}{a_d h\nu_s}\frac{\partial P_s}{\partial z} - \frac{T_1}{a_d h\nu_p}\frac{\partial P_p}{\partial z} \tag{2.54}$$

where a_d is the overlapping area between the active region and the propagating mode. The total amplifier gain G for an EDWA of length L is obtained by plugging in Eq. (2.54) into Eqs. (2.52 & 2.53) and integrating over the amplifier length:

$$G = \Gamma_s \exp\left[\int_0^L (\sigma_s^e N_2 - \sigma_s^a N_1)dz\right] \tag{2.55}$$

Further details will be discussed in Chapter 6 for the experimental results.

2.4.3 Erbium implantation in tellurium oxide

There are different ways of incorporating erbium ions into EDWAs, including molecular beam epitaxy, sputtering, thermal diffusion, chemical vapour deposition, and ion implantation. Ion implantation of erbium offers precise doping control of dopant location and concentration. It is also effective for co-doping, notably with ytterbium (Yb) to enhance Er^{3+} emission and reduce upconversion losses [61]. In addition, ion implantation of Er ions can lead to better electrical activation and more optically active erbium ions compared to other techniques [56]. Implantation of erbium ions directly into the silicon waveguide suffers from the damage introduced to the silicon matrix. High-temperature annealing can repair most of the damage caused in the fabrication process, but it has

the downside of creating clusters of rare-earth ions or forming optically inactive silicides [62]. Besides, low solubility of erbium in crystalline silicon has been a limiting factor for the development of silicon EDWAs. Ion implantation directly into Si_3N_4 waveguides has been demonstrated recently [63], but with added complexity in the fabrication process.

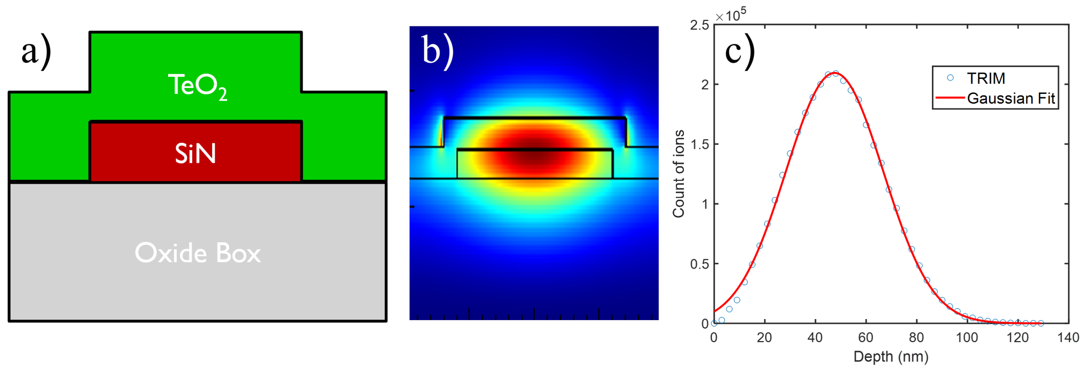

FIGURE 2.17: a) Schematic cross-sectional view of the cross section view of the Si_3N_4 waveguide cladded with TeO_2 glass with a thickness of 100 nm, b) optical mode profile of the propagating light at 1550 nm, and c) simulated ion implantation ion as a function of implantation depth based on an energy of 200 KeV.

TeO_2 is considered as a promising host for erbium ions due to its high refractive index (around 2.1), high rare earth solubility, high transparency at the near infrared wavelength with low propagation loss, and good thermal and mechanical stability.

Figure 2.17 (a) and (b) show the structure cross section of a Si_3N_4 waveguide cladded with TeO_2 thin film, and the corresponding mode simulation at 1550 nm. When excited with a 1470 nm pump light, the evanescent field of the pump light interacts with the erbium-implanted TeO_2 cladding. This interaction prompts the emission of light at approximately 1530 nm from Er^{3+} ions, which matches the signal wavelength. Fig 2.17 (c) shows the ion distribution along the TeO_2 depth simulated from transport of ions in matter (TRIM), where the peak of the erbium concentration overlaps with the propagating mode. The emitted light coherently propagates alongside the signal, thereby amplifying its power.

In this thesis, we focus on erbium implantation into tellurium oxide (TeO_2) as cladding material for the development of EDWAs, with more details discussed in Chapter 6.

2.5 References

[1] A. Shacham, K. Bergman, and L. P. Carloni, Photonic networks-on-chip for future generations of chip multiprocessors, *IEEE Transactions on Computers*, vol. 57(9), 1246–1260, 2008.

[2] D. B. Bonneville, M. Albert, R. Arbi, M. Munir, B. L. S. Frare, K. K. M. Kiani, H. C. Frankis, A. P. Knights, A. Turak, K. N. Sask, *et al.*, Hybrid silicon-tellurium-dioxide dbr resonators coated in pmma for biological sensing, *Biomedical Optics Express*, vol. 14(4), 1545–1561, 2023.

[3] X. Tu, J. Song, T.-Y. Liow, M. K. Park, J. Q. Yiying, J. S. Kee, M. Yu, and G.-Q. Lo, Thermal independent silicon-nitride slot waveguide biosensor with high sensitivity, *Optics Express*, vol. 20(3), 2640–2648, 2012.

[4] X. Zhang, K. Kwon, J. Henriksson, J. Luo, and M. C. Wu, A large-scale micro electro mechanical-systems-based silicon photonics lidar, *Nature*, vol. 603(7900), 253–258, 2022.

[5] J. Bao, Z. Fu, T. Pramanik, J. Mao, Y. Chi, Y. Cao, C. Zhai, Y. Mao, T. Dai, X. Chen, *et al.*, Very-large-scale integrated quantum graph photonics, *Nature Photonics*, vol. 17(7), 573–581, 2023.

[6] X. Yan, W. Asavanant, H. Kamakari, J. Wu, J. F. Young, and R. Raussendorf, A quantum computer architecture based on silicon donor qubits coupled by photons, *Advanced Quantum Technologies*, vol. 2000011, 2 000 011, 2020, issn: 2511-9044.

[7] J. Sun, E. Timurdogan, A. Yaacobi, E. S. Hosseini, and M. R. Watts, Large-scale nanophotonic phased array, *Nature*, vol. 493(7431), 195–199, 2013.

[8] A. Liu, R. Jones, L. Liao, D. Samara-Rubio, D. Rubin, O. Cohen, R. Nicolaescu, and M. Paniccia, A high-speed silicon optical modulator based on a metal-oxide-semiconductor capacitor, *Nature*, vol. 427(6975), 615–618, 2004, ISSN: 00280836.

[9] Z. Wang, D. Paez, A. I. Abd El-Rahman, P. Wang, L. Dow, J. C. Cartledge, and A. P. Knights, Resonance control of a silicon micro-ring resonator modulator under high-speed operation using the intrinsic defect-mediated photocurrent, *Optics Express*, vol. 25(20), 24 827–24 836, 2017.

[10] D. Nikolova, S. Rumley, D. Calhoun, Q. Li, R. Hendry, P. Samadi, and K. Bergman, Scaling silicon photonic switch fabrics for data center interconnection networks, *Optics Express*, vol. 23(2), 1159–1175, 2015.

[11] H. Jayatilleka, H. Shoman, L. Chrostowski, and S. Shekhar, Photoconductive heaters enable control of large-scale silicon photonic ring resonator circuits, *Optica*, vol. 6(1), 84, 2019, ISSN: 2334-2536.

[12] C. T. DeRose, D. C. Trotter, W. A. Zortman, A. L. Starbuck, M. Fisher, M. R. Watts, and P. S. Davids, Ultra compact 45 ghz cmos compatible germanium waveguide photodiode with low dark current, *Optics Express*, vol. 19(25), 24 897–24 904, 2011.

[13] J. J. Ackert, High-speed silicon detector structures for photonic integrated circuits, Ph.D. dissertation, McMaster University, 2015, 156.

[14] R. Anthony, D. E. Hagan, D. Genuth-Okon, L. Martinez Maestro, I. F. Crowe, M. P. Halsall, and A. P. Knights, Extended wavelength responsivity of a germanium photodetector integrated with a silicon waveguide exploiting the indirect transition, *IEEE Journal of Selected Topics in Quantum Electronics*, vol. 26(2), 1–7, 2020, ISSN: 21910359.

[15] Y. Gao, F. Guo, R. Das, P. Mascher, and A. P. Knights, High responsivity si/ge phototransistor on silicon photonics platform for small signal application, in *2023 Photonics North (PN)*, IEEE, 2023, 1–1.

[16] K. K. Miarabbas, H. C. Frankis, A. P. Knights, and J. D. B. Bradley, Silicon-thulium hybrid microdisk lasers with low threshold and wide emission wavelength range, *Optics Express*, vol. 31(12), 20 244–20 255, 2023.

[17] C. Xiang, J. Guo, W. Jin, L. Wu, J. Peters, W. Xie, L. Chang, B. Shen, H. Wang, Q.-F. Yang, *et al.*, High-performance lasers for fully integrated silicon nitride photonics, *Nature communications*, vol. 12(1), 6650, 2021.

[18] Y. Zhang, S. Yang, A. E.-J. Lim, G.-Q. Lo, C. Galland, T. Baehr-Jones, and M. Hochberg, A compact and low loss y-junction for submicron silicon waveguide, *Optics Express*, vol. 21(1), 1310–1316, 2013.

[19] Z. Lu, H. Yun, Y. Wang, Z. Chen, F. Zhang, N. A. F. Jaeger, and L. Chrostowski, Broadband silicon photonic directional coupler using asymmetric-waveguide based phase control, *Optics Express*, vol. 23(3), 3795, 2015, ISSN: 1094-4087.

[20] W. Bogaerts, P. Dumon, D. Van Thourhout, and R. Baets, Low-loss, low-cross-talk crossings for silicon-on-insulator nanophotonic waveguides, *Optics letters*, vol. 32(19), 2801–2803, 2007.

[21] D.-X. Xu, J. H. Schmid, G. T. Reed, G. Z. Mashanovich, D. J. Thomson, M. Nedeljkovic, X. Chen, D. Van Thourhout, S. Keyvaninia, and S. K. Selvaraja, Silicon photonic integration platform–have we found the sweet spot? *IEEE Journal of Selected Topics in Quantum Electronics*, vol. 20(4), 189–205, 2014.

[22] D. Taillaert, H. Chong, P. I. Borel, L. H. Frandsen, R. M. De La Rue, and R. Baets, A compact two-dimensional grating coupler used as a polarization splitter, *IEEE Photonics Technology Letters*, vol. 15(9), 1249–1251, 2003.

[23] G. Lifante, *Integrated photonics: fundamentals.* John Wiley & Sons, 2003.

[24] B. E. Saleh and M. C. Teich, *Fundamentals of photonics*. John Wiley & Sons, 2019.

[25] I. Ansys, *Mode solutions – waveguide mode solver and propagation simulator*, `https://www.ansys.com/products/optics/mode`, Accessed: 2023/11/06, 2024.

[26] P. Cheben, R. Halir, J. H. Schmid, H. A. Atwater, and D. R. Smith, Subwavelength integrated photonics, *Nature*, vol. 560(7720), 565–572, 2018, ISSN: 14764687.

[27] S. Rytov, Electromagnetic properties of a finely stratified medium, *Soviet Physics JEPT*, vol. 2, 466–475, 1956.

[28] P. Lalanne, S. Astilean, P. Chavel, E. Cambril, and H. Launois, Design and fabrication of blazed binary diffractive elements with sampling periods smaller than the structural cutoff, *JOSA A*, vol. 16(5), 1143–1156, 1999.

[29] P. Jean, A. Gervais, S. LaRochelle, and W. Shi, Slow light in subwavelength grating waveguides, *IEEE Journal of Selected Topics in Quantum Electronics*, vol. 26(2), 2020, ISSN: 15584542.

[30] L. Chrostowski, Z. Lu, J. Flueckiger, X. Wang, J. Klein, A. Liu, J. Jhoja, and J. Pond, Design and simulation of silicon photonic schematics and layouts, *Silicon Photonics and Photonic Integrated Circuits V*, vol. 9891, 989 114, 2016, ISSN: 1996756X.

[31] S. Sze, *Semiconductor Devices: Physics and Technology* (Bibliyografya ve İndeks). Wiley, 1985, ISBN: 9780471874249.

[32] M. Casalino, G. Coppola, R. M. De La Rue, and D. F. Logan, State-of-the-art all-silicon sub-bandgap photodetectors at telecom and datacom wavelengths, *Laser and Photonics Reviews*, vol. 10(6), 895–921, 2016, ISSN: 18638899.

[33] H. Garcia and R. Kalyanaraman, Phonon-assisted two-photon absorption in the presence of a dc-field: The nonlinear franz–keldysh effect in indirect gap semiconductors, *Journal of Physics B: Atomic, Molecular and Optical Physics*, vol. 39(12), 2737, 2006.

[34] A. P. Knights, J. D. B. Bradley, S. H. Gou, and P. E. Jessop, Silicon-on-insulator waveguide photodetector with self-ion-implantation-engineered-enhanced infrared response, *Journal of Vacuum Science & Technology A: Vacuum, Surfaces, and Films*, vol. 24(3), 783–786, 2006, ISSN: 0734-2101.

[35] D. F. Logan, P. E. Jessop, A. P. Knights, R. M. Gwilliam, and M. P. Halsall, The effect of doping type and concentration on optical absorption via implantation induced defects in silicon-on-insulator waveguides, *Conference on Optoelectronic and Microelectronic Materials and Devices, Proceedings, COMMAD*, (1), 152–155, 2008.

[36] D. F. Logan, P. Velha, M. Sorel, R. M. De La Rue, A. P. Knights, and P. E. Jessop, Defect-enhanced silicon-on-insulator waveguide resonant photodetector with high sensitivity at 1.55 μm, *IEEE Photonics Technology Letters*, vol. 22(20), 1530–1532, 2010.

[37] J. J. Ackert, A. S. Karar, D. J. Paez, P. E. Jessop, J. C. Cartledge, and A. P. Knights, 10 gbps silicon waveguide-integrated infrared avalanche photodiode, *Optics Express*, vol. 21(17), 19 530, 2013, ISSN: 1094-4087.

[38] J. J. Ackert, D. J. Thomson, L. Shen, A. C. Peacock, P. E. Jessop, G. T. Reed, G. Z. Mashanovich, and A. P. Knights, High-speed detection at two micrometres with monolithic silicon photodiodes, *Nature Photonics*, vol. 9(6), 393–396, 2015, ISSN: 17494893.

[39] D. F. Logan, P. E. Jessop, and A. P. Knights, Modeling defect enhanced detection at 1550 nm in integrated silicon waveguide photodetectors, *Journal of Lightwave Technology*, vol. 27(7), 930–937, 2009, ISSN: 07338724.

[40] P. Foster, J. Doylend, P. Mascher, A. Knights, and P. Coleman, Optical attenuation in defect-engineered silicon rib waveguides, *Journal of applied physics*, vol. 99(7), 2006.

[41] F. Vook and H. Stein, Relation of neutron to ion damage annealing in si and ge, *Radiation Effects*, vol. 2(1), 23–30, 1969.

[42] M. W. Geis, S. J. Spector, M. E. Grein, J. U. Yoon, D. M. Lennon, and T. M. Lyszczarz, Silicon waveguide infrared photodiodes with >35 GHz bandwidth and phototransistors with 50 AW-1 response, *Optics Express*, vol. 17(7), 5193, 2009, ISSN: 10944087.

[43] G. Chiarotti, S. Nannarone, R. Pastore, and P. Chiaradia, Optical absorption of surface states in ultrahigh vacuum cleaved (111) surfaces of ge and si, *Physical review B*, vol. 4(10), 3398, 1971.

[44] T. Baehr-Jones, M. Hochberg, and A. Scherer, Photodetection in silicon beyond the band edge with surface states, *Optics Express*, vol. 16(3), 1659, 2008, ISSN: 1094-4087.

[45] J. J. Ackert, A. S. Karar, J. C. Cartledge, P. E. Jessop, and A. P. Knights, Monolithic silicon waveguide photodiode utilizing surface-state absorption and operating at 10 gb/s, *Optics Express*, vol. 22(9), 10 710, 2014, ISSN: 10944087.

[46] H. Chen, X. Luo, and A. W. Poon, Cavity-enhanced photocurrent generation by 1.55 μm wavelengths linear absorption in a p-i-n diode embedded silicon microring resonator, *Applied Physics Letters*, vol. 95(17), 2009, ISSN: 00036951.

[47] H. Zhu, L. Zhou, Y. Zhou, Q. Wu, X. Li, and J. Chen, All-silicon waveguide avalanche photodetectors with ultrahigh gain-bandwidth product and low breakdown voltage, *IEEE Journal of Selected Topics in Quantum Electronics*, vol. 20(6), 226–231, 2014, ISSN: 15584542.

[48] N. Boynton, M. Gehl, C. Dallo, A. Pomerene, A. Starbuck, D. Hood, P. Dodd, S. Swanson, D. Trotter, C. DeRose, and A. Lentine, Gamma radiation effects on passive silicon photonic waveguides using phase sensitive methods, *Optics Express*, vol. 28(23), 35 192, 2020, ISSN: 10944087.

[49] X. Qiu, Z. Wang, X. Hou, X. Yu, and D. Yang, Visible-blind short-wavelength infrared photodetector with high responsivity based on hyperdoped silicon, *Photonics Research*, vol. 7(3), 351, 2019, ISSN: 23279125.

[50] Z. Zhang, Z. Wang, K. Zou, T. Yang, and X. Hu, Temperature-dependent characteristics of infrared photodetectors based on surface-state absorption in silicon, *Applied Optics*, vol. 60(30), 9347, 2021, ISSN: 1559-128X.

[51] J. M. Senior and M. Y. Jamro, *Optical fiber communications: principles and practice*. Pearson Education, 2009.

[52] S. M. Sze, Y. Li, and K. K. Ng, *Physics of semiconductor devices*. John Wiley & Sons, 2021.

[53] D. Neamen, *Semiconductor physics and devices*. McGraw-Hill, Inc., 2002.

[54] H. Steinkemper, S. Fischer, M. Hermle, and J. Goldschmidt, Stark level analysis of the spectral line shape of electronic transitions in rare earth ions embedded in host crystals, *New Journal of Physics*, vol. 15(5), 053 033, 2013.

[55] H. C. Frankis, Low-loss TeO_2 devices on Si and Si_3N_4 photonic circuits, Ph.D. dissertation, McMaster University, 2021.

[56] A. Kenyon, Erbium in silicon, *Semiconductor Science and Technology*, vol. 20(12), R65, 2005.

[57] C. R. Giles and E. Desurvire, Modeling erbium-doped fiber amplifiers, *Journal of lightwave technology*, vol. 9(2), 271–283, 1991.

[58] A. Saleh, R. Jopson, J. Evankow, and J. Aspell, Modeling of gain in erbium-doped fiber amplifiers, *IEEE Photonics Technology Letters*, vol. 2(10), 714–717, 1990.

[59] H. C. Frankis, H. M. Mbonde, D. B. Bonneville, C. Zhang, R. Mateman, A. Leinse, and J. D. B. Bradley, Erbium-doped TeO_2-coated Si_3N_4 waveguide amplifiers with 5 dB net gain, *Photonics Research*, vol. 8(2), 127–134, 2020.

[60] P. M. Becker, A. A. Olsson, and J. R. Simpson, *Erbium-doped fiber amplifiers: fundamentals and technology.* Elsevier, 1999.

[61] G. Dearnaley, Ion implantation, *Nature*, vol. 256(5520), 701–705, 1975.

[62] A. Polman, Erbium implanted thin film photonic materials, *Journal of Applied Physics*, vol. 82(1), 1–39, 1997, ISSN: 00218979.

[63] Y. Liu, Z. Qiu, X. Ji, A. Lukashchuk, J. He, J. Riemensberger, M. Hafermann, R. N. Wang, J. Liu, C. Ronning, *et al.*, A photonic integrated circuit–based erbium-doped amplifier, *Science*, vol. 376(6599), 1309–1313, 2022.

Chapter 3

Si/Ge Phototransistor with Responsivity over 1000A/W on a Silicon Photonics Platform

Reprinted in part with open access permissions from: Yuxuan Gao, Ranjan Das, Yanran Xie, Feng Guo, Peter Mascher, and Andrew P. Knights. Si/Ge Phototransistor with Responsivity 1000A/W on a Silicon Photonics Platform. *Optics Express*, *32*(2), 2271-2280, 2024.

https://doi.org/10.1364/OE.512228

This chapter includes the findings presented in a published manuscript on the design, simulation, and characterization of a Si/Ge phototransistor with enhanced responsivity through electric field engineering. Compared to conventional n-p-n or p-n-p phototransistors, two p+ doped regions are intentionally introduced under the Ge epitaxy, in the slightly p doped silicon region. As a result, the device bandgap structure is altered, with the energy levels in the p+ doped regions raised, resulting in a higher internal gain which is discussed in details in section 3.1. The device achieved a high responsivity of

over 1000 A/W from direct fabrication through a standard silicon photonics fabrication technology, making it promising for high volume integration with large scale photonic integrated circuits for various applications.

3.1 Abstract

We report a Si/Ge waveguide phototransistor with high responsivity and low dark current under low bias voltages, due to an engineered electric field distribution. The photodetector consists of n-i-p-i-n doping regions and shows a responsivity of 606 A/W at 1 V bias, and 1032 A/W at 2.8V bias with an input optical power of -50 dBm, and dark current of 4 µA and 42 µA respectively. This is achieved by placing two p^+-doped regions in the silicon slab region beneath the Ge epitaxial layer. A measured small signal -3 dB bandwidth of 1.5 GHz with a -80 dBc/Hz phase noise response at 1 KHz frequency offset were demonstrated experimentally.

3.2 Introduction

Leveraged by the proliferation of complementary metal-oxide semiconductor (CMOS) technologies, silicon photonics has gained a significant position in the field of optical communication[1], optical computing[2], quantum computing[3], optical beam forming[4], and bio-sensing[5].

A critical function in any silicon photonic circuit is photodetection, particularly when integrated with internal amplification, to address the need to work within a limited link budget. There have been several reports of amplified detection including Si/Ge avalanche photodetectors (APDs) [6–9] and all-silicon APDs[10–12]. Si/Ge photodetectors are disadvantaged by a relatively large leakage current, attributable to the lattice mismatch at the Si/Ge interface[13, 14]. Conversely, all-silicon photodetectors suffer from relatively

low responsivity due to silicon's low optical absorption coefficient at 1550 nm even with sensitization via deep levels [11, 15, 16].

A phototransistor operates as a photosensitive transistor, effectively combining the properties of both a photodiode and a bipolar junction transistor (BJT). The conductivity of a phototransistor is modulated by the base current, which originates from the electron-hole pairs generated from the active area upon optical excitation. Phototransistors achieve high responsivity due to internal photocurrent gain, eliminating the need for low input impedance between the phototransistor and external amplifiers, leading to a simplification of the overall circuitry[17]. The impedance of phototransistors can be tuned to adjust the gain and diminish device noise, making them ideal for monitoring optical signals across a large dynamic range of intensities. Moreover, such a high-responsivity phototransistor eliminates the transimpedence amplifier (TIA) element from the subsequent circuit chain, which leads to reduced system design complexity and an improved system power budget[18]. In some applications, proposed high-gain phototransistors can be directly terminated using a broadband passive impedance matching network, diminishing the need for implementing successive TIAs and limiting amplifier (LA) circuit blocks.

In addition to responsivity, low phase noise is a desirable feature in numerous applications, including LIDAR[19], high-quality RF or microwave signal generation[20], frequency comb generation[21] and photonics based quantum applications[22]. Low phase noise and a clean RF spectrum without any harmonic distortion are crucial design parameters for precise range and speed detection [23–26]. Also, excess phase noise from photodetectors overloads the successive signal processing units, additional high-quality factor (high-Q) photonic filtering, and constrain the TIA design specifications [10, 11]. Similarly, phase noise in photodetectors is a major bottleneck in RF-photonics, time

and frequency metrology, and photonic low-phase noise microwave generation or in frequency converter systems [12, 13]. Achieving both high responsivity and low detector phase noise performances concurrently is challenging.

Ultra-high responsivity ranging from 10^5 to 10^7 A/W has been demonstrated for phototransistors with different material systems including hybrid graphene-perovskite [14], InGaAs [3], and inorganic/organic hybrid materials [15]. However, there has been very limited work on phototransistors on a silicon photonics platform. Responsivities of 42 A/W at 1V [16], 14 A/W at 1.5 V [17], and 53 A/W at 1 V [18] have been achieved for waveguide integrated phototransistors using a commercial silicon foundry.

Here we demonstrate a Si/Ge phototransistor that operates at the conventional optical band centred at 1550 nm, with high responsivity, low dark current and low phase noise. The devices are fabricated using a standard silicon photonics fabrication technology without modification or post processing. The key innovation compared to previous work is the introduction of floating p^+-doped regions beneath the photosensitive germanium, allowing the passive manipulation of the electric field, with concomitant suppression of dark current generated at the Ge-Si interface[27].

This chapter is organized as follows. Section 3.3 describes the device design and fabrication followed by experimental characterization in Section 3.4. It also explains the effect of the p^+-doped regions in terms of responsivity and dark current performance. Finally, a conclusion and outlook is provided in Section 3.5.

3.3 Method

3.3.1 Operational principle

The device is a waveguide integrated phototransistor designed with an n-p-n configuration with two floating p^+-doped regions beneath the germanium epitaxial layer as shown

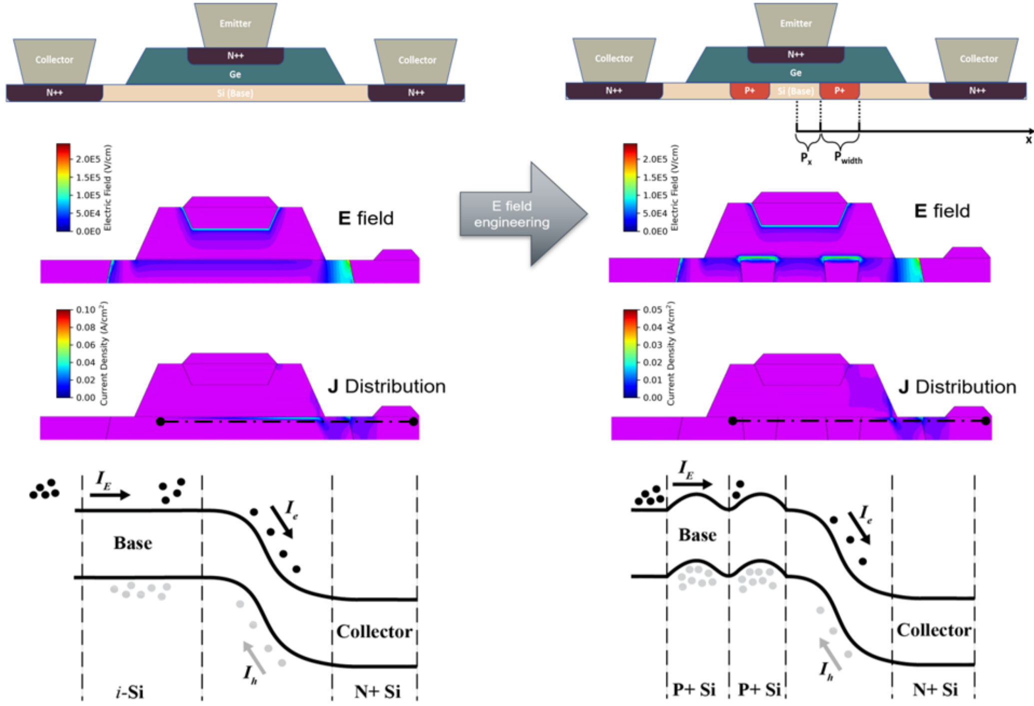

FIGURE 3.1: Cross-sectional diagram of the n-p-n structure of the Si/Ge photodetector with electric field and current density (J) simulation of the photodetector at a forward bias of 2 V_{ce}. Voltage is applied on the emitter and the right side collector only in the simulation. Bottom shows the band diagrams of the devices with a cutline at the Si/Ge interface demonstrated in the current density plots. Left, without p^+-doping; right, with p^+-doping.

in Fig. 3.1. P_x and P_{width} denote the distance from the device center to the inner edge of the p^+-doped regions and the width of the p^+-doped regions. The low-doped i region, the n^{++} region within the Ge, and the n^{++} region within the Si act as the base (B), emitter (E), and collector (C) of the phototransistor, respectively. The emitter is heavily doped to supply ample carriers during device operation.

Unlike previously reported waveguide Si-Ge phototransistors [28], the two p^+-doped regions distributed under the Ge facilitate an increased gain while suppressing the leakage current of the n-p-n structured phototransistor by re-configuring the electric field

distribution. The structure is simulated with technology computer aided design (TCAD) from Silvaco, with electric field and current density shown in Fig. 3.1 for a forward V_{ce} of 2V.

The B-E potential barrier's height is governed by the doping levels of the adjacent regions. With the p^+-doped regions under Ge, the potential barrier at the B-E junction increases as demonstrated in the schematic band diagram (derived from horizontal cutlines at the Si/Ge interface) in Fig .3.1, which effectively restricts the flow of dark current through the base region. The increased potential barrier would force the dark current to follow an alternate route that bypasses the Si/Ge interface as shown in the current density plot (right) in Fig.3.1, where the dark current is typically originated due to the Ge/Si lattice mismatch [27] as shown in the current density plot (left), thus significantly reducing the dark current. Importantly, this suppression is achieved without significantly impacting the photocurrent pathway, which is more vertical in nature.

When biased in the active regime, with near infrared light (at 1550 nm) coupling, photo-generated holes in the Ge layer are swept into the base region within the diffusion length, while electrons move toward the collector. The accumulation of holes in the base lowers the B-E energy barrier [29]. Electrons are subsequently injected from the emitter into the base region, contributing to the amplification of the photocurrent. The floating p^+-doped regions would elevate the potential barrier in the valance band at the base, which increases the base's capacity to accumulate holes, further raising the potential and amplifying the photocurrent. This interplay between the structural elements and carrier dynamics is crucial for the observed improvement in photocurrent. The internal gain of the photo response and the dark current, determined by the base current (photo-generated carriers), can be adjusted by modulating the intensity of the injected light.

3.3.2 Device fabrication

Device fabrication was carried out at the Advanced Micro Foundry (AMF) using 193 nm ultraviolet lithography multi-project wafer (MPW) process, facilitated by CMC Singapore Microsystems of Canada. Silicon-on-insulator (SOI) <100> wafers with a silicon thickness of 220 nm were etched to form rib waveguides with a nominal width of 10 µm and a length of 200 µm on top of 2 µm of buried oxide. A silicon taper of 100 µm length was used to couple light from the routing strip waveguide with a width of 500 nm to the rib waveguide of 10 µm width. The doping regions in the silicon layer were formed by the implantation of boron (p-type) and phosphorus (n-type) in the 220 nm thick waveguide region. The i-region in the silicon (base region) is in fact slightly p-doped to a level of $\sim 5-10\times10^{15}cm^{-3}$ and the floating p^{+}-doped regions to a level of $\sim 1\times10^{19}cm^{-3}$. The width and location of the p^{+}-doped regions (P_{width} and P_x) varied from 0.75 µm to 1.5 µm, and from 0.5 µm to 1 µm, respectively, to investigate the impact of p^{+}-doped regions on the device performance. With the total device length and the width of the collector fixed, the distance between the edge of the p^{+}-doped region and the edge of the n^{++} region varied from 0 µm to 1.25 µm. The collectors are doped to a level of $\sim 5-10\times10^{20}cm^{-3}$. A layer of germanium was deposited on top of silicon by selective epitaxial growth with a shallow n^{++} doped layer ($\sim 5-10\times10^{19}cm^{-3}$) at its top for emitter contact.

3.3.3 Device characterization

To investigate device optical response, we used light with a wavelength of 1550 nm, sourced from an Agilent 81640A tunable laser. This light, channeled through a tapered single-mode fiber with a 2.5±0.5 microns spot size, was introduced into the silicon waveguide. For optimal results, we ensured the light maintained a quasi transverse electric (TE) mode, utilizing polarization paddles. The optical power injected from the tapered fiber was adjusted and calibrated using a Thorlab VOA50 variable optical attenuator

and an integrating sphere Thorlab PM400 power meter. Optical coupling and transfer waveguide propagation loss resulted in a total loss from fiber to detector of 4 dB.

For DC characterization, a Keithley 2400 source meter was used to control the bias and capture the photocurrent of the devices. The high frequency S_{21} response of the device were measured with an HP8719C vector network analyzer, where a 1550 nm optical carrier was used to modulate the injected RF sweep signal from the VNA. The devices were set in forward-bias V_{ce} mode using GS RF probes, facilitated by the Keithley source meter combined with a bias tee. The collector was connected to a positive voltage to reverse-bias the collector-base junction, ensuring that the phototransistor is primed to respond to incident light. single side band (SSB) phase noise characteristics were measured using a pure RF signal at 1 GHz modulated using an optical carrier at 1550 nm and subsequently the electrical spectrum was measured using a high resolution (5 Hz) electrical spectrum analyzer (ESA). For comparison, data was acquired from devices with different configurations of floating p^+-doping regions.

3.4 Experimental results

3.4.1 Steady-state response

The device operates under both positive and negative V_{CE} due to the n-i-p-i-n doping structure, which resembles an n-p-n type bipolar phototransistor [30]. Due to the asymmetry of the device geometry and doping, the phototransistor exhibits different electrical characteristics under different biasing polarity. The emitter is more heavily doped than the collector, thus when operating in the forward V_{CE} regime, the emitter region is able to provide more electrons to tunnel through the base region for extraction by the collector, resulting in significant photocurrent as demonstrated in Fig. 3.2 (a).

The optimized device where the two p^+-doped regions of 0.75 µm width are separated by a distance of 1 µm, exhibits dark current of 4 nA and 4 µA under V_{CE} of -1 V and

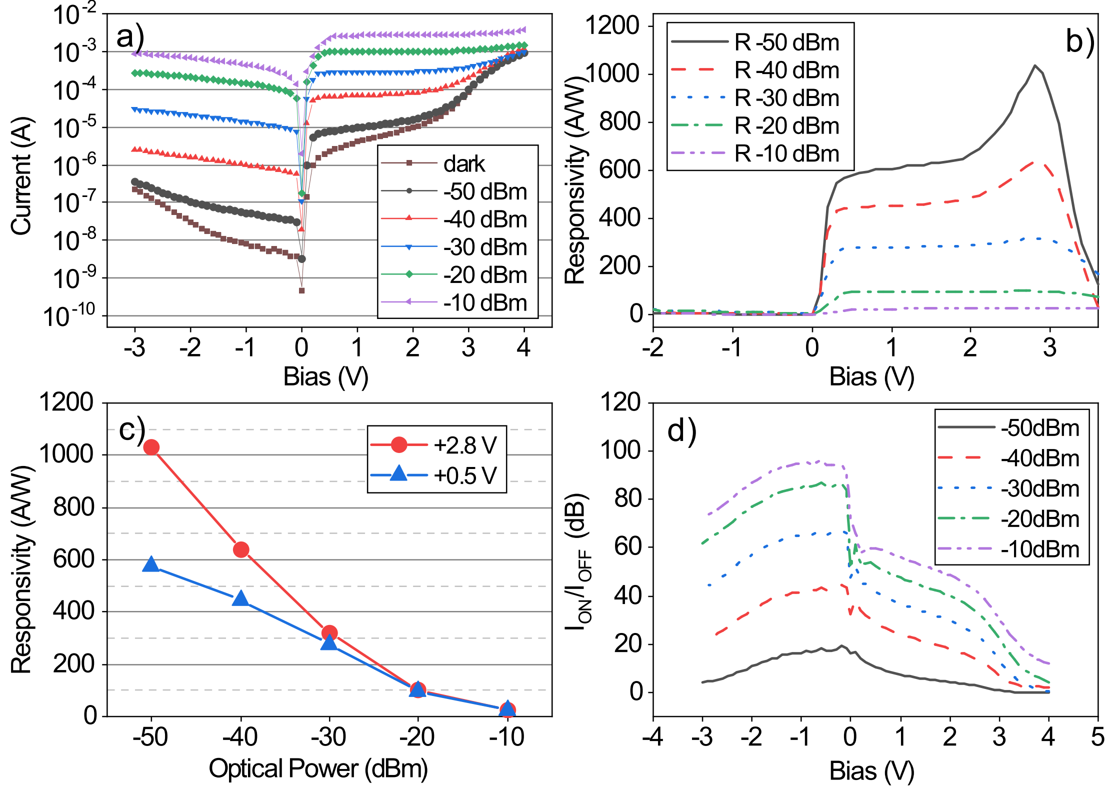

FIGURE 3.2: a, b) Device dark current, illuminated current, and responsivity under different incident power levels with incident light at 1550 nm; c) responsivity versus optical power at different applied voltage; d) I_{ON}/I_{OFF} ratio of the device under different incident power levels.

1 V respectively. An illuminated current of 440 µA and 2600 µA are obtained under these biases when the device is injected with TE polarized light at 1550 nm with a power of -10 dBm, corresponding to a responsivity of 4.4 A/W and 26 A/W respectively. In reverse bias, the lower responsivity arises because the collector is less heavily doped than the emitter, leading to a reduced availability of carriers. It is noted that under these conditions, the phototransistor enters the high injection regime with a relatively high intensity of optical power present in the device. This generates a surplus of minority carriers that are injected into the transistor's base region, leading to a low photocurrent gain.

The injected optical power was decreased from -10 to -50 dBm using the optical attenuator. The illuminated current decreased from 440 µA and 2600 µA to 56 nA and 10 µA under a forward and reverse V_{CE} of 1V respectively. However, the device responsivity was increased from 26 to 606 A/W under 1 V V_{CE} as shown in Fig. 3.2 (b), due to the transition from the high injection regime to the normal operation regime. Compared to previous work on phototransistors fabricated using silicon photonics technology [28] where at -30dBm optical power, responsivity of 232 A/W with a dark current of 45 µA at 5 V, and 42 A/W with 9 µA dark current at 1 V were reported, the optimized device in this work exhibits responsivity of 318 A/W with a dark current of 42 µA at 2.8 V, and 281 A/W with 4 µA dark current at 1 V. Besides, the I_{ON}/I_{OFF} ratio (defined as $I_{ON}/I_{OFF}(dB) = 20log(I_{illumated}/I_{dark})$) increased to 16 dB and 36 dB at 5 V and 1 V respectively compared to 5 dB from [28].

A maximum responsivity of 1032 A/W was obtained under a forward bias of 2.8 V with an optical power of -50 dBm, where the dark current is 42 µA. This is a significant improvement over previously reported work using a commercial Si photonics platform [28], and the first report of >1000 A/W responsivity on this platform. The responsivity of the device rapidly rolls off above 3 V_{CE} due to the increase of the dark current. Thus the optimal working regime of the device is between 0.5 V and 3 V under forward V_{CE}.

Fig. 3.2 (c) shows the responsivity at V_{CE} = 0.5 V and V_{CE} = 2.8 V versus optical power. The device responsivity decreases as optical power increases due to the increasing injection of carriers in the base region. Despite its high responsivity, the device sensitivity is compromised by the dark current at low optical power levels even in these dark current suppressed designs. As shown in Fig. 3.2 (d), the I_{ON}/I_{OFF} ratio drops from 56.0 dB to 7.4 dB at 1 V as the input power is reduced from -10 dBm to -50 dBm.

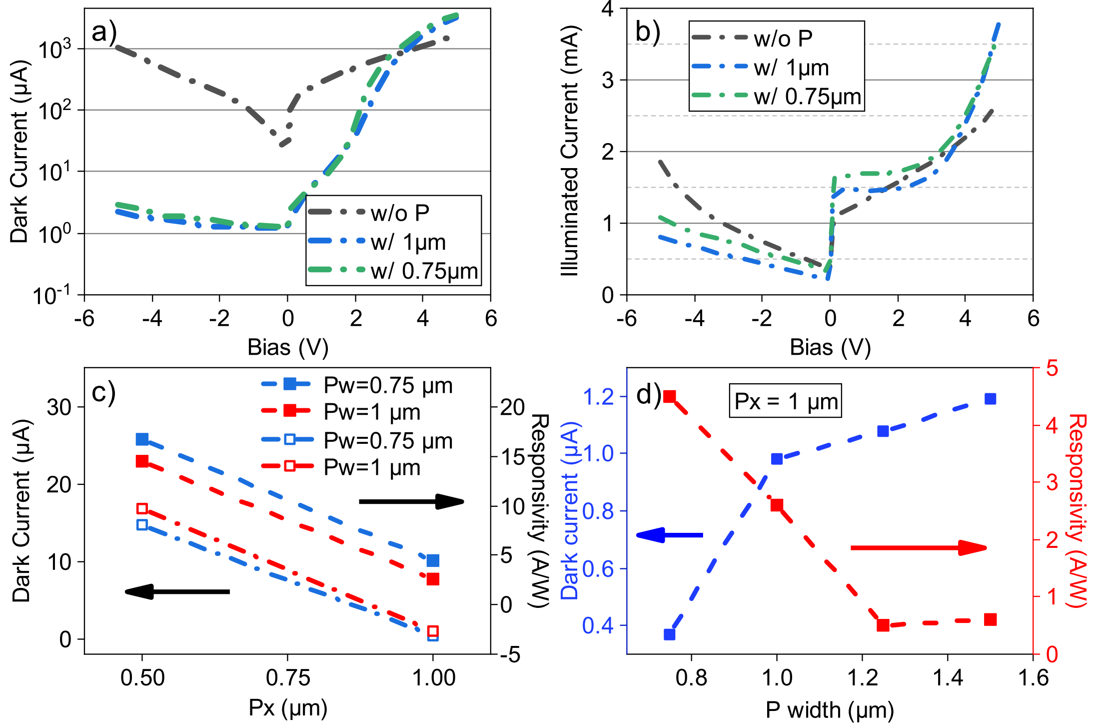

FIGURE 3.3: a) Dark current, b) illuminated current (-10 dBm optical power), for devices with different geometries (without p$^+$-doped regions, with 1 μm and 0.75 μm width p$^+$-doped region); device dark current and responsivity comparisons with c) varying p$^+$-doped regions distances, and d) varying p$^+$-doped region widths.

3.4.2 Assessing the impact of the floating p-doped regions

The device design introduces p$^+$-doped regions with the aim to suppress the dark current and enhance the photocurrent as described in Fig. 3.1. Fig 3.3 (a) shows the dark current comparison between devices without p$^+$-doped regions and with floating p$^+$-doped regions (of varying width) beneath the Ge epitaxy. The dark current is reduced by two orders of magnitude from 285 μA to 4 μA at 1V V_{CE}, and from 575 μA to 2 μA at -4V V_{CE} for device with p$^+$-doped regions of 1 μm width and 1 μm separation. With p$^+$-doped regions, illuminated current (Fig 3.3 (b)) increased from 1.3 mA to 1.5 mA and 1.7 mA at 1 V V_{CE} with -10 dBm optical power by introducing the p$^+$-doped region under Ge layer with widths of 1 μm and 0.7 μm, respectively. This is explained

by the band adjustment in the device. Photo-generated holes are drifted to the base region in the electrical field with a forward V_{CE} bias, resulting in a higher concentration of holes, which leads to a higher bias on the base-emitter junction and a lower potential barrier. Consequently, more electrons can be injected from the emitter to the base region, contributing to an increased photocurrent.

The increase in photocurrent and decrease in dark current collectively contribute to the increase of the device responsivity from 20.5 A/W to 28.9 A/W and 33.6 A/W at -10 dBm with floating p^+-doped regions of 1 µm and 0.75µm widths respectively. We also note that the dark current can be suppressed to even lower values of less than 1 µA at 1 V V_{CE} by increasing the distance between the two p^+-doped regions from 1 µm to 2 µm, which, however, would also significantly decrease the photocurrent of the device to approximately 500 µA, resulting in a lower responsivity.

The geometrical details of the p^+-doped regions, particularly their width and separation, have a significant impact on the performance metrics of the phototransistor, as shown in Fig 3.3 (c) and (d). For devices with p^+ widths of 0.75 µm and 1 µm, increasing the separation between adjacent p^+-regions reduces the dark current from a high of 20 µA to less than 1 µA, a trend attributable to the suppression of the carrier transport channel. However, this comes at the cost of responsivity, which also drops from an initial 15 A/W to below 5 A/W. Reducing the separation between the p^+ regions, while maintaining their individual widths, effectively narrows the high potential barrier regions, as depicted in Fig.3.1. This narrowing makes it more challenging for carriers to traverse these barriers directly. Consequently, more carriers are inclined to follow the lower potential barrier path along the Si/Ge interface, which is not within the p+ regions. This shift in carrier path effectively broadens the overall low potential pathway for carrier transportation across the device, enhancing conductivity under both dark and illuminated conditions. This change results in the observed increase in both

dark current and photocurrent. Moreover, the expansion of this lower potential pathway predominantly occurs at the Si/Ge interface. This interface is significant due to the excess carriers generated by the Si/Ge lattice mismatch. Therefore, an increase in the interface area not only augments the overall carrier pathway but also intensifies the generation of dark current due to the lattice mismatch-induced excess carriers. The key to optimizing the spacing between p+ regions lie in balancing the trade-offs between dark current and responsivity. The optimal spacing is determined by the specific application's requirements and its tolerance for dark current.

Conversely, when the separation remains unchanged, narrowing the width of the p^+-regions leads to a desirable reduction in dark current from 1.2 µA to 0.4 µA, while concurrently improving responsivity from 0.6 A/W to 4.5 A/W. The best balance between these factors is found in a device featuring a 0.5 µm p^+-region separation and 0.75 µm p^+-region width.

3.4.3 Electrical bandwidth and phase noise

The dynamic photodetector response is shown in Fig. 3.4, where devices with different p^+-region widths were measured while varying the bias voltage.

We observed a small signal -3 dB bandwidth of 1.5 GHz and 1 GHz under forward and reverse bias, respectively, where the frequency responses are slightly higher in forward bias due to lower device resistance. All frequency responses were measured using an electrical vector network analyzer (VNA: HP 8719C) and by measuring the S_{21} scattering parameter directly from the VNA. We used a 1550 nm optical carrier to modulate the injected RF sweep signal from the VNA. We measured a –3dB small-signal bandwidth of 1.5 GHz as compared to the conventional photodiodes with tens of GHz. The small-signal response of the phototransistor is primarily limited by the reversed biased B-C junction capacitance as the device consists of a relatively large B-C junction area.

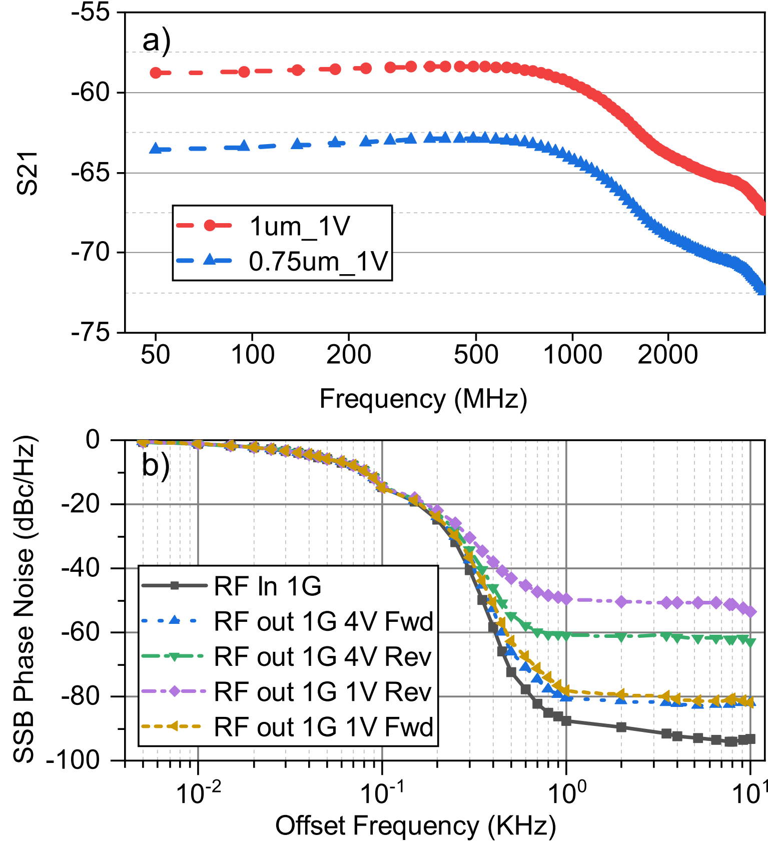

FIGURE 3.4: a) 3-dB bandwidth for devices with 1 µm and 0.75 µm p^+-region widths under 1 V_{CE}; b) Phase noise with 1 GHz RF carrier for device with 0.75 µm p^+-region under different biases of V_{CE}(1 V, 4 V, and -4 V).

Additionally, the base acts as an input to the phototransistor, hence the large junction capacitance is further enhanced by the Miller effect [31]. Therefore, the device bandwidth is significantly compromised. Nevertheless, this structure offers lower noise current than conventional avalanche photodiodes. Note that the device bandwidth can be improved significantly by reducing its length. For the proposed phototransistor, we have designed it for a length of 200 µm which can further be shortened to a conventional $\tilde{2}0$ µm without sacrificing the photocurrent due to the high optical absorption coefficient of Ge. Such a device modification not only boosts the small-signal bandwidth, but also improves the dark current of the phototransistor.

Single side band (SSB) phase noise characteristic was measured for different bias voltage using a pure RF signal at 1 GHz modulated with an optical carrier at 1550 nm and subsequently the electrical spectrum was measured using a high resolution (5 Hz) electrical spectrum analyzer (ESA) placed after the photodetector. The results are plotted in Fig. 3.4 (b). The measured spectrum density depicts a SSB phase noise of -80 dBc/Hz at 1 KHz offset for an -90 dBc/Hz RF input signal. Such a low SSB phase noise characteristic is viable for application in LIDAR for example, where the phase noise (PN) performance is a paramount design criteria [32].

3.5 Discussion and Conclusion

Table 3.1 provides a summary of recent results for phototransistors on a silicon photonics commercial platform with various structures and material systems. Each type of phototransistor utilizes a distinct operational principle, leading to varied advantages and drawbacks in terms of responsivity, dark current, bandwidth, and compatibility with Si photonics foundries. The study by Frounchi et al. [33] utilized a Ge BJT structure, achieving a responsivity of 80 A/W at 4V, with a notable bandwidth of 10 GHz. In contrast, Sorianello et al. [28] employed a Si/Ge BJT structure, which exhibited a higher responsivity of 232 A/W at 5V and a minimal optical power requirement of 1µW. Going et al. [34] explored the potential of a Ge MOSFET structure, which, while having a lower responsivity of 18 A/W at 1.75V, showed a bandwidth of 2.5 GHz. The 2D FET structure presented by Fu et al. [35] achieved a high responsivity of 3.5×10^4 A/W at 20V, highlighting the potential of 2D materials in this domain. Ochiai et al. [18] introduced a Si/InGaAs FET structure with an impressive responsivity of 10^6 A/W at 1V. In the present work, a Si/Ge BJT structure was employed, achieving a responsivity of 1032 A/W and 606 A/W at 2.8V and 1V with dark currents of 42 µA and 4 µA, respectively. Dark current density of 2.1×10^{-7} A/µm and 2×10^{-8} A/µm are obtained under these biases for a device with a 200 µm length, which is significantly lower than

previously reported devices fabricated with silicon photonics technology.

In summary we have demonstrated a Si/Ge waveguide integrated phototransistor with engineered electric field which operates with high responsivity of 606 A/W, low dark current of 4 µA, and low phase noise of -80 dBc/Hz under a low bias of 1 V for input power of -50 dBm. A high responsivity of 1032 A/W with a dark current of 42 µA was obtained under 2.8 V bias. It should be noted that the bias condition significantly impacts the dark current characteristics and hence the overall interpretation of the device's performance, particularly in low-light applications where dark current is a significant performance indicator. The p^+-doping regions under the Ge epitaxial layer, was demonstrated to increase photocurrent gain and suppress the dark current compared to a reference device without the p^+-regions. Dark current and responsivity can be engineered by varying the location of the p^+-doped regions. A narrower width of the p^+ regions may contribute to higher responsivity and lower dark current. A -80 dBc/Hz phase noise response at 1 KHz frequency offset was obtained experimentally. Small signal -3dB bandwidth of 1.5 GHz is mainly limited by the base-collector junction capacitance. High responsivity combined with low dark current and acceptable phase noise enables detectivity of light with a wide range of powers. The device is suitable for monolithic integration with advanced CMOS processes operating under a 2V supply and applications involving optical power of the order of nW range, requiring low dark current and phase noise characteristics.

Table 3.1: A performance summary of selected phototransistors on silicon photonics platform.

	Device structure	Responsivity (A/W)	Optical power (mW)	Dark current (µA)	D.C. density (A/µm)	Bandwidth (GHz)	Si Photonics Foundry
[33]	Ge BJT	80 @4V	\	\	\	10	Yes
[28]	Si/Ge BJT	232 @ 5V	0.001	45	2.5E-6	\	Yes
[36]	Si/Ge JFET	36 @2V	0.001	33	1.8E-6	\	Yes
[34]	Ge MOSFET	18 @ 1.75	5.8E-4	\	\	2.5	No
[37]	Silicide Schottky-Barrier	0.024	1	0.09	4.4E-7	0.4	No
[38]	Si Membrane	0.007	\	0.01	1E-10	\	No
[35]	2D FET	3.5E4 @20V	2E-7	0.01	1E-10	\	No
[18]	Si/InGaAs FET	1E6 @1V	6E-10	60	2E-6	\	No
this work	Si/Ge BJT	1032 @ 2.8V	1E-5	42	2.1E-7	1.5	Yes
this work	Si/Ge BJT	606 @ 1V	1E-5	4	2E-8	1.5	Yes

Bibliography

[1] D. Thomson, A. Zilkie, J. E. Bowers, T. Komljenovic, G. T. Reed, L. Vivien, D. Marris-Morini, E. Cassan, L. Virot, J.-M. Fédéli, *et al.*, Roadmap on silicon photonics, *Journal of Optics*, vol. 18(7), 073 003, 2016.

[2] Y. Jiang, P. T. DeVore, and B. Jalali, Analog optical computing primitives in silicon photonics, *Optics letters*, vol. 41(6), 1273–1276, 2016.

[3] J. Bao, Z. Fu, T. Pramanik, J. Mao, Y. Chi, Y. Cao, C. Zhai, Y. Mao, T. Dai, X. Chen, *et al.*, Very-large-scale integrated quantum graph photonics, *Nature Photonics*, vol. 17(7), 573–581, 2023.

[4] V. C. Duarte, J. G. Prata, C. F. Ribeiro, R. N. Nogueira, G. Winzer, L. Zimmermann, R. Walker, S. Clements, M. Filipowicz, M. Napierała, *et al.*, Modular coherent photonic-aided payload receiver for communications satellites, *Nature communications*, vol. 10(1), 1984, 2019.

[5] C. Dhote, A. Singh, and S. Kumar, Silicon photonics sensors for bio-photonic applications-a review, *IEEE Sensors Journal*, 2022.

[6] Y. Kang, H.-D. Liu, M. Morse, M. J. Paniccia, M. Zadka, S. Litski, G. Sarid, A. Pauchard, Y.-H. Kuo, H.-W. Chen, *et al.*, Monolithic germanium/silicon avalanche photodiodes with 340 ghz gain–bandwidth product, *Nature photonics*, vol. 3(1), 59–63, 2009.

[7] D. Benedikovic, L. Virot, G. Aubin, J.-M. Hartmann, F. Amar, X. Le Roux, C. Alonso-Ramos, É. Cassan, D. Marris-Morini, F. Boeuf, *et al.*, Silicon-germanium

avalanche receivers with fj/bit energy consumption, *IEEE Journal of Selected Topics in Quantum Electronics*, vol. 28(2: Optical Detectors), 1–8, 2021.

[8] H. Chen, J. Verbist, P. Verheyen, P. De Heyn, G. Lepage, J. De Coster, P. Absil, X. Yin, J. Bauwelinck, J. Van Campenhout, *et al.*, High sensitivity 10gb/s si photonic receiver based on a low-voltage waveguide-coupled ge avalanche photodetector, *Optics Express*, vol. 23(2), 815–822, 2015.

[9] M. Huang, S. Li, P. Cai, G. Hou, T.-I. Su, W. Chen, C.-y. Hong, and D. Pan, Germanium on silicon avalanche photodiode, *IEEE Journal of Selected Topics in Quantum Electronics*, vol. 24(2), 1–11, 2017.

[10] Y. Peng, Y. Yuan, W. V. Sorin, S. Cheung, Z. Huang, M. Fiorentino, and R. G. Beausoleil, All-silicon microring avalanche photodiodes with a> 65 a/w response, *Optics Letters*, vol. 48(5), 1315–1318, 2023.

[11] J. J. Ackert, D. J. Thomson, L. Shen, A. C. Peacock, P. E. Jessop, G. T. Reed, G. Z. Mashanovich, and A. P. Knights, High-speed detection at two micrometres with monolithic silicon photodiodes, *Nature Photonics*, vol. 9(6), 393–396, 2015, ISSN: 17494893.

[12] M. Geis, S. Spector, M. Grein, R. Schulein, J. Yoon, D. Lennon, S. Deneault, F. Gan, F. Kaertner, and T. Lyszczarz, Cmos-compatible all-si high-speed waveguide photodiodes with high responsivity in near-infrared communication band, *IEEE Photonics Technology Letters*, vol. 19(3), 152–154, 2007.

[13] Y. Gao, F. Guo, R. Das, P. Mascher, and A. P. Knights, High responsivity si/ge phototransistor on silicon photonics platform for small signal application, in *2023 Photonics North (PN)*, IEEE, 2023, 1–1.

[14] H. Chen, P. Verheyen, P. De Heyn, G. Lepage, J. De Coster, S. Balakrishnan, P. Absil, G. Roelkens, and J. Van Campenhout, Dark current analysis in high-speed

germanium pin waveguide photodetectors, *Journal of Applied Physics*, vol. 119(21), 2016.

[15] Y. Gao, F. Guo, P. Mascher, and A. P. Knights, Monolithic silicon avalanche photodetector utilizing surface state defects operating at 1550 nm, in *Silicon Photonics XVIII*, SPIE, vol. 12426, 2023, 61–65.

[16] X. Sang, E.-K. Tien, and O. Boyraz, Applications of two photon absorption in silicon, *Journal of optoelectronics and advanced materials*, vol. 11(1), 15, 2009.

[17] M. Pantouvaki, P. Verheyen, G. Lepage, J. De Coster, H. Yu, P. De Heyn, P. Absil, and J. Van Campenhout, 20gb/s silicon ring modulator co-integrated with a ge monitor photodetector, in *39th European Conference and Exhibition on Optical Communication (ECOC 2013)*, IET, 2013, 1–3.

[18] T. Ochiai, T. Akazawa, Y. Miyatake, K. Sumita, S. Ohno, S. Monfray, F. Boeuf, K. Toprasertpong, S. Takagi, and M. Takenaka, Ultrahigh-responsivity waveguide-coupled optical power monitor for si photonic circuits operating at near-infrared wavelengths, *Nature Communications*, vol. 13(1), 7443, 2022.

[19] J. T. Spollard, L. E. Roberts, C. S. Sambridge, K. McKenzie, and D. A. Shaddock, Mitigation of phase noise and doppler-induced frequency offsets in coherent random amplitude modulated continuous-wave lidar, *Optics Express*, vol. 29(6), 9060–9083, 2021.

[20] J.-P. Zhuang and S.-C. Chan, Phase noise characteristics of microwave signals generated by semiconductor laser dynamics, *Optics Express*, vol. 23(3), 2777–2797, 2015.

[21] A. Ishizawa, T. Nishikawa, A. Mizutori, H. Takara, A. Takada, T. Sogawa, and M. Koga, Phase-noise characteristics of a 25-ghz-spaced optical frequency comb based on a phase-and intensity-modulated laser, *Optics Express*, vol. 21(24), 29 186–29 194, 2013.

[22] B. Qi, Y.-M. Chi, H.-K. Lo, and L. Qian, High-speed quantum random number generation by measuring phase noise of a single-mode laser, *Optics letters*, vol. 35(3), 312–314, 2010.

[23] W. Zhang, S. Seidelin, A. Joshi, S. Datta, G. Santarelli, and Y. L. Coq, Dual photo-detector system for low phase noise microwave generation with femtosecond lasers, *Opt. Lett.*, vol. 39(5), 1204–1207, 2014.

[24] I. M. Anjum, E. Simsek, S. E. J. Mahabadi, T. F. Carruthers, and C. R. Menyuk, Design and analysis of low bias, low phase noise photodetectors for frequency comb applications using particle swarm optimization, in *2022 IEEE International Topical Meeting on Microwave Photonics (MWP)*, 2022, 1–4.

[25] M. B. Gray, D. A. Shaddock, C. C. Harb, and H.-A. Bachor, Photodetector designs for low-noise, broadband, and high-power applications, *Review of Scientific Instruments*, vol. 69(11), 3755–3762, Nov. 1998, ISSN: 0034-6748.

[26] R. Das, Y. Xie, H. Frankis, K. Chen, H. Rufenacht, G. Lamontagne, J. D. B. Bradley, and A. P. Knights, Gain-enabled optical delay readout unit using cmos-compatible avalanche photodetectors, *Photon. Res.*, vol. 10(10), 2422–2433, 2022.

[27] N. DiLello, D. Johnstone, and J. Hoyt, Characterization of dark current in ge-on-si photodiodes, *Journal of Applied Physics*, vol. 112(5), 054 506, 2012.

[28] V. Sorianello, G. De Angelis, A. De Iacovo, L. Colace, S. Faralli, and M. Romagnoli, High responsivity sige heterojunction phototransistor on silicon photonics platform, *Optics Express*, vol. 23(22), 28 163–28 169, 2015.

[29] K.-W. Ang, M.-B. Yu, G.-Q. Lo, and D.-L. Kwong, Low-voltage and high-responsivity germanium bipolar phototransistor for optical detections in the near-infrared regime, *IEEE electron device letters*, vol. 29(10), 1124–1127, 2008.

[30] S. M. Sze, Y. Li, and K. K. Ng, *Physics of semiconductor devices*. John Wiley & Sons, 2021.

[31] D. Neamen, *Semiconductor physics and devices*. McGraw-Hill, Inc., 2002.

[32] M. Jahangir, J. M. Jones, J. Kannanthara, C. J. Baker, K. Bongs, M. Antoniou, and Y. Singh, Development of quantum enabled staring radar with low phase noise, in *2021 18th European Radar Conference (EuRAD)*, IEEE, 2022, 225–228.

[33] M. Frounchi, G. N. Tzintzarov, A. Ildefonso, and J. D. Cressler, High responsivity ge phototransistor in commercial cmos si-photonics platform for monolithic optoelectronic receivers, *IEEE Electron Device Letters*, vol. 42(2), 196–199, 2020.

[34] R. W. Going, J. Loo, T.-J. K. Liu, and M. C. Wu, Germanium gate photomosfet integrated to silicon photonics, *IEEE Journal of Selected Topics in Quantum Electronics*, vol. 20(4), 1–7, 2013.

[35] Q. Fu, C. Zhu, X. Zhao, X. Wang, A. Chaturvedi, C. Zhu, X. Wang, Q. Zeng, J. Zhou, F. Liu, *et al.*, Ultrasensitive 2d bi2o2se phototransistors on silicon substrates, *Advanced Materials*, vol. 31(1), 1 804 945, 2019.

[36] V. Sorianello, G. De Angelis, L. Colace, S. Faralli, M. Romagnoli, *et al.*, Germanium gate phototransistor fabricated on soi platform, in *2015 IEEE 12th International Conference on Group IV Photonics (GFP)*, IEEE, 2015, 19–20.

[37] S. Zhu, G. Lo, M. Yu, and D. Kwong, Silicide schottky-barrier phototransistor integrated in silicon channel waveguide for in-line power monitoring, *IEEE Photonics Technology Letters*, vol. 21(3), 185–187, 2008.

[38] R. Pan, Q. Guo, J. Cao, G. Huang, Y. Wang, Y. Qin, Z. Tian, Z. An, Z. Di, and Y. Mei, Silicon nanomembrane-based near infrared phototransistor with positive and negative photodetections, *Nanoscale*, vol. 11(36), 16 844–16 851, 2019.

Chapter 4

Monolithic silicon avalanche photodetector utilizing surface state defects operating at 1550 nm

Reprinted in part with open access permissions from: Yuxuan Gao, Feng Guo, Peter Mascher, Andrew P. Knights. Si/Ge Monolithic silicon avalanche photodetector utilizing surface state defects operating at 1550 nm. *Silicon Photonics XVIII*. Vol. 12426. SPIE, 2023.

https://doi.org/10.1117/12.2651724

This chapter includes the findings presented in a published manuscript on the fabrication and characterization of defect-mediated all silicon avalanche photodetectors utilizing surface state defects (SSD) and bulk defect absorption (BDA) effects. Device optical response and electrical response were investigated with different defect levels and types, with an optimized device responsivity of 4 A/W and 3 dB bandwidth of around 8 GHz

obtained. Sections included in the following chapter which were not published in the manuscript include the discussion of fabrication and characterization. Fig. 4.2, Fig. 4.4, 4.5, and the discussion in Section 4.4 discussing the surface oxidation are also included here. These alterations were made to better explain how surface states degrade with time and the effect of their contribution to the overall photocurrent.

4.1 Abstract

In this work, we report on all-silicon waveguide photodetectors utilizing surface state defects and bulk defects to sensitize the silicon to sub-bandgap light. The detectors are foundry fabricated, waveguide-integrated p-i-n junctions with post-processing consisting of HF acid exposure, ion implantation, annealing, or a combination of the three. HF exposure increases the photoresponse of the as-received detectors due to the increase in unpassivated surface states. The efficiency of surface state detection is greater than that for bulk defect detection in terms of mode overlap with the defected volumes of the silicon waveguide. Detectors in all cases have a 3dB bandwidth of around 8 GHz.

4.2 Introduction

Silicon photonics has significant economic advantages over other photonic platforms, such as III-V compounds and polymers, motivating both academia and industry to invest efforts in the development of silicon optoelectronics technology[1–3]. Silicon photonic integrated circuits (PICs) are designed to manipulate light in silicon, supporting functionality such as light generation, modulation, routing, processing, and detection[4]. Despite the cost advantages of silicon, its indirect bandgap of 1.1 eV results in very poor optical absorption at the conventional telecommunication wavelengths region.

Approaches based on different sub-bandgap absorption mechanisms have been demonstrated to improve the response of all-silicon photodetectors at telecommunication wavelengths, including two-photo absorption (TPA), mid-bandgap absorption (MBA), and surface state absorption (SSA). Photodetectors based on TPA require a relatively high optical power to overcome the low TPA coefficient and initiate the nonlinear effect[5], which makes them non-ideal for small signal detection. MBA can be achieved by introducing foreign atoms into the bulk of the device, producing defects as deep electronic levels in the silicon bandgap[6–8]. In addition to deep levels formed in the silicon bulk, mid-bandgap energy levels can be produced by surface states, which result from dangling bonds at interfaces such as the silicon-air boundary.

Mid-bandgap absorption can be achieved also via bulk defects absorption (BDA), where the defects are introduced by inert ion implantation into the silicon crystal structure. The tuneable concentration and the distribution of the implanted ions (by controlling the implantation dose and energy) are considered the main advantages of this method. In this case, a deep level with charge-state energy located below the conduction band can provide electron-hole pair generation through a two-step process. First, the absorption of a photon excites an electron from the valence band to the deep level. Second, the electron is thermally excited from the deep level into the conduction band. In 2006, Knights *et al.* proposed a waveguide photodetector using ion implantation with a p-i-n diode integrated, reaching a responsivity of 9 mA/W [6]. The responsivity of this silicon photodetector was enhanced with ring resonators fabricated with electron beam lithography, reaching a responsivity of 39 mA/W at a 20 volt reverse bias[7]. Fast operation (35 GHz) of similar devices were fabricated and characterized to have responsivity of 1-2 A/W at 20 volts by Geis *et al.*[9].

Surface state defects (Figure 4.1) can be formed at the silicon detector surface. This effect has been known to increase the optical absorption in the early 1970s[10]. This

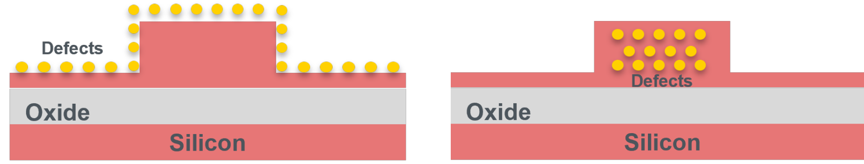

FIGURE 4.1: Schematic show of surface state defects (left) and bulk defects (right).

effect was deployed into photodetectors in 2008, where Baehr-Jones *et al.* proposed a photodetector with sensitivity at C-band wavelength by removing the top silicon dioxide cladding and exposing the silicon waveguide to the air[11]. Chen *et al.* proposed an all-silicon p-i-n photodetector with a reponsivity of 0.25 mA/W, where they attribute the linear absorption to surface state absorption[12]. An avalanche photodetector from Zhu *et al.* reached a responsivity of 2.33 $A/W$by improving surface state absorption with reduced waveguide width [13], while a 2 mm long silicon photodetector utilizing surface-state absorption with 0.045 A/W reponsivity was achieved by Ackert *et al.* [14].

4.3 Fabrication and Characterization

4.3.1 Device Fabrication

The devices reported in this study were fabricated at AMF in Singapore using the Silicon Photonics Multi-Project Wafer (MPW) process, grounded on 193 nm deep-ultraviolet lithography. The silicon-on-insulator (SOI) <100> wafers with a silicon thickness of 220 nm were etched to form waveguides with a nominal width of 1000 nm over 2 µm of buried oxide. Along the chip's perimeter, the waveguide narrows from a 1000 nm width over a distance of 300 µm, eventually merging with a nanotaper coupler optimized for efficiently channeling light from a single-mode fiber. As shown in Figure 4.2, the employed detector structures were of the p-i-n type created by implanting boron and phosphorus into the 90 nm thick slab regions 300 nm from the edge of the waveguide. The oxide layer above the p-i-n junction was selectively etched with 2 µm in width and 750 µm in length at

the foundry to form an activated surface and unveil a site for the inert ion implantation.

Doubly charged argon and boron ions were implanted into the intrinsic waveguide region with doses ranging from 5^{10} to $8^{11} cm^{-2}$ and an energy of 30 KeV, at the Centre for Emerging Devices and Technologies (CEDT), McMaster University, which is followed by annealing at 200 °C for 5 minutes in an air ambient. This process introduced vacancy- and interstitial-type defects to the lattice in the bulk region of the silicon waveguide, forming deep-level states in the silicon bandgap and increasing the bulk defect absorption (BDA) in the infrared region.

Deep-level states have been introduced into the silicon bandgap through the creation of surface state defects (SSD) by removing the naturally occurring silicon dioxide layer using a 5% buffered hydrofluoric acid solution. This process results in dangling bonds at the silicon-air interfaces, which are formed as the surface is exposed to ambient air. These deep-level states facilitate the absorption of light at sub-bandgap wavelengths, creating a pathway for optical transitions. Such transitions can occur through two potential mechanisms: electron excitation from the valence band to unoccupied states just above the Fermi level, or from states slightly below the Fermi level to the conduction band, as described in [15].

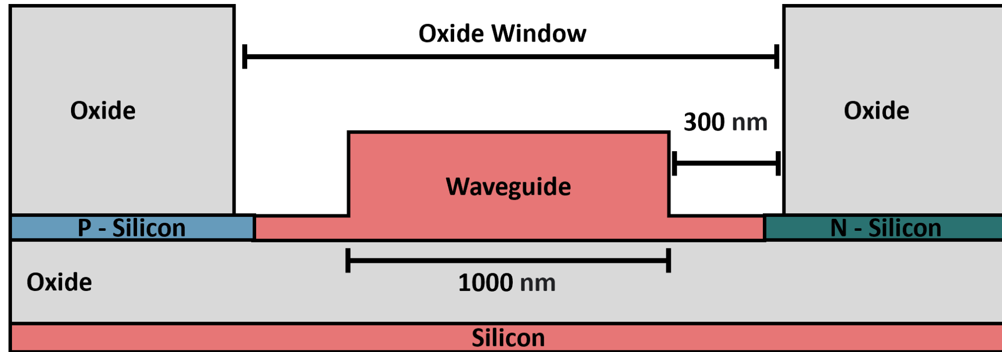

FIGURE 4.2: Cross-sectional diagram of the p-i-n diode.

Table 1 presents an overview of the devices used in this study, where the symbols

#Ref, #SSD, and #BDA correspond to the as-received device, the device with surface states, and the device with bulk defects (doubly charged argon ions implanted), respectively. Moreover, the device #BDA_SSD is the #BDA device equipped with surface states. The waveguides of the Ref and #BDA_SSD devices were exposed to the atmosphere for 30 days, leading to the formation of native silicon dioxide on their surfaces. To introduce surface states at the Si/air interface, 5% buffered hydrofluoric acid was used to remove the native silicon dioxide layer. The #BDA_SSD_Oxide device was produced by depositing a 10 nm thin layer of silicon dioxide on the exposed surface of the #BDA_SSD device using an electron cyclotron resonance plasma enhanced chemical vapor deposition (ECR-PECVD) system [16] to passivate the surface states.

Device Code	Post process
#Ref	As-received
#SSD	As-received + HF
#BDA	As-received + Implantation
#BDA_SSD	As-received + Implantation + HF
#BDA_SSD_Oxide	As-received + Implantation + HF + Oxide

TABLE 4.1: Device summary with post process details

4.3.2 Device Characterization

To characterize the optical response of the devices, linearly polarized light at 1550 nm was edge-coupled into the silicon waveguide from a tapered single-mode fiber with a spot diameter of 2.5±0.5 microns from a tunable laser source (Agilent 81640A). Quasi transverse electric (TE) mode was maintained using polarization controlling paddles to maximize the optical response of the devices. A multimeter (Keithley 2400) is used to control the bias and extract the photocurrent of the devices. The total optical power reaching the detector was calibrated to be -3 dBm with an integrating sphere photodiode optical powermeter (Thorlab PM400). The overall throughput loss of a circuit including

two edge couplers and a straight waveguide is approximately 8 dB with a fiber-fiber loss of 4 dB. The high frequency S_{21} response of the device was measured with a vector network analyzer (Anritsu 37397C). For comparison, data was also acquired from an unaltered device, where carrier generation is believed to occur through mid-gap states present at the Si/ambient interface.

4.4 Results and discussions

The responsivity of the as-received (reference) device, SSD device, and the BDA device are shown in Figure 4.3. It is worth mentioning that the reference device has a thin layer of silicon oxide on the silicon ridge waveguide region despite efforts to remove all SiO_2 by the foundry. This will be discussed further. Compared to the reference device with a photocurrent of 5.8 μA at a reverse bias of 15 V, the SSD device with 60 seconds HF etching has a photocurrent of 32.6 μA, corresponding to a responsivity of 0.06 A/W. The BDA device has a photocurrent of 82.7 μA and a responsivity of 0.16 A/W at 15 V . The BDA device shows a responsivity more than twice that of the SSD device, because of the higher defect concentration in the bulk silicon region.

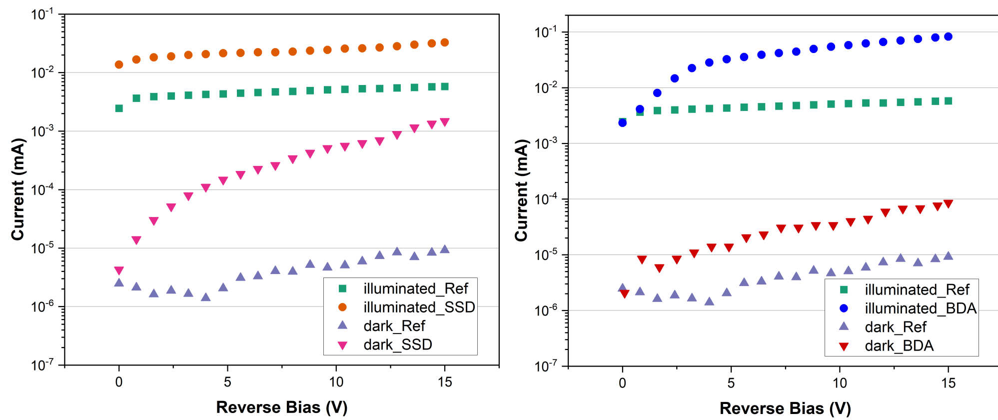

FIGURE 4.3: Measured illuminated currents and dark currents of reference device, SSD device, and BDA device.

The dark current increased significantly from 9 nA for the reference device to 1483

nA with SSD and to 85.5 nA with BDA, indicating possibly different mechanisms for how SSDs and bulk defects assist carrier drift/conductivity, which requires further investigation.

SSD detectors and BDA detectors operate optimally in different bias regimes. The BDA detectors show a stronger photocurrent enhancement at higher bias, but a small photocurrent at low bias $(0 - 2V)$. Comparatively, the surface-state detectors show a significantly better response at low bias, but lacks high responsivity in the higher bias regime.

Figure 4.3 also provides information on the effect of bulk defects on the detector. At low bias, significant recombination at defect centres reduces the photocurrent, while in the surface-state device carriers can be extracted with relatively high efficiency as only the surface acts as a source of recombination. At high bias, there is a significant increase in photocurrent (a result of avalanche multiplication) for the bulk defect device, but this effect is not observed in the surface-state device.

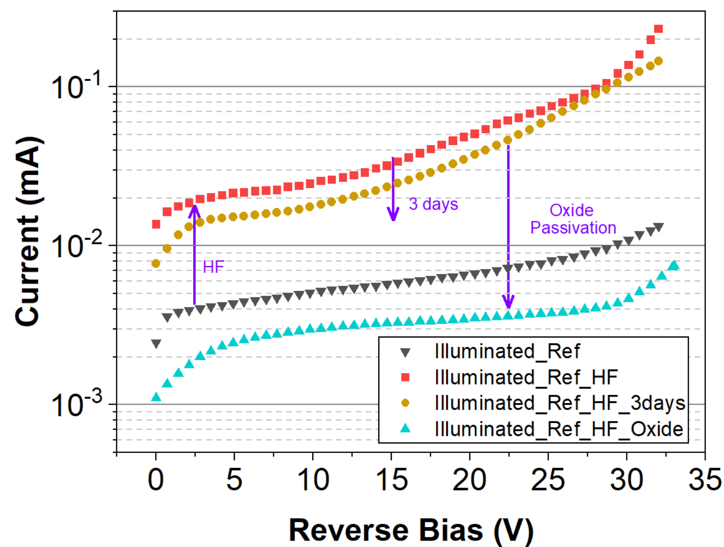

FIGURE 4.4: Photocurrent of devices before and after surface state defects activation, after native-grown oxide and controlled surface oxidation.

The passivation and stability of SSDs have been investigated, as shown in Figure 4.4. This figure displays the photocurrent measurements of devices before and after SSD activation (Ref and Ref_HF), following native oxide growth (Ref_HF_3days), and after surface oxidation (Ref_HF_Oxide). The photocurrent of the device subjected to SSD activation (HF) increased by nearly an order of magnitude, from 7.8 to 70.9 μA under a reverse bias of 25 V compared to that of the reference sample. The absorption of the SSDs resulted in an additional waveguide loss of 2 dB, leading to an internal quantum efficiency of approximately 30%, which is higher than that of BDA detectors.

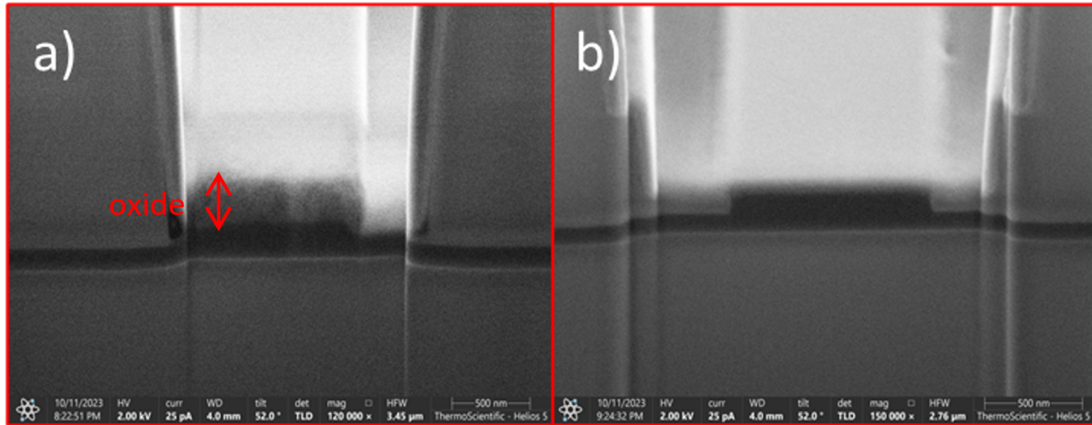

FIGURE 4.5: SEM image of device a) as received and b) HF etched.

Examination of the device surface status is shown in Fig. 4.5, where the left image shows a thick oxide layer (around 250 nm) on top of silicon for as-received chips from the foundry, and the right image shows the oxide layer post HF etching and subjected to exposure to ambient environment after one month. After exposure to air at room temperature for 3 days (corresponding to an oxide thickness of approximately 8 Å[17]), the photocurrent of the SSD-activated device remained high, with a slight drop to 60.0 μA. Even after one month of exposure, the photocurrent of the device still demonstrated a significant amount of enhancement from the SSDs, owing to the equilibrium oxide thickness at room temperature being less than 14 Å[17] (data not shown) and oxidation of silicon generating excess self-interstitials at the interface of SiO_2 and Si which contributes

to the photocurrent [18]. Finally, the photocurrent dropped to 4.7 μA, which is lower than that of the original reference device (7.8 μA), after deposition of a 10-nm-thick silicon dioxide layer, confirming the reduction of the SSDs. It should be noted that the reference sample had its top oxide layer removed at the foundry, which may explain the additional photocurrent drop after 10-nm-thick oxide deposition.

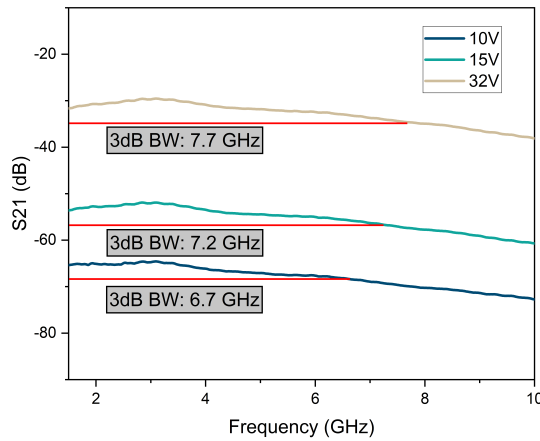

FIGURE 4.6: Bandwidth measurement of SSD devices under various biases (10 V, 15 V, and 32 V).

The dynamic response of the photodetector is shown in Figure 4.6, where 750 µm long devices with both types of defects were measured. Similar responses were obtained for both SSD devices and BDA devices. We observed a 3-dB bandwidth of 6.7 to 7.7 GHz under various reverse biases. We attribute the increase in response to the expansion of the junction depletion region.

4.5 Summary

Monolithic silicon photodetectors utilizing surface state defects and bulk defects were designed, fabricated and characterized. The best device achieved a responsivity of nearly 0.16 A/W under a reverse bias of 15 V with BDA introduced, and a 3-dB bandwidth of 7.7 GHz was obtained. Surface state defects are demonstrated to significantly increase

the photocurrent of the photodetector due to the deep levels in the silicon bandgap introduced by the defects at silicon/air interface, despite the limited overlap between surface region and the TE mode optical profile. The results are important for future designs of monolithic silicon photodetectors, as both types of defects can be used for device modification after fabrication. SSD detectors are primarily attractive for their ease of fabrication and consequently their integration into complex photonic integrated circuits, despite their lower responsivity compared to the BDA detectors.

Bibliography

[1] A. S. Mayer and B. C. Kirkpatrick, Silicon photonics, *Frontiers in Modern Optics*, vol. 24(12), 189–205, 2016, ISSN: 18798195.

[2] M. J. S. Shawon and F. Li, A review of the building blocks of silicon photonics: From fabrication perspective, *Semiconductor Science and Information Devices*, vol. 1(1), 29–35, 2019.

[3] Y. Gao, Z. Khatami, and P. Mascher, Influence of Nitrogen on the Luminescence Properties of Ce-Doped SiO_xN_y, *ECS Journal of Solid State Science and Technology*, vol. 10(7), 076 005, ISSN: 2162-8769.

[4] S. Y. Siew, B. Li, F. Gao, H. Y. Zheng, W. Zhang, P. Guo, S. W. Xie, A. Song, B. Dong, L. W. Luo, *et al.*, Review of silicon photonics technology and platform development, *Journal of Lightwave Technology*, vol. 39(13), 4374–4389, 2021.

[5] M. Casalino, G. Coppola, R. M. De La Rue, and D. F. Logan, State-of-the-art all-silicon sub-bandgap photodetectors at telecom and datacom wavelengths, *Laser and Photonics Reviews*, vol. 10(6), 895–921, 2016, ISSN: 18638899.

[6] A. P. Knights, J. D. B. Bradley, S. H. Gou, and P. E. Jessop, Silicon-on-insulator waveguide photodetector with self-ion-implantation-engineered-enhanced infrared response, *Journal of Vacuum Science & Technology A: Vacuum, Surfaces, and Films*, vol. 24(3), 783–786, 2006, ISSN: 0734-2101.

[7] D. F. Logan, P. Velha, M. Sorel, R. M. De La Rue, A. P. Knights, and P. E. Jessop, Defect-enhanced silicon-on-insulator waveguide resonant photodetector with high

sensitivity at 1.55 μm, *IEEE Photonics Technology Letters*, vol. 22(20), 1530–1532, 2010.

[8] J. J. Ackert, D. J. Thomson, L. Shen, A. C. Peacock, P. E. Jessop, G. T. Reed, G. Z. Mashanovich, and A. P. Knights, High-speed detection at two micrometres with monolithic silicon photodiodes, *Nature Photonics*, vol. 9(6), 393–396, 2015, ISSN: 17494893.

[9] M. W. Geis, S. J. Spector, M. E. Grein, J. U. Yoon, D. M. Lennon, and T. M. Lyszczarz, Silicon waveguide infrared photodiodes with >35 GHz bandwidth and phototransistors with 50 AW-1 response, *Optics Express*, vol. 17(7), 5193, 2009, ISSN: 10944087.

[10] G. Chiarotti, S. Nannarone, R. Pastore, and P. Chiaradia, Optical absorption of surface states in ultrahigh vacuum cleaved (111) surfaces of ge and si, *Physical review B*, vol. 4(10), 3398, 1971.

[11] T. Baehr-Jones, M. Hochberg, and A. Scherer, Photodetection in silicon beyond the band edge with surface states, *Optics Express*, vol. 16(3), 1659, 2008, ISSN: 1094-4087.

[12] H. Chen, X. Luo, and A. W. Poon, Cavity-enhanced photocurrent generation by 1.55 μm wavelengths linear absorption in a p-i-n diode embedded silicon microring resonator, *Applied Physics Letters*, vol. 95(17), 2009, ISSN: 00036951.

[13] H. Zhu, L. Zhou, Y. Zhou, Q. Wu, X. Li, and J. Chen, All-silicon waveguide avalanche photodetectors with ultrahigh gain-bandwidth product and low breakdown voltage, *IEEE Journal of Selected Topics in Quantum Electronics*, vol. 20(6), 226–231, 2014, ISSN: 15584542.

[14] J. J. Ackert, A. S. Karar, J. C. Cartledge, P. E. Jessop, and A. P. Knights, Monolithic silicon waveguide photodiode utilizing surface-state absorption and operating at 10 gb/s, *Optics Express*, vol. 22(9), 10 710, 2014, ISSN: 10944087.

[15] J. S. Orcutt, S. D. Tang, S. Kramer, K. Mehta, H. Li, V. Stojanović, and R. J. Ram, Low-loss polysilicon waveguides fabricated in an emulated high-volume electronics process, *Optics Express*, vol. 20(7), 7243–7254, 2012.

[16] F. Azmi, Y. Gao, Z. Khatami, and P. Mascher, Tunable emission from Eu: SiO_xN_y thin films prepared by integrated magnetron sputtering and plasma enhanced chemical vapor deposition, *Journal of Vacuum Science & Technology A*, vol. 40(4), 2022.

[17] S. Raider, R. Flitsch, and M. Palmer, Oxide growth on etched silicon in air at room temperature, *Journal of the Electrochemical Society*, vol. 122(3), 413, 1975.

[18] F. Shimura, *Semiconductor silicon crystal technology.* Elsevier, 2012.

Chapter 5

Slow Light Enhanced Monolithic Silicon Photodetector Using Subwavelength Grating Waveguides

This chapter includes the design, simulation, fabrication, and measurement results for a slow-light-enhanced monolithic silicon avalanche photodetector. Slow light at 1550 nm was achieved at the band edge of the dispersion relationship of the subwavelength grating (SWG) waveguide, which is acting as the core optical absorption region. Responsivity between un-doped devices and devices doped with Si^{+} are compared, leading to the development of a figure of merit of responsivity per unit length to describe the slow light gain more accurately due to the lossy nature of the long SWG waveguides. Enhanced responsivity due to slow light on silicon photonics is demonstrated for the first time to the best of the author's knowledge. This work represents a manuscript which is in preparation by the authors and has been included in the thesis due to its considerable responsivity for light signal detection for optical communication and the

ease of fabrication with only one post fabrication step (ion implantation) needed.

5.1 Abstract

In this study, we present a monolithically integrated silicon waveguide avalanche photodetector, fabricated utilizing conventional silicon photonics technology. A significant enhancement in responsivity, achieving 5 A/W, is attributed to the presence of slow light within the subwavelength grating (SWG) waveguide. This performance marks a notable improvement over the reference device without the SWG waveguide. This advancement underscores the potential of integrating SWG structures in silicon photonics for enhanced photodetector efficiency.

5.2 Introduction

Over the last three decades, silicon photonics has evolved from a niche research area to a major commercial platform, encompassing a wide range of applications, including optical interconnects [1], optoelectronics [2], sensors for biological and chemical analysis [3], LiDAR systems [4], and analog optical computing [5]. The cornerstone of this evolution is the integration and interaction of various photonic elements such as lasers, modulators, waveguides, and photodetectors.

A significant challenge in silicon photonics is rooted in silicon's inherent nature as an indirect band gap semiconductor, transparent in the O, C, and L bands. Although facilitating low-loss transmission, this characteristic fundamentally restricts its effectiveness in photodetection within the mid-infrared telecommunication spectrum. To address these constraints, direct band gap materials, particularly III-V semiconductors such as InGaAs [6] and GaAs [7], as well as Ge [8], have been utilized to achieve high optical to electrical conversion efficiency. Despite these advancements, the monolithic integration

of Si-based photodetectors remains an attractive approach, owing to its relatively simple fabrication process and resultant cost-effectiveness [9].

All-silicon photodetectors exploiting sub-bandgap detection mechanisms have garnered increasing attention in recent years. Various methodologies leveraging sub-bandgap absorption have been investigated. These include two-photon absorption (TPA) [10, 11], band tunneling photoexcitation [12], bulk defect absorption (BDA) [13–16], and surface state defect absorption (SSD) [17–19]. This collective exploration underscores the potential of silicon-based photodetectors in efficiently harnessing sub-bandgap light.

To enhance light absorption and thus responsivity and bandwidth of silicon-based photodetectors, device structural modifications can be considered to improve light-matter interaction within their active detection regions, such as through the use of slow light supporting waveguides. The phenomenon of slow light has been shown previously to significantly enhance light-matter interactions, as demonstrated in applications such as sensing [20–22], optical force enhancement [23], and light amplification [24]. Notably, slow light has also been utilized in a phosphorus-based photonic crystal waveguide photodetector with a responsivity enhancement of more than tenfold [25], and a silicon photonic crystal photodiode with a responsivity of 0.36 A/W [26]. Slow light can be realized through relatively simple periodic structures such as sub-wavelength gratings (SWG). Near the Bragg reflection regime of the grating structures, slow light propagates below the band edge, leading to a significant increase in group index and light matter interaction.

In this study, we introduce a monolithic Si-based photodetector, specifically engineered for mid-infrared light detection. A key feature of this photodetector is the integration of a sub-wavelength grating (SWG) waveguide to exploit the phenomenon of slow light. Our approach employs a foundry-compatible process, facilitating the straightforward incorporation of SWGs to support slow light propagation. This method also

provides flexibility to modify design parameters, ensuring adaptability to different wavelengths.

5.3 Method

5.3.1 Device design

The device is a waveguide-integrated photodiode configured in a p-i-n structure, as depicted in Fig. 5.1 (a). When exposed to near-infrared light, photo-generated carriers created through mid-bandgap defects and drift towards the p-doped and n-doped regions. The carriers are then extracted to the external circuit. Under a high reverse bias in the avalanche region, the device experiences an amplification of the photocurrent, facilitated by the high electric field in the i-region.

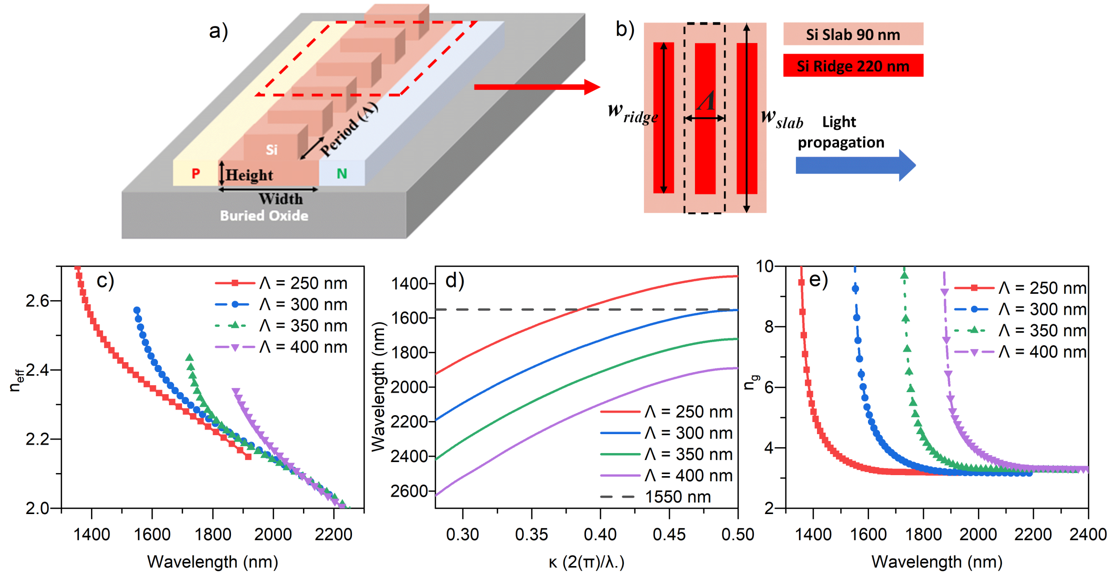

FIGURE 5.1: a) Device structure, b) SWG waveguide diagram of the device, c) simulated effective index, d) band diagram, and e) group index of the devices with a duty cycle of 0.5 and varied periods from 250 nm to 400 nm.

The silicon SWG waveguide is designed with a period of 300 nm and duty cycles of 0.5 and 0.47 on the top ridge, which has a height of 220 nm and a nominal width of 1

µm. The slab region of the waveguide has a height of 90 nm as illustrated in Fig. 5.1 (b). Mode conversion from the routing strip waveguide to the slow light SWG waveguides is achieved through physical tapers. These SWG tapers, 12 µm in length, gradually alter the waveguide width from 500 nm at the input to 140 nm at the output. The SWG blocks in the taper region gradually increases in width from 500 nm to 1 µm, maintaining a relatively consistent effective index and ensuring a smooth mode transition. Fig. 5.1 (c) shows the simulated effective indices and (d) shows the simulated optical bandgaps of the SWG waveguide for different periods. Here, $\Lambda = 300nm$ corresponds to a band edge located at 1550 nm, indicating strong dispersion leading to slow light at this wavelength. The group index, extracted from the band diagram and presented in Fig. 5.1 (e), reaches a value higher than 10 at the wavelength of 1550 nm for a SWG waveguide with a period of 300 nm. This high group index in the slow light regime significantly enhances light-matter interaction, leading to enhanced optical response of the mid-level defects to light at this wavelength. A significant benefit is then a proportionate decrease in photodiode length circumventing the main disadvantage of all-silicon photodetectors [27].

Fig. 5.2 illustrates the simulated Floquet-Bloch modes propagating in the SWG waveguide in both the slow light (1550 nm) and deep SWG (1600 nm) regimes. At 1600 nm, the SWG waveguide behaves optically equivalent to a uniaxial crystal with the optic axis aligned along the light propagation direction, resulting in lossless localized Floquet–Bloch modes [28, 29], as shown in Fig. 5.2 (v) and (vi). Conversely, at 1550 nm, the occurrence of slow light is attributed to a decrease in group velocity, stemming from the curvature of the waveguide's optical band-edge. The Bloch mode in the slow light regime is reshaped compared to the mode in the SWG regime, exhibiting greater concentration within the high-index silicon region. This localization effect, depicted in Fig. 5.2 (i), (ii), and (iii), enhances light-matter interaction nonlinearly in the slow light regime [30], contributing to the photodetector's enhanced photo response in the presence of mid-bandgap defects.

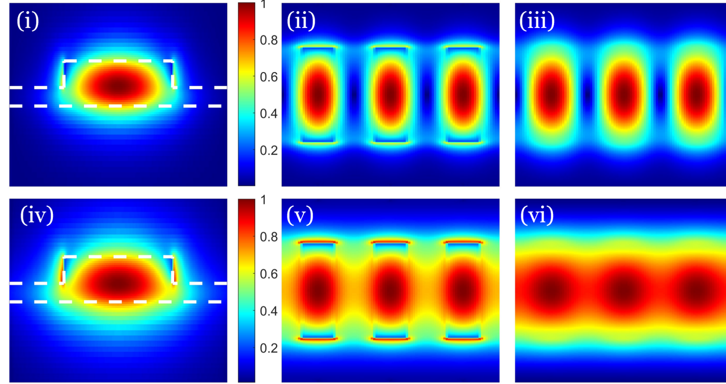

FIGURE 5.2: Simulated Floquet-Bloch mode propagating in the SWG waveguide at slow light regime (1550 nm) with cross-section view(i), top view at the ridge region (ii) and slab region (iii), and SWG regime (1600 nm) with cross-section view(iv), top view at the ridge region (v) and slab region (vi).

5.3.2 Device fabrication

Device fabrication was conducted at the Advanced Micro Foundry (AMF), Singapore, using a 193 nm ultraviolet lithography multi-project wafer (MPW) process, facilitated by CMC Microsystems of Canada. Silicon-on-insulator (SOI) wafers of <100> orientation, featuring a silicon thickness of 220 nm, were etched to create SWG ridge waveguides with a nominal width of 1 µm and length of 750 µm, situated atop 2 µm of buried oxide. Doping regions within the silicon layer were established through the implantation of boron (p-type) and phosphorus (n-type) into the 90 nm thick waveguide slab region, resulting in p and n doping of the order of $1 \times 10^{20} cm^{-3}$. The intrinsic (i) region of the silicon with a width of 1.6 µm (separation between the p and n doped regions) was slightly p-doped to approximately $5 - 10 \times 10^{15}$ cm^{-3}. Mid-bandgap levels are always present at the Si-SiO_2 interface albeit their concentration may vary significantly depending upon the surface treatment [9]. Additionally, mid-gap defects can be deliberately and controllably introduced in the waveguide bulk through inert ion implantation, for example by using Si^+ ions. In the present study such implantation was performed at an energy of 4.2 MeV for varying doses of between 5×10^{11} to $1 \times 10^{12} cm^{-2}$. Subsequent to

ion implantation in these cases was a low temperature annealing process at 200 °C for 5 minutes in air.

5.3.3 Device characterization

To assess the optical response of the device, light ranging in wavelength from 1520 nm to 1600 nm was sourced from an Agilent 81640A tunable laser. This light was edge coupled into the silicon waveguide via a tapered single-mode fiber, featuring a spot size of 2.5±0.5 microns. To achieve optimal results, the light was maintained in a quasi transverse electric (TE) mode using polarization paddles. The injected optical power from the tapered fiber was finely adjusted and calibrated and measured using an integrating sphere Thorlab PM400 power meter. Taking into account the circuit's losses, which included passive components (polarization paddles and fiber connectors) and fiber to chip coupling loss, a total background loss of 6 dB was observed for each measurement. An optical power of 0 dBm from the tunable laser reaching the photodetector was thus calibrated to be around -3 dBm (0.5 mW). For DC characterization, a Keithley 2400 source meter was utilized to control the bias and measure the photocurrent of the devices. For comparative analysis, data was also gathered from photodetectors that employed a conventional ridge waveguide configuration, equipped with the same mode converter but without an SWG structure.

5.4 Experimental Results and Discussion

5.4.1 Intrinsic photodetector characterization

The optical transmissions across the wavelength range from 1520 nm to 1600 nm for both the SWG waveguide (with duty cycles of 0.50 and 0.47) and the conventional reference waveguide are illustrated in Fig.5.3 (a). The fiber-to-fiber transmission loss for the reference straight strip waveguide was measured at 4.8 dB at 1550 nm. Additionally, the transition loss from the tapered fiber to the edge coupler, as well as the routing strip

waveguide propagation loss, were determined to be approximately 2 dB/facet and 2.3 dB/cm, respectively, using a cut-back method.

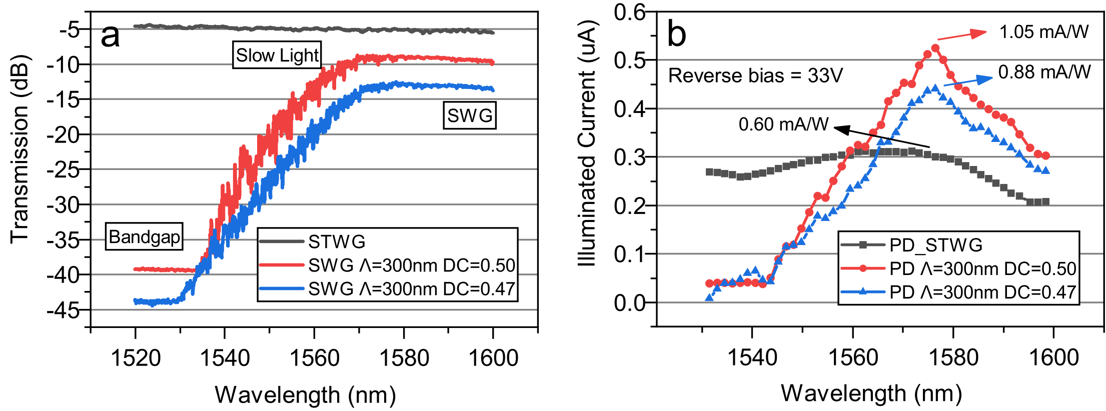

FIGURE 5.3: a) Fiber-to-fiber transmission of the reference straight waveguide (STWG) and the slow light (SWG) device test structure for $\Lambda = 300nm$ and duty cycle of 0.5 and 0.47; b) Illuminated current from the corresponding photodetectors of these waveguide structures. Dark current (not shown) is below 0.3 nA at a bias of 33V (avalanche) for all the devices.

For the SWG waveguide with a duty cycle of 0.50, the transmission demonstrates stable excess loss across the deep SWG spectrum, implying efficient light propagation through the waveguide with an estimated propagation loss of around 26 dB/cm, comparable to previously reported values of 25 dB/cm [30]. In contrast, the waveguide with a duty cycle of 0.47 exhibits a relatively higher propagation loss, which is due to the reduced effective refractive index of the waveguide, leading to a delocalized mode and reduced mode confinement. Additionally, a smaller duty cycle translates to finer feature sizes, making the structure more susceptible to fabrication variations and imperfections such as slanted or collapsed silicon pillars [30]. Examining transmission losses near the central operating wavelength is crucial for assessing the waveguide design's effectiveness. At wavelengths around 1550 nm, the SWG waveguides are specifically engineered to operate within the slow light regime which is characterized by a substantial rise in propagation loss which increases non-linearly with the group index in the waveguide structure [30–33]. Such a design aims to significantly enhance the light absorption

within the photodetector. Any TE polarized light with a wavelength below around 1540 nm is considered as within the optical bandgap of the SWG structure, where no optical mode is allowed due to Bragg exclusion.

The photocurrent, as depicted in Fig. 5.3 (b), reveals the relationship between the wavelength and the detector's optical response in avalanche mode with a reverse bias of 33 V, with a notably enhanced responsivity within the slow light regime compared to the reference device. Here the generation of electron-hole pairs is solely attributed to the surface (interface) defects. Although the simulation shows a lower group index at 1575 nm compared to that at shorter wavelengths, peak responsivity occurs at this wavelength where a balance is struck between the augmented light-matter interaction from the increased group index and the optical loss of the waveguide. In comparison to the reference device's responsivity of 0.6 mA/W, the photocurrent from both SWG configurations exhibits an increase to 1.05 mA/W and 0.88 mA/W for duty cycles of 0.5 and 0.47, respectively. This underscores the SWG's pivotal role in boosting the photodetector's efficiency. At wavelengths shorter than 1575 nm, despite the increased group index, the optical response of the SWG devices starts to drop rapidly due to the relatively high propagation loss. In the deep SWG regime with wavelength longer than 1575 nm, SWG devices still maintain relatively higher photocurrent than the reference device, which can be attributed to the expanded evanescent field due to reduced effective index interacting with the surface state defects. Furthermore, we note that a minor alteration in duty cycle from 0.50 to 0.47 significantly impacts the index contrast and device response, presenting an opportunity for precise adjustments in the device's sensitivity and optical bandwidth.

The surface state defects at the Si-SiO_2 interface, situated between the waveguide and the top oxide cladding, are considered to be the dominant factor contributing to the overall device photocurrent in Fig. 5.3. This is particularly notable due to the extremely

low light absorption in intrinsic silicon at 1550 nm, reported to be 264$\pm$39 parts per million (ppm)/cm [34]. Such low absorption can be considered negligible for converting the absorbed optical signal to an electrical signal. The combination of localized modes with slow light results in a nonlinear enhancement of light-matter interaction, particularly the interaction between the propagating light and the SSDs. Moreover, SWG structures are capable of increasing the Si-SiO_2 interface surface area compared to conventional straight waveguides, which further enhances the responsivity of the device.

Due to the non-negligible propagation loss in the SWG waveguide, it is inaccurate to assume a uniform light intensity throughout the entire length of the photodetector's active region. Fig. 5.4 (a) presents the normalized light intensity in both waveguide types across different locations within the device, based on the propagation losses calculated from optical transmission measurements. It is observed that the optical power remains relatively homogeneous in the straight ridge waveguide, while it attenuates rapidly in the SWG waveguide, exhibiting a propagation loss of 26 dB/cm. To accurately represent the device responsivity across different waveguide lengths, the overall responsivity is determined by integrating the optical power over a specific length of the corresponding waveguide and then calculating the ratio of this integrated power to the total length. Knowing the responsivity of the 750 µm devices for both reference and SWG waveguides allows us to calibrate the plot to show absolute responsivities as depicted in Fig. 5.4 (b). In the straight waveguide with low attenuation, responsivity increases almost linearly with device length. However, in the SWG waveguide, total responsivity saturates at longer lengths due to diminished optical power in the distant regions from the input side. Consequently, increasing the SWG device length does not significantly enhance the photocurrent. We note that in fact, a long waveguide length in the case of the SWG has a detrimental effect in terms of electrical bandwidth due to increased capacitance. This will be discussed further. Fig. 5.4 (c) illustrates the responsivity per unit length for both photodetector types, showing that the SWG photodetector, with a shorter device length,

exhibits almost triple the optical response compared to a reference straight waveguide, attributable to enhanced light-matter interaction (specifically an increase in the effective cross-section for light-defect absorption).

In the design of the current photodetector, we have meticulously replicated the structural dimensions and doping profiles of a previously fabricated and characterized device, which demonstrated an electrical bandwidth of approximately 7-8 GHz [35, 36]. The device length, doping concentrations in the p-n junction, and the width of the intrinsic region are kept identical to the prior model. Notably, the variation between the two designs resides solely in the waveguide grating structure. Since the grating pertains to the optical domain and its impact on the electrical response is negligible, it is reasonable to estimate that the electrical bandwidth will remain within the 7-8 GHz range, as observed in the previous iteration.

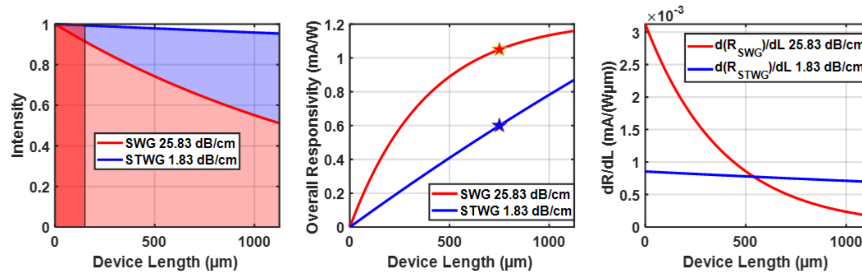

FIGURE 5.4
a) Optical power attenuation in the waveguide (SWG and reference straight waveguide) as a function of device length; b) Calculated device responsivity as a function of device overall length calibrated with measured responsivity values; c) Calculated responsivity per unit length as a function of device length.

5.4.2 Enhanced responsivity with mid-bandgap defects

To increase light absorption in the near-infrared region, Si^+ ions are implanted into the silicon SWG region at an energy of 4.2 MeV with varying doses varying from 5×10^{11} to $1 \times 10^{12} cm^{-2}$ followed by low temperature annealing to create deep levels within the silicon bandgap. Increased optical absorption post-ion implantation is confirmed in both

the reference straight waveguide and SWG waveguide structures, as illustrated in Fig. 5.5 (a). Compared to the un-doped structures, the reference STWG exhibits a 2 dB and 6.7 dB increase in loss from transmission measurements with doses of 5×10^{11} and $1 \times 10^{12} cm^{-2}$, respectively. In contrast, the SWG structure shows increases of 3.3 dB and 8.2 dB in loss. It is important to note that due to the SWG structure's 50% duty cycle, it has a smaller bulk silicon volume compared to the STWG, which is comprised entirely of silicon. Consequently, after implantation, a lower aggregate of defects is expected in the SWG compared to the STWG, as evidenced by the SWG's smaller dark current. Despite having fewer defects (deep levels), the SWG structure consistently exhibits a higher increase in loss compared to the STWG.

The increase in loss due to implanted defects leads to a desired enhancement in the optical response when compared to un-implanted devices. As shown in Fig. 5.5 (b), the illuminated current of the STWG with incident TE light at 1575 nm increased from 0.3 µA to 1.73 mA and 2 mA for doses of 5×10^{11} and $1 \times 10^{12} cm^{-2}$, respectively, while the dark current rose to 3.4 µA and 13.6 µA. In contrast, for the SWG device, the illuminated current increased from less than 1 µA to 1.67 mA and 2.45 mA, with corresponding increases in dark current to 2.3 µA and 10.7 µA. It is noteworthy that the illuminated current from the SWG device is not consistently higher than that from the STWG device, even with equivalent ion implantation doses, due to the SWG structure's higher propagation losses. The responsivity per unit length, calculated using the method described in Section 5.4.1, is presented in Fig. 5.5 (c). Here, the responsivity per 1 µm for both SWG devices with the two different doses is about three times that of the STWG with corresponding doses. This increased responsivity is attributed to the enhanced light-matter interaction between the optical signal and the deep levels created by implantation.

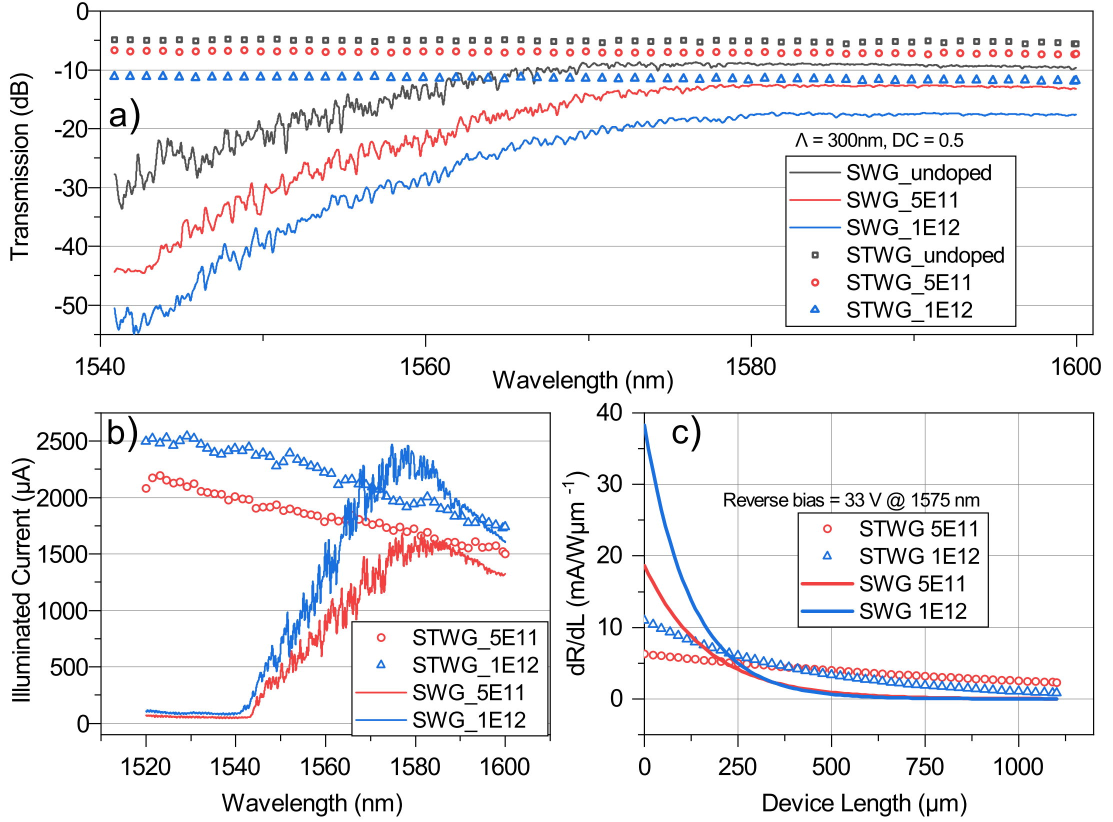

FIGURE 5.5
a) Fiber-to-fiber transmission of the reference straight waveguide (STWG) and the slow light (SWG) device test structure for $\Lambda = 300nm$ and duty cycle of 0.5 with different implantation dose levels: un-implanted, 5E11, and 1E12 cm^{-2}; b) Illuminated current from the corresponding photodetectors of these waveguide structures with incident optical power of 0.5 mW under a reverse bias of 33 V; c) Calculated responsivity per unit length as a function of device length for different implantation doses.

5.5 Conclusion

This study presents an innovative all-Si avalanche photodetector, enhanced for mid-infrared light detection using sub-wavelength grating (SWG) waveguides and deep levels to exploit slow light phenomena. This approach partially mitigates the limitations of silicon's indirect bandgap in photodetection. Our design integrates a p-i-n structured photodiode within a SWG waveguide, optimized to maximize light-matter interaction.

Experimental results reveal a substantial increase in optical response compared to traditional straight waveguide detectors in terms of responsivity per length.

In conclusion, the incorporation of SWG waveguides into silicon photodetectors offers a promising avenue for enhancing their efficiency in mid-infrared applications.

Bibliography

[1] D. Thomson, A. Zilkie, J. E. Bowers, T. Komljenovic, G. T. Reed, L. Vivien, D. Marris-Morini, E. Cassan, L. Virot, J.-M. Fédéli, *et al.*, Roadmap on silicon photonics, *Journal of Optics*, vol. 18(7), 073 003, 2016.

[2] V. C. Duarte, J. G. Prata, C. F. Ribeiro, R. N. Nogueira, G. Winzer, L. Zimmermann, R. Walker, S. Clements, M. Filipowicz, M. Napierała, *et al.*, Modular coherent photonic-aided payload receiver for communications satellites, *Nature communications*, vol. 10(1), 1984, 2019.

[3] C. Dhote, A. Singh, and S. Kumar, Silicon photonics sensors for bio-photonic applications-a review, *IEEE Sensors Journal*, 2022.

[4] X. Zhang, K. Kwon, J. Henriksson, J. Luo, and M. C. Wu, A large-scale micro electro mechanical-systems-based silicon photonics lidar, *Nature*, vol. 603(7900), 253–258, 2022.

[5] J. Bao, Z. Fu, T. Pramanik, J. Mao, Y. Chi, Y. Cao, C. Zhai, Y. Mao, T. Dai, X. Chen, *et al.*, Very-large-scale integrated quantum graph photonics, *Nature Photonics*, vol. 17(7), 573–581, 2023.

[6] Z. Sheng, L. Liu, J. Brouckaert, S. He, and D. Van Thourhout, Ingaas pin photodetectors integrated on silicon-on-insulator waveguides, *Optics Express*, vol. 18(2), 1756–1761, 2010.

[7] C. Errando-Herranz, A. Y. Takabayashi, P. Edinger, H. Sattari, K. B. Gylfason, and N. Quack, Mems for photonic integrated circuits, *IEEE Journal of Selected Topics in Quantum Electronics*, vol. 26(2), 1–16, 2019.

[8] J. Michel, J. Liu, and L. C. Kimerling, High-performance ge-on-si photodetectors, *Nature photonics*, vol. 4(8), 527–534, 2010.

[9] Y. Gao, F. Guo, P. Mascher, and A. P. Knights, Monolithic silicon avalanche photodetector utilizing surface state defects operating at 1550 nm, in *Silicon Photonics XVIII*, SPIE, vol. 12426, 2023, 61–65.

[10] X. Sang, E.-K. Tien, and O. Boyraz, Applications of two photon absorption in silicon, *Journal of optoelectronics and advanced materials*, vol. 11(1), 15, 2009.

[11] N. K. Hon, R. Soref, and B. Jalali, The third-order nonlinear optical coefficients of si, ge, and si 1-x ge x in the midwave and longwave infrared articles you may be interested in, *J. Appl. Phys*, vol. 110, 11 301, 2011.

[12] J.-B. You, H. Kwon, J. Kim, H.-H. Park, and K. Yu, Photon-assisted tunneling for sub-bandgap light detection in silicon pn-doped waveguides, *Optics Express*, vol. 25(4), 4284–4297, 2017.

[13] D. F. Logan, P. Velha, M. Sorel, R. M. De La Rue, A. P. Knights, and P. E. Jessop, Defect-enhanced silicon-on-insulator waveguide resonant photodetector with high sensitivity at 1.55 μm, *IEEE Photonics Technology Letters*, vol. 22(20), 1530–1532, 2010.

[14] A. P. Knights, J. D. B. Bradley, S. H. Gou, and P. E. Jessop, Silicon-on-insulator waveguide photodetector with self-ion-implantation-engineered-enhanced infrared response, *Journal of Vacuum Science & Technology A: Vacuum, Surfaces, and Films*, vol. 24(3), 783–786, 2006, ISSN: 0734-2101.

[15] J. D. B. Bradley, P. E. Jessop, and A. P. Knights, Silicon waveguide-integrated optical power monitor with enhanced sensitivity at 1550nm, *Applied Physics Letters*, vol. 86(24), 241 103, 2005, ISSN: 0003-6951.

[16] J. J. Ackert, A. S. Karar, D. J. Paez, P. E. Jessop, J. C. Cartledge, and A. P. Knights, 10 gbps silicon waveguide-integrated infrared avalanche photodiode, *Optics Express*, vol. 21(17), 19 530, 2013, ISSN: 1094-4087.

[17] M. W. Geis, S. J. Spector, M. E. Grein, J. U. Yoon, D. M. Lennon, and T. M. Lyszczarz, Silicon waveguide infrared photodiodes with >35 GHz bandwidth and phototransistors with 50 AW-1 response, *Optics Express*, vol. 17(7), 5193, 2009, ISSN: 10944087.

[18] T. Baehr-Jones, M. Hochberg, and A. Scherer, Photodetection in silicon beyond the band edge with surface states, *Optics Express*, vol. 16(3), 1659, 2008, ISSN: 1094-4087.

[19] J. J. Ackert, A. S. Karar, J. C. Cartledge, P. E. Jessop, and A. P. Knights, Monolithic silicon waveguide photodiode utilizing surface-state absorption and operating at 10 gb/s, *Optics Express*, vol. 22(9), 10 710, 2014, ISSN: 10944087.

[20] Y.-N. Zhang, Y. Zhao, D. Wu, and Q. Wang, Theoretical research on high sensitivity gas sensor due to slow light in slotted photonic crystal waveguide, *Sensors and Actuators B: Chemical*, vol. 173, 505–509, 2012.

[21] A. Gervais, P. Jean, W. Shi, and S. LaRochelle, Design of slow-light subwavelength grating waveguides for enhanced on-chip methane sensing by absorption spectroscopy, *IEEE Journal of Selected Topics in Quantum Electronics*, vol. 25(3), 1–8, 2018.

[22] Z. Gharsallah, M. Najjar, B. Suthar, and V. Janyani, Slow light enhanced bio sensing properties of silicon sensors, *Optical and Quantum Electronics*, vol. 51, 1–7, 2019.

[23] M. G. Scullion, Y. Arita, T. F. Krauss, and K. Dholakia, Enhancement of optical forces using slow light in a photonic crystal waveguide, *Optica*, vol. 2(9), 816–821, 2015.

[24] S. Ek, P. Lunnemann, Y. Chen, E. Semenova, K. Yvind, and J. Mork, Slow-light-enhanced gain in active photonic crystal waveguides, *Nature Communications*, vol. 5, 1–8, 2014, ISSN: 20411723.

[25] Y. Ma, B. Dong, J. Wei, Y. Chang, L. Huang, K.-W. Ang, and C. Lee, High-responsivity mid-infrared black phosphorus slow light waveguide photodetector, *Advanced Optical Materials*, vol. 8(13), 2 000 337, 2020.

[26] Y. Terada, K. Miyasaka, H. Ito, and T. Baba, Slow-light effect in a silicon photonic crystal waveguide as a sub-bandgap photodiode, *Optics Letters*, vol. 41(2), 289–292, 2016.

[27] M. Casalino, G. Coppola, R. M. De La Rue, and D. F. Logan, State-of-the-art all-silicon sub-bandgap photodetectors at telecom and datacom wavelengths, *Laser and Photonics Reviews*, vol. 10(6), 895–921, 2016, ISSN: 18638899.

[28] P. J. Bock, P. Cheben, J. H. Schmid, J. Lapointe, A. Delâge, S. Janz, G. C. Aers, D.-X. Xu, A. Densmore, and T. J. Hall, Subwavelength grating periodic structures in silicon-on-insulator: A new type of microphotonic waveguide, *Optics Express*, vol. 18(19), 20 251–20 262, 2010.

[29] C. M. Naraine, J. W. Miller, H. C. Frankis, D. E. Hagan, P. Mascher, A. P. Knights, J. D. Bradley, J. H. Schmid, and P. Cheben, Subwavelength grating metamaterial waveguides functionalized with tellurium oxide cladding, *2020 Photonics North, PN 2020*, vol. 28(12), 18 538–18 547, 2020.

[30] P. Jean, A. Gervais, S. LaRochelle, and W. Shi, Slow light in subwavelength grating waveguides, *IEEE Journal of Selected Topics in Quantum Electronics*, vol. 26(2), 2020, ISSN: 15584542.

[31] M. Notomi, Manipulating light with strongly modulated photonic crystals, *Reports on Progress in Physics*, vol. 73(9), 096 501, 2010.

[32] L. O'Faolain, S. A. Schulz, D. M. Beggs, T. P. White, M. Spasenović, L. Kuipers, F. Morichetti, A. Melloni, S. Mazoyer, J.-P. Hugonin, *et al.*, Loss engineered slow light waveguides, *Optics Express*, vol. 18(26), 27 627–27 638, 2010.

[33] S. A. Schulz, C. Hu, J. Upham, R. W. Boyd, and L. O'Faolain, Controllable low-loss slow light in photonic crystals, in *Steep Dispersion Engineering and Opto-Atomic Precision Metrology XI*, SPIE, vol. 10548, 2018, 9–15.

[34] J. Steinlechner, C. Kruger, N. Lastzka, S. Steinlechner, A. Khalaidovski, and R. Schnabel, Optical absorption measurements on crystalline silicon test masses at 1550 nm, *Classical and Quantum Gravity*, vol. 30(9), 095 007, 2013.

[35] Y. Gao, F. Guo, R. Das, P. Mascher, and A. P. Knights, High responsivity si/ge phototransistor on silicon photonics platform for small signal application, in *2023 Photonics North (PN)*, IEEE, 2023, 1–1.

[36] D. H. Hagan, Y. Xie, R. Das, A. S. Kashi, J. C. Cartledge, and A. P. Knights, Modification of the electrical properties of a silicon waveguide avalanche photodetector operating at 1550 nm via defect engineering, *Journal of Lightwave Technology*, vol. 42(2), 704–712, 2024.

Chapter 6

Erbium implanted waveguide amplifier on SiN platform

This chapter includes the results for a SiN waveguide amplified with Er-implanted tellurium oxide thin film cladding. The integrated spiral waveguide is fabricated using a standard silicon photonics foundry process. The Tellurium Oxide thin films were applied using a sputtering system, followed by the introduction of Er ions through an ion implantation system. Optically active Er ions are evidenced by a 9 dB small-signal enhancement and visible green emission, resulting from the up-conversion process of Er ions. Additionally, a moderate thermal treatment has proven effective in mitigating waveguide propagation losses, improving Er lifetime, and boosting overall gain efficiency. This study is currently being prepared for publication by the authors and is included in this thesis due to its innovative approach to integrating active Er ions into a Tellurium Oxide matrix. It highlights the device's potential for gain applications, subject to design optimization and post-fabrication treatments.

6.1 Abstract

In this paper, we demonstrate optical amplification in an ion-implanted erbium-doped hybrid tellurium oxide waveguide on a wafer-scale silicon nitride platform. Silicon nitride waveguides of 2 µm width and 100 nm height are cladded with 110 nm tellurium oxide, followed by erbium ion implantation with an energy of 200 KeV and a dose of $1 \times 10^{15} cm^{-2}$. A small signal enhancement of 9 dB was achieved on a 11 cm long waveguide, with an erbium lifetime of over 800 µs after low-temperature annealing at 150 °C for 30 minutes.

6.2 Introduction

Erbium-Doped Fiber Amplifiers (EDFAs) have been a tremendous success since their invention in the 1980s [1]. Primarily operating in the C-band and L-band of the optical spectrum, EDFAs are pivotal in supporting Dense Wavelength Division Multiplexing (DWDM) to significantly increase the data capacity of optical fibers, crucial for managing the burgeoning demand in global communication networks with high data integrity and enhanced network scalability, especially in applications like cloud computing and data centers [2]. To miniaturize the EDFA for applications in integrated photonic circuits, Erbium-Doped Waveguide Amplifiers (EDWAs) have been extensively studied for higher reliability and lower cost. However, it still remains a challenge to efficiently incorporate Er ions, especially when the waveguide has a much shorter amplification length compared to conventional EDFAs.

Different material systems and fabrication techniques have been investigated to achieve high Er solubility, low propagation loss, uniform growth over a large substrate area, compatibility with complementary metal-oxide semiconductor (CMOS), and sufficiently high deposition rate [3]. Various host materials including crystalline materials like lithium niobate [4–6] and amorphous materials like aluminum oxides (Al_2O_3) [7–11], tantalum

pentoxide (Ta_2O_5) [12, 13], and tellurium oxide (TeO_2) [14–16] are widely investigated to obtain optical gain by erbium doping. Among these, tellurium oxide (TeO_2) provides several benefits as a host medium for EDWAs compared to other substances, such as a high refractive index, which leads to a larger emission cross-section and enables more compact devices, a broad emission bandwidth, high solubility of erbium, and minimal cross-relaxation between ions [14]. Previously, co-sputtering of tellurium and rare-earths in an oxygen ambient have been used for successful fabrication of EDWAs [14–17].

Ion implantation of Er is also an ideal technique to fabricate EDWAs. As a non-equilibrium method, ion implantation allows for higher concentrations of erbium, offers a high degree of control over the position of the implanted ions within the target material [18]. Moreover, co-doping of different ions can be easily achieved with ion implantation compared with other techniques [19]. One common approach to improve the emission of Er^{3+} is to co-dope with ytterbium (Yb) ions, which facilitates efficient energy transfer to Er ions, reducing losses due to upconversion, and allowing for the optimization of dopant concentrations to minimize quenching effects [18]. Implantation of oxygen, in addition to erbium, is necessary for efficient electrical activation and a high percentage of optically active erbium ions, leading to the formation of Er–O complexes that act as efficient electronic traps, promoting radiative transitions and increasing erbium solubility [18]. Ion implantation of Er also shows less undesired cooperative upcoversion compared to co-sputtered films [20].

Silicon nitride (Si_3N_4) photonic integrated circuits (PICs) have been widely explored for applications in telecommunications [21, 22], lasing [17, 23, 24], and sensing [25, 26] due to its advantages of ultra low propagation loss, wide transparent wavelength window, low temperature sensitivity, high power handling, and compatibility with standard silicon photonics technology [27, 28]. Optical amplification on such a platform is crucial for signal boosting and loss compensation to enable complex functionalities in scaled

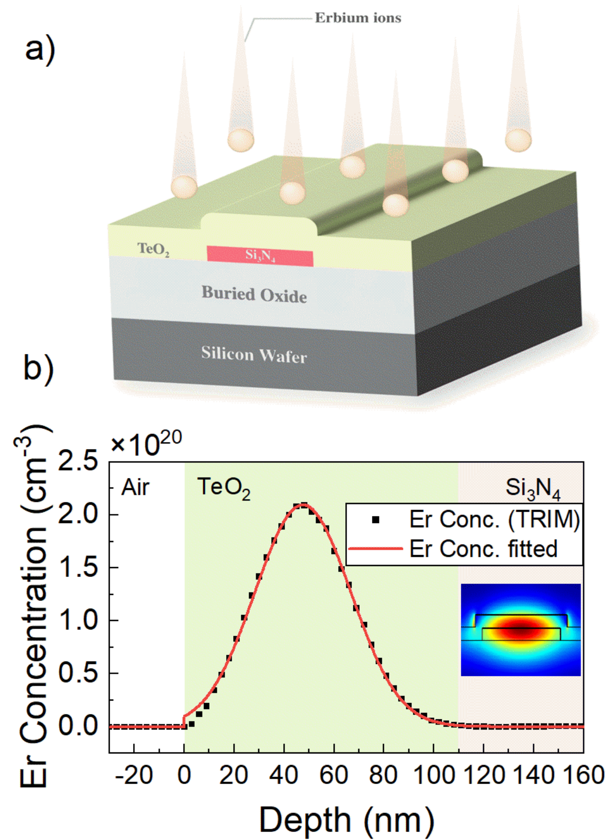

FIGURE 6.1: a) Diagram of the TeO_2:Er^{3+}-coated Si_3N_4 waveguide structure. b) Calculated (black dot) and fitted (red line) erbium concentration using TRIM simulations, and the simulated optical transverse electric (TE) mode intensity (inset).

photonic systems.

In this work, we demonstrate an EDFA using Si_3N_4 waveguides cladded with Er^{3+}-implanted TeO_2 on an integrated platform. Low temperature annealing is demonstrated to activate the Er ions and improve the waveguide background loss by recovering the implantation damage. Signal enhancement of around 9 dB is demonstrated with an erbium lifetime of over 800 µs.

6.3 Methods

Figure. 6.1 (a) demonstrates the cross-section of the EDWA structure studied in this work. The uncladded Si_3N_4 waveguide with a height of 100 nm and a width of 2 µm was fabricated at LioniX International using stepper lithography and reactive ion etching [24]. The wide waveguide supports single mode propagation which resides in the waveguide center, decreasing the waveguide propagation loss due to the sidewall roughness. A height of 100 nm enables delocalization of the fundamental TE mode into the cladding, maximizing the overlap factor between the electric field and the active Er ions. The total spiral waveguide length is 11 cm, with linearly tapered edge couplers of 250 µm in length on both sides. The TeO_2 thin film with a thickness of 110 nm was deposited on the Si_3N_4 chip using a radio frequency (RF) reactive sputtering system (Lesker PVD Pro 200) at room temperature at the Centre for Emerging Device Technologies (CEDT) at McMaster University [29], with the detailed process described in [29]. Er^{3+} ions were introduced to the TeO_2 film via ion implantation with an energy of 200 KeV and a dose of $1 \times 10^{15} cm^{-2}$, carried out by the Ion Beam Centre at the University of Surrey. The Er^{3+} concentration, as plotted in Fig. 6.1 (b), is calculated by fitting the Transport of Ions in Matter (TRIM) simulation of Er implanted in TeO_2, where a peak concentration of 2×10^{20} cm^{-3} is obtained at a depth of around 50 nm into the TeO_2 film. The thickness of the TeO_2 layer was carefully chosen to allow for higher overlap between the mode and the Er ion distribution due to the short ion travel range of around 50 nm as shown in Fig.6.1 (b) inset while maintaining a low propagation loss. This configuration leads to more efficient excitation of the Er^{3+} ions residing in the TeO_2 film. Even though higher overlaps can be achieved with thicker TeO_2, prohibitive implantation energies would be needed to optimize the mode overlap with ion distribution. Moreover, a negligible amount of Er^{3+} penetrate beyond the TeO_2 layer, leaving the low-loss Si_3N_4 waveguide intact. Post ion implantation, low-temperature annealing at 150 °C for 30 min in nitrogen was performed for defect recovery and erbium activation.

Gain measurements are conducted using a one-sided pumping arrangement as depicted in Fig. 6.2. On the input side, a tunable C-band (1530–1565 nm) signal laser is combined with a pump laser diode at 1470 nm, using a wavelength division multiplexer (WDM). This combined light is then edge-coupled onto the device using a tapered fiber with a 2.5 µm spot size. The polarization paddles are finely adjusted for transverse electric (TE) mode launching considering the target waveguide structure supports on TE mode. Light exiting the waveguide is then coupled into another similarly tapered fiber. After this, the signal light that is outcoupled passes through WDM and a 1500 nm edge-pass filter, eliminating any remaining pump light after the WDM, and the transmitted signal is then detected using a photodetector. The measurement of the lifetime involves a function generator and an electrical oscilloscope, where a 100 Hz periodic square wave with a duty cycle of 50% is used to modulate the pump laser, and the spontaneous emission decay is detected with the oscilloscope. Single bus point-coupled microring resonators with a radius of 500 µm and various coupling gaps were also fabricated with 100 nm in height and 2µm in width to extract the intrinsic waveguide propagation losses using the passive configuration.

6.4 Measurement results

The intrinsic propagation loss of the waveguide was first determined by measuring point-coupled microring resonators. Fig 6.3 illustrates the ring's resonance in the same configuration under different states: post-TeO_2 deposition (red), post-Er implantation (blue), and post-annealing at 150 °C (green). The ring resonators are under-coupled with a gap of 2.8 µm and measured at the same wavelength range of around 1620 nm to extract the intrinsic Q factors beyond the Er absorption band.

Q factors of 5.4×10^5, 1.0×10^5, and 3.0×10^5 were obtained by fitting the transmission spectrum, in accordance with coupled mode theory, corresponding to propagation

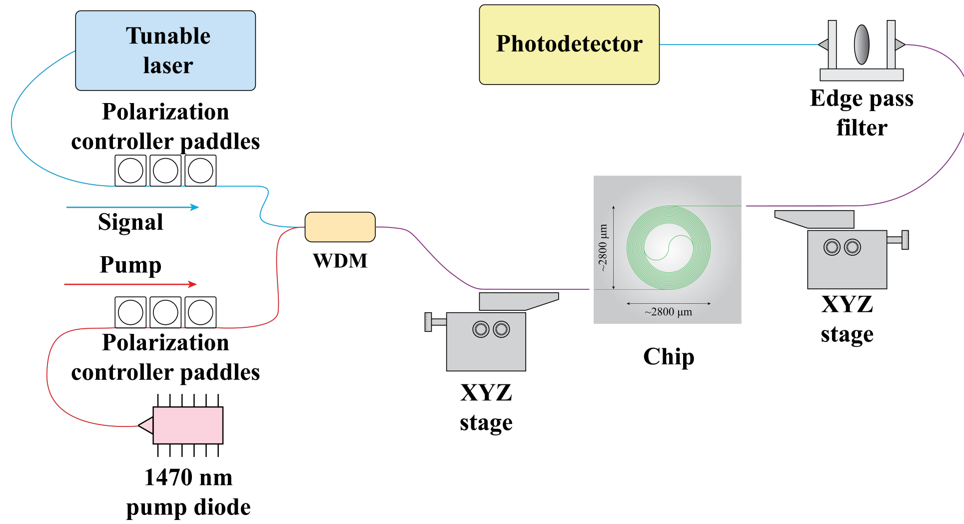

FIGURE 6.2: Experimental setup for measuring gain in TeO_2: Er^{3+} cladded Si_3N_4 spiral waveguides.

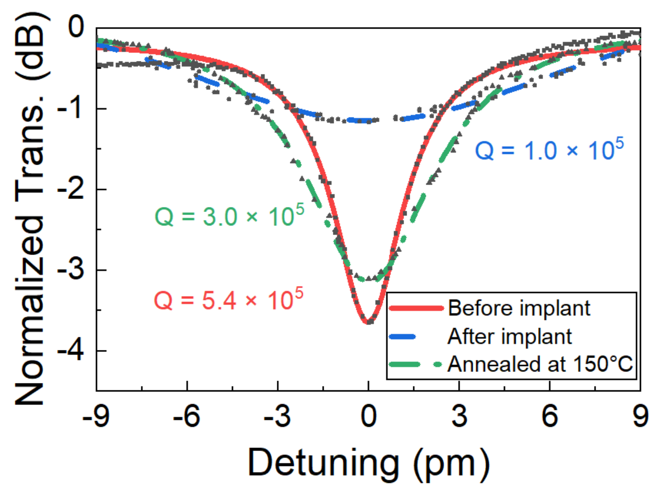

FIGURE 6.3: a) The Lorentzian fittings indicating the Q-factors of the microrings before implantation, right after implantation, and after annealing.

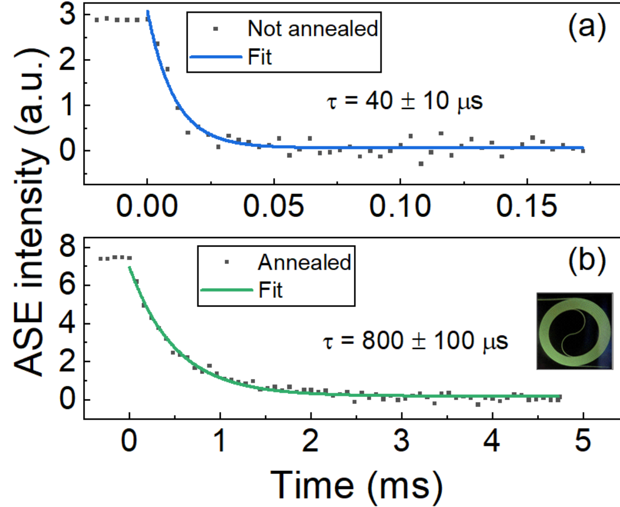

FIGURE 6.4: Measured and fitted photoluminescence intensity decay a) before and b) after annealing.

losses of approximately 0.5 dB/cm, 1.3 dB/cm, and 1.0 dB/cm, respectively. The implantation process significantly increases the waveguide propagation loss to 1.3 dB/cm, which is attributed to defects introduced in the TeO_2 cladding during implantation. Low-temperature annealing at 150 °C was employed to repair these defects and enhance waveguide transmission, successfully reducing the propagation loss to 1.0 dB/cm. Although higher temperatures than 150 °C might further decrease the loss introduced by implantation, they could cause the crystallization of the TeO_2 film [30], resulting in undesired increase in propagation loss. Furthermore, this low-temperature annealing process, significantly lower than previously employed temperatures of over 1000 °C [31], is compatible with standard CMOS processes.

In addition to the healed TeO_2 cladding, an increased photoluminescence lifetime of erbium was also observed in chips post-annealing. Fig. 6.4 demonstrates a 20 fold increase in lifetime to around 800 µs, as determined by exponential curve fitting, compared to approximately 40 µs before annealing. This increase is attributed to the repair of defects that acted as non-radiative recombination centers [18]. Additionally, annealing

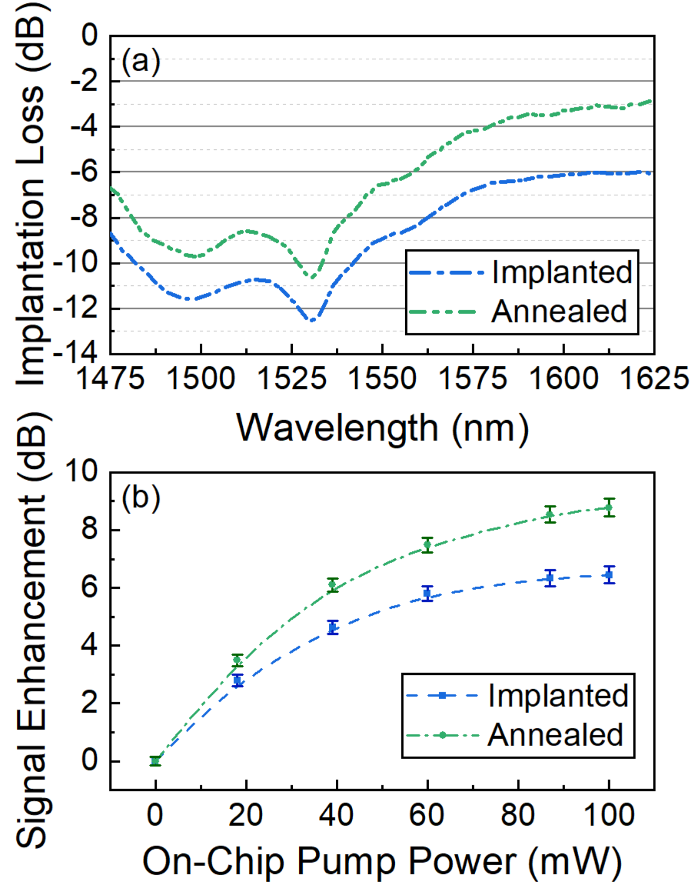

FIGURE 6.5: a) Measured Er implantation loss spectrum (excluding fiber-chip edge coupling loss) of waveguide after implantation (blue) and annealing (green); b) Measured signal enhancement factor (dB) at 1550 nm as a function of on-chip optical pump power (mW) at 1470 nm.

could possibly reduce the hydroxyl (OH) groups in the host material originated from the sputtering process, reducing quenching of the photoluminescence [32, 33]. Furthermore, annealing could facilitate the diffusion of Er ions within the TeO_2 cladding, resulting in a more uniform distribution of Er ions across the thin film, which mitigates concentration-related quenching [34]. A strong green emission from the second order Er^{3+} upconversion was observed after annealing (Fig. 6.4 inset), which agrees with the increased lifetime measured.

The passive transmission of the 11 cm spiral waveguide was measured at various

stages: post-cladding deposition, post-implantation, and post-annealing. In the cladded waveguide (without Er implantation), the total transmission loss was approximately 3.5 dB across the entire spectrum (1460 nm to 1640 nm), with a fiber-chip coupling loss of about 3 dB for both facets. The optical loss from Er implantation was calculated by subtracting the fiber-fiber waveguide loss from the transmission spectra of the implanted and annealed waveguide, as illustrated in Fig. 6.5(a), assuming consistent fiber-chip edge coupling loss across all measurements. After implantation, an increase in waveguide background loss of 0.6 dB/cm was observed at around 1620 nm, a wavelength where Er absorption is negligible. Consequently, the Er absorption loss was determined by subtracting the background propagation loss from the total loss due to implantation, with a peak absorption of about 0.65 dB/cm at 1530 nm. It was observed that the background loss, resulting from implantation damage outside the Er absorption band, could be significantly reduced to 0.3 dB/cm from 0.6 dB/cm with low-temperature annealing at 150 °C in nitrogen for 30 minutes, due to the recovery of implantation defects [35]. Meanwhile, the Er absorption was reduced by less than 0.2 dB/cm at 1530 nm, attributed to ion diffusion during the annealing process. It is notable that this reduction of 0.2 dB/cm is slightly less than the 0.3 dB/cm loss reduction at 1620 nm, indicating an increased absorption cross-section of Er post-annealing. This could result in a higher signal enhancement, as depicted in Fig. 6.5(b), showing the waveguide's signal enhancement at 1550 nm as a function of pump power sourced from a 1470 nm laser diode, with an on-chip signal power set around -20 dBm to prevent gain saturation. Peak signal enhancement factors of 0.6 dB/cm and 0.8 dB/cm were obtained from the 11 cm waveguide post-implantation and post-annealing, respectively. The net gain, calculated by deducting the waveguide erbium absorption loss and the background waveguide loss from the signal enhancement, was -8.7 dB before annealing and -7.2 dB after annealing. Double-sided pump was not able to improve the net gain due to the saturation of the low erbium concentration.

The lower gain efficiency can be primarily attributed to the limited overlap between the optical mode profile and the Er ions, a consequence of the considerable distance (approximately 80 nm) between the center of the Er ions distribution and the optical mode core. Enhancing gain efficiency could be realized by incrementally increasing the ion implantation depth into the Si_3N_4 waveguide, without damaging the waveguide structure. Applying a thicker TeO_2 film could enhance optical confinement within the TeO_2 area, due to the elevation of the mode towards the surface. Furthermore, an increased implantation dose is posited to augment signal enhancement. To circumvent quenching, a strategy of successive ion implants with incrementally higher energies could yield a more homogeneous ion distribution across a broader depth. In addition, suppressing waveguide background propagation losses through optimized post-implantation annealing conditions would further improve gain efficiency. While pumping with a 980 nm laser theoretically yields a higher population inversion, other crucial factors come into play. Single-mode operation is desired for both the pump and signal, aiming to improve coupling efficiency, achieve high mode overlap, exert control over the device's behavior, and reduce nonlinear effects. Conversely, reducing sidewall interactions is essential to minimize losses. Therefore, the device's design must strike a balance among waveguide geometry, population dynamics, and losses. Lastly, the co-doping of Er and Yb is suggested as an optimal approach for significantly enhancing Er efficiency due to the efficient energy transfer from Yb to Er ions [16].

6.5 Conclusion

In conclusion, this study demonstrates optical signal enhancement in an erbium-doped hybrid tellurium oxide waveguide on a silicon nitride platform. The integration of a silicon nitride waveguide with erbium ions implanted in tellurium oxide exhibits a notable small signal enhancement, achieved through carefully calibrated ion implantation and low-temperature annealing processes. The results indicate the potential for further

optimizations in waveguide design and ion implantation techniques to enhance gain efficiency. This work lays a foundational step towards a more efficient, CMOS compatible, integrated optical amplifier on silicon photonics platform, offering promising implications for telecommunications, sensing, and beyond.

Bibliography

[1] R. J. Mears, L. Reekie, I. Jauncey, and D. N. Payne, Low-noise erbium-doped fibre amplifier operating at 1.54 μm, *Electronics Letters*, vol. 19(23), 1026–1028, 1987.

[2] P. J. Winzer, D. T. Neilson, and A. R. Chraplyvy, Fiber-optic transmission and networking: The previous 20 and the next 20 years, *Optics Express*, vol. 26(18), 24 190–24 239, 2018.

[3] D. Nikolova, S. Rumley, D. Calhoun, Q. Li, R. Hendry, P. Samadi, and K. Bergman, Scaling silicon photonic switch fabrics for data center interconnection networks, *Optics Express*, vol. 23(2), 1159–1175, 2015.

[4] R. Brinkmann, I. Baumann, M. Dinand, W. Sohler, and H. Suche, Erbium-doped single and double pass Ti:$LiNbO_3$ waveguide amplifiers, *IEEE journal of quantum electronics*, vol. 30(10), 2356–2360, 1994.

[5] H. Suche, I. Baumann, D. Hiller, and W. Sohler, Modelocked Er: Ti:$LiNbO_3$ waveguide laser, *Electronics Letters*, vol. 29(12), 1111–1112, 1993.

[6] J. Zhou, Y. Liang, Z. Liu, W. Chu, H. Zhang, D. Yin, Z. Fang, R. Wu, J. Zhang, W. Chen, *et al.*, On-chip integrated waveguide amplifiers on erbium-doped thin-film lithium niobate on insulator, *Laser & Photonics Reviews*, vol. 15(8), 2 100 030, 2021.

[7] S. A. Vazquez-Cordova, M. Dijkstra, E. H. Bernhardi, F. Ay, K. Worhoff, J. L. Herek, S. M. Garcia-Blanco, and M. Pollnau, Erbium-doped spiral amplifiers with 20 dB of net gain on silicon, *Optics Express*, vol. 22(21), 25 993–26 004, 2014.

[8] J. Ronn, W. Zhang, A. Autere, X. Leroux, L. Pakarinen, C. Alonso-Ramos, A. Saynatjoki, H. Lipsanen, L. Vivien, E. Cassan, *et al.*, Ultra-high on-chip optical gain in erbium-based hybrid slot waveguides, *Nature communications*, vol. 10(1), 432, 2019.

[9] J. Mu, M. Dijkstra, J. Korterik, H. Offerhaus, and S. M. Garcia-Blanco, High-gain waveguide amplifiers in Si_3N_4 technology via double-layer monolithic integration, *Photonics Research*, vol. 8(10), 1634–1641, 2020.

[10] K. Worhoff, J. D. B. Bradley, F. Ay, D. Geskus, T. P. Blauwendraat, and M. Pollnau, Reliable Low-Cost Fabrication of Low-Loss Al_2O_3:Er^{3+} Waveguides With 5.4-dB Optical Gain, *IEEE Journal of Quantum Electronics*, vol. 45(5), 454–461, 2009.

[11] J. Bradley, L. Agazzi, D. Geskus, F. Ay, K. Worhoff, and M. Pollnau, Gain bandwidth of 80 nm and 2 dB/cm peak gain in Al_2O_3: Er^{3+} optical amplifiers on silicon, *JOSA B*, vol. 27(2), 187–196, 2010.

[12] A. Z. Subramanian, G. S. Murugan, M. N. Zervas, and J. S. Wilkinson, High index contrast Er: Ta_2O_5 waveguide amplifier on oxidised silicon, *Optics Communications*, vol. 285(2), 124–127, 2012.

[13] Z. Zhang, R. Liu, W. Wang, K. Yan, Z. Yang, M. Song, D. Wu, P. Xu, X. Wang, and R. Wang, On-chip Er-doped Ta_2O_5 waveguide amplifiers with a high internal net gain, *Optics Letters*, vol. 48(21), 5799–5802, 2023.

[14] K. Vu and S. Madden, Tellurium dioxide erbium doped planar rib waveguide amplifiers with net gain and 2.8 db/cm internal gain, *Optics Express*, vol. 18(18), 19 192–19 200, 2010.

[15] K. Vu, S. Farahani, and S. Madden, 980nm pumped erbium doped tellurium oxide planar rib waveguide laser and amplifier with gain in S, C and L band, *Optics Express*, vol. 23(2), 747–755, 2015.

[16] H. C. Frankis, H. M. Mbonde, D. B. Bonneville, C. Zhang, R. Mateman, A. Leinse, and J. D. B. Bradley, Erbium-doped TeO_2-coated Si_3N_4 waveguide amplifiers with 5 dB net gain, *Photonics Research*, vol. 8(2), 127–134, 2020.

[17] K. K. Miarabbas, H. C. Frankis, A. P. Knights, and J. D. B. Bradley, Silicon-thulium hybrid microdisk lasers with low threshold and wide emission wavelength range, *Optics Express*, vol. 31(12), 20 244–20 255, 2023.

[18] A. Kenyon, Erbium in silicon, *Semiconductor Science and Technology*, vol. 20(12), R65, 2005.

[19] G. Dearnaley, Ion implantation, *Nature*, vol. 256(5520), 701–705, 1975.

[20] P. Kik and A. Polman, Cooperative upconversion as the gain-limiting factor in Er doped miniature Al_2O_3 optical waveguide amplifiers, *Journal of Applied Physics*, vol. 93(9), 5008–5012, 2003.

[21] C. G. Roeloffzen, L. Zhuang, C. Taddei, A. Leinse, R. G. Heideman, P. W. van Dijk, R. M. Oldenbeuving, D. A. Marpaung, M. Burla, and K.-J. Boller, Silicon nitride microwave photonic circuits, *Optics Express*, vol. 21(19), 22 937–22 961, 2013.

[22] C. Xiang, W. Jin, and J. E. Bowers, Silicon nitride passive and active photonic integrated circuits: Trends and prospects, *Photonics Research*, vol. 10(6), A82–A96, 2022.

[23] C. Xiang, J. Guo, W. Jin, L. Wu, J. Peters, W. Xie, L. Chang, B. Shen, H. Wang, Q.-F. Yang, *et al.*, High-performance lasers for fully integrated silicon nitride photonics, *Nature communications*, vol. 12(1), 6650, 2021.

[24] B. L. Segat Frare, P. Torab Ahmadi, B. Hashemi, D. B. Bonneville, H. M. Mbonde, H. C. Frankis, A. P. Knights, P. Mascher, and J. D. B. Bradley, On chip hybrid erbium-doped tellurium oxide silicon nitride distributed bragg reflector lasers, *Applied Physics B*, vol. 129(10), 158, 2023.

[25] D. B. Bonneville, M. Albert, R. Arbi, M. Munir, B. L. S. Frare, K. K. M. Kiani, H. C. Frankis, A. P. Knights, A. Turak, K. N. Sask, *et al.*, Hybrid silicon-tellurium-dioxide dbr resonators coated in pmma for biological sensing, *Biomedical Optics Express*, vol. 14(4), 1545–1561, 2023.

[26] X. Tu, J. Song, T.-Y. Liow, M. K. Park, J. Q. Yiying, J. S. Kee, M. Yu, and G.-Q. Lo, Thermal independent silicon-nitride slot waveguide biosensor with high sensitivity, *Optics Express*, vol. 20(3), 2640–2648, 2012.

[27] D. J. Blumenthal, R. Heideman, D. Geuzebroek, A. Leinse, and C. Roeloffzen, Silicon nitride in silicon photonics, *Proceedings of the IEEE*, vol. 106(12), 2209–2231, 2018.

[28] T. Sharma, J. Wang, B. K. Kaushik, Z. Cheng, R. Kumar, Z. Wei, and X. Li, Review of recent progress on silicon nitride-based photonic integrated circuits, *IEEE Access*, vol. 8, 195 436–195 446, 2020.

[29] H. C. Frankis, K. K. M. Kiani, D. B. Bonneville, C. Zhang, S. Norris, R. Mateman, A. Leinse, N. D. Bassim, A. P. Knights, and J. D. B. Bradley, Low-loss TeO_2-coated Si_3N_4 waveguides for application in photonic integrated circuits, *Optics Express*, vol. 27(9), 12 529–12 540, 2019.

[30] T. Komatsu, H. Tawarayama, H. Mohri, and K. Matusita, Properties and crystallization behaviors of TeO_2 $LiNbO_3$ glasses, *Journal of non-crystalline solids*, vol. 135(2-3), 105–113, 1991.

[31] Y. Liu, Z. Qiu, X. Ji, A. Lukashchuk, J. He, J. Riemensberger, M. Hafermann, R. N. Wang, J. Liu, C. Ronning, *et al.*, A photonic integrated circuit–based erbium-doped amplifier, *Science*, vol. 376(6599), 1309–1313, 2022.

[32] Y. Y. Hui, P.-H. Shih, K.-J. Sun, and C.-F. Lin, Enhancement of 1.5 μm emission in erbium-doped spin-on glass by furnace annealing, *Thin Solid Films*, vol. 515(17), 6754–6757, 2007.

[33] L. Slooff, M. De Dood, A. Van Blaaderen, and A. Polman, Effects of heat treatment and concentration on the luminescence properties of erbium-doped silica sol–gel films, *Journal of non-crystalline solids*, vol. 296(3), 158–164, 2001.

[34] A. Polman, Erbium implanted thin film photonic materials, *Journal of Applied Physics*, vol. 82(1), 1–39, 1997, ISSN: 00218979.

[35] S. Coffa, F. Priolo, and A. Battaglia, Defect production and annealing in ion-implanted amorphous silicon, *Physical review letters*, vol. 70(24), 3756, 1993.

Chapter 7

Conclusions and future perspectives

7.1 Summary of work

The aim of this thesis was to explore and develop CMOS compatible photodetectors and optical amplifiers with enhanced gain on a silicon photonics platform to mitigate the limited link budget of silicon integrated photonics circuits. The operating principles, design and fabrication methods, characterization, and application of these devices have been thoroughly reported herein.

The motivation and the underlying theoretical background of the main concepts were given in the first two chapters. In chapter one, the motivation for this work was highlighted by discussing the need for next generation transceivers for data centers due to the increasing internet traffic. Featured with CMOS compatibility, silicon photonics stands out as one of the most promising platform for the development of robust, reliable, and high-speed transceivers. However, the challenge of photodetection and optical amplification on this platform is exacerbated by silicon's indirect bandgap. In Chapter 2, a

brief theoretical introduction was given emphasizing key concepts and design terms that were then used to describe the features of the devices focused in this thesis.

Chapter 3 presents an innovative design for a Si/Ge waveguide photodetector, which incorporates a bipolar phototransistor to achieve enhanced internal gain through transistor operation. This device demonstrated a high responsivity of 606 A/W, a low dark current of 4 μA, and a reduced phase noise of -80 dBc/Hz at a 1 V bias for an input power of -50 dBm. Under a 2.8 V bias, the device's responsivity increased to 1032 A/W with a dark current of 42 μA. The introduction of p^+-doping regions beneath the Ge epitaxial layer proved effective in amplifying photocurrent gain and diminishing dark current in comparison to a reference device lacking such regions. The positioning and width of the p^+-doped regions were optimized to further refine dark current and responsivity metrics. Experimental validation yielded a phase noise response of -80 dBc/Hz at a 1 kHz frequency offset and a small-signal -3dB bandwidth of 1.5 GHz, primarily limited by the base-collector junction capacitance. The combination of high responsivity, low dark current, and acceptable phase noise facilitates the detection of light across a broad power spectrum, rendering the device ideal for integration with advanced CMOS processes for applications requiring minimal dark current and phase noise characteristics.

In Chapter 4, a monolithic silicon avalanche photodetector leveraging surface state defects and bulk defects to achieve a near 5 A/W responsivity under a 32 V reverse bias is presented. Both types of defects exhibited different optimal operating regimes due to the difference in recombination center concentrations. Surface state defects contribute to the detector's stability and sustained high photocurrent after extended exposure to ambient conditions, attributed to the Si/SiO_2 interface defects from the thin equilibrium native oxide layer. It was also demonstrated that SSDs play a crucial role in enhancing the photocurrent of the photodetector despite the limited active area. Surface activation with HF was shown to enhance photocurrent by optimizing the interplay between SSDs

and bulk defects, resulting in a device with a 15.6 gain and an 8 GHz 3-dB bandwidth, promising for implementation in telecommunication applications.

The integration of monolithic silicon avalanche photodetector with SWG waveguide structures was put forward in Chapter 5 as a means of enhancing the responsivity of the photodetector by enhanced light-matter interaction due to slow light effect. A significant enhancement in responsivity, achieving 5 A/W, is attributed to the presence of slow light within the SWG waveguide. The design of an appropriate SWG structure was described, selected to maximize the group index, leading to enhanced gain. This structure was fully characterized optically and electrically, and produced a responsivity per unit length which was enhanced by more than three times compared to devices without SWG structures. Also, the use of defect-mediation was demonstrated, and results confirmed enhanced interaction between light and defects. This approach partially mitigates the limitations of silicon's indirect bandgap in photodetection. Experimental results reveal a substantial increase in optical response compared to traditional straight waveguide detectors in terms of responsivity per length. The incorporation of SWG waveguides into silicon photodetectors offers a promising avenue for enhancing their efficiency in mid-infrared applications.

Finally, optical amplification in an ion-implanted erbium-doped hybrid tellurium oxide waveguide on a wafer-scale silicon nitride platform was discussed in Chapter 6. The waveguide, measuring 2 μm in width and 100 nm in height, clad with 110 nm of tellurium oxide, was subjected to erbium ion implantation at 200 KeV with a dose of $1 \times 10^{15} cm^{-2}$. This configuration achieved a 9 dB signal enhancement over an 11 cm length, with an erbium lifetime exceeding 800 μs following a low-temperature annealing process at 150°C for 30 minutes. These findings underscore the potential for further optimization in waveguide design and ion implantation techniques to enhance gain efficiency, marking a fundamental step towards an efficient, CMOS-compatible, integrated

optical amplifier on the silicon photonics platform.

7.2 Suggested future work

Future work is recommended to broaden the experimental scope of this thesis, with each chapter's investigations outlined individually. Detailed recommendations will be provided for optimizing specific steps and procedures, alongside suggestions for related projects.

Si/Ge phototransistor

Despite the high responsivity achieved by the Si/Ge phototransistor discussed in Chapter 3, its bandwidth is limited to approximately 1.5 GHz. This limitation renders it less suitable for optical communication applications, which typically demands operational bandwidth in the tens of GHz range. The primary constraints on the device's bandwidth are attributed to the Miller Effect and significant junction capacitance, as outlined in [1]. To enhance the bandwidth, one viable approach involves reducing both the length and width of the device. Given the substantial optical absorption coefficient of Ge, a device length of just tens of microns could suffice to generate a significant photocurrent [2]. Furthermore, uni-traveling-carrier (UTC) photodiodes, which exhibit increased bandwidth by excluding slower-moving holes, present a model for increasing bandwidth [3]. A similar strategy might be applied to the Si/Ge phototransistor by introducing recombination centers (defects) via ion implantation techniques.

Another area for device enhancement relates to its terminal configuration. The current design employs a symmetric structure, with the emitter positioned centrally between two collectors. This arrangement results in only half of the device being biased during operation. The photocurrent could potentially be increased by applying bias across the entire device laterally, which would require meticulous device design and simulation.

An intrinsic benefit of the discussed phototransistor is its compatibility with standard silicon photonics technology, facilitating mass production without requiring additional post-fabrication processes. An interesting subsequent project could involve developing a LIDAR receiver that utilizes an array of these phototransistors [4, 5].

Defect-mediated avalanche photodetector

The combination of SSD and BDA showed an intriguing device responsivity with significant enhancement. The mechanism behind this phenomenon should be carefully investigated and a model needs to be established.

With the device bandwidth currently at approximately 8 GHz, there exists potential for improvement through reduction of device length. However, such modifications could adversely affect responsivity by limiting optical absorption from the defects. The gain-bandwidth product stands as a critical metric for assessing photodetector performance. Thus, efforts should be directed towards optimizing this parameter to enhance the device's gain-bandwidth.

The introduction of defects has been observed to augment both the photocurrent and the dark current. To improve the signal-to-noise ratio, employing a differential photodetection configuration could effectively mitigate the increase in dark current associated with the avalanche regime [6].

Furthermore, alternative approaches to surface treatment on SSDs merit exploration. For example, enhancing surface roughness could potentially increase absorption due to a larger surface area, presenting another dimension for device optimization.

Waveguide structure for Si photodetectors

The SWG waveguide photodetector, as discussed in Chapter 5, exhibited an increase in photocurrent at a wavelength of 1575 nm, deviating from the targeted 1550 nm. This

discrepancy may be due to inaccuracies in simulations and variations in the fabrication process. The initial step towards optimization should focus on refining the SWG design to enhance the device's responsivity specifically at 1550 nm. Moreover, it is essential to recognize that achieving the highest group index does not translate to the highest photocurrent, given the inherent trade-off between light-matter interaction and propagation loss. Consequently, the group index for the SWG structure must be experimentally determined, for instance, through an unbalanced Mach–Zehnder interferometer (MZI) to gain better understanding of the device design trade-off.

Additionally, the device's optical response rolls off rapidly outside its detection wavelength range. This limitation could be mitigated by incorporating apodized SWG waveguides and mode converters. Another strategy to optically boost the photodetector's responsivity involves utilizing cavities, such as microring resonators [7]. Comparing the SWG and cavity methods could yield interesting insights. It is also beneficial to assess how the SWG structure impacts the device's electrical bandwidth.

The high responsivity of 5 A/W achieved by the SWG photodetector was facilitated through ion implantation. Investigating an SWG photodetector integrated with Surface State Defects presents an intriguing prospect. The SWG configuration not only enhances light-matter interaction but also naturally expands the surface area, potentially further enhancing the responsivity. However, the current limitations of photolithography resolution in multi-project wafer (MPW) services hinder direct fabrication of SWGs under an oxide window. To expose Si SWG to air, one can either selectively etch the oxide cladding on top of the SWG waveguide, or expose an conventional waveguide to air and pattern it into an SWG waveguide using focused ion beam (FIB).

Erbium implanted waveguide amplifier

Enhancing the performance of an erbium-doped waveguide amplifier (EDWA) involves minimizing propagation losses while maximizing the excitation of Er^{3+} ions. An innovative approach to achieving lower propagation losses involves exploring alternative methods for depositing the crucial TeO_2 film. An electron cyclotron resonance plasma enhanced chemical vapour deposition (ECR-PECVD) system offers the benefit of depositing uniform and high-quality thin films, which could significantly improve the cladding of EDWA waveguides. Furthermore, integrating in-situ rare earth sputtering within this process could allow for uniform doping [8].

To optimize Er^{3+} ion emission, a comprehensive investigation into a matrix of parameters is needed. This includes examining the ion dose and depth, the geometry of the waveguide, and the thickness of the cladding film. Additionally, conducting an annealing study in incremental steps in temperature could reveal whether the losses induced by ion implantation can be fully recovered.

Since gain material is essential for the development of a laser, laser development combining the EDWA described in Chapter 6 and cavity structures should be explored.

Given the critical role of gain material in laser development, future research should also consider the integration of the EDWA described in Chapter 6 with various cavity structures for the development of advanced lasers on silicon photonics platform.

7.3 References

[1] D. Neamen, *Semiconductor physics and devices.* McGraw-Hill, Inc., 2002.

[2] M. Huang, S. Li, P. Cai, G. Hou, T.-I. Su, W. Chen, C.-y. Hong, and D. Pan, Germanium on silicon avalanche photodiode, *IEEE Journal of Selected Topics in Quantum Electronics*, vol. 24(2), 1–11, 2017.

[3] T. Ishibashi and H. Ito, Uni-traveling-carrier photodiodes, *Journal of Applied Physics*, vol. 127(3), 031 101, 2020.

[4] C. V. Poulton, M. J. Byrd, P. Russo, E. Timurdogan, M. Khandaker, D. Vermeulen, and M. R. Watts, Long-range lidar and free-space data communication with high-performance optical phased arrays, *IEEE Journal of Selected Topics in Quantum Electronics*, vol. 25(5), 1–8, 2019.

[5] Y. Yoshida, T. Umezawa, A. Kanno, and N. Yamamoto, A phase-retrieving coherent receiver based on two-dimensional photodetector array, *Journal of Lightwave Technology*, vol. 38(1), 90–100, 2020.

[6] P. J. Windpassinger, M. Kubasik, M. Koschorreck, A. Boisen, N. Kjærgaard, E. S. Polzik, and J. H. Müller, Ultra low-noise differential ac-coupled photodetector for sensitive pulse detection applications, *Measurement Science and Technology*, vol. 20(5), 055 301, 2009.

[7] J. J. Ackert, Silicon-on-insulator microring resonator defect-based photodetector with 3.5-GHz bandwidth, *Journal of Nanophotonics*, vol. 5(1), 059 507, 2011, ISSN: 1934-2608.

[8] Y. Gao, Z. Khatami, and P. Mascher, Influence of Nitrogen on the Luminescence Properties of Ce-Doped SiO_xN_y, *ECS Journal of Solid State Science and Technology*, vol. 10(7), 076 005, ISSN: 2162-8769.